NUMERICAL SIMULATION OF PRESSURE WAVE SUPERCHARGER WITH POCKETS OPERATING AT DIFFERENT SPEEDS

by

Pawan Sutar

A Thesis

Submitted to the Faculty of Purdue University

In Partial Fulfillment of the Requirements for the degree of

Master of Science in Mechanical Engineering

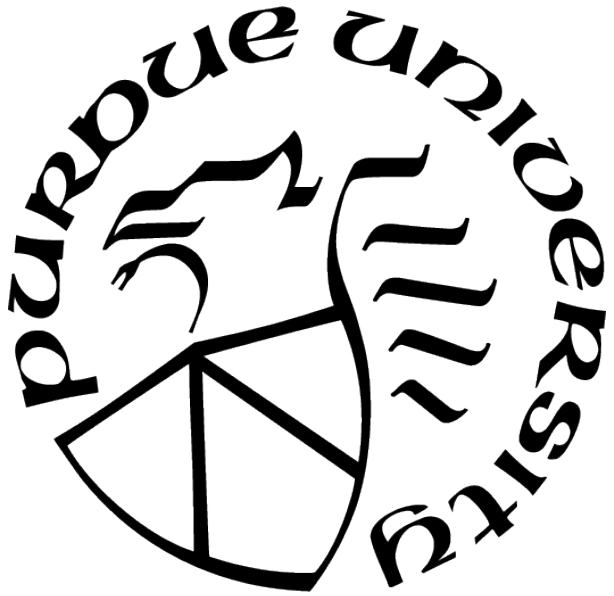

Department of Mechanical and Energy Engineering

Indianapolis, Indiana

December 2020

THE PURDUE UNIVERSITY GRADUATE SCHOOL
STATEMENT OF COMMITTEE APPROVAL

Dr. M. R. Nalim,, Chair

Department of Mechanical and Energy Engineering

Dr. Carlos Larriba-Andaluz

Department of Mechanical and Energy Engineering

Dr. Eric Adams

Department of Mechanical and Energy Engineering

Approved by:

Dr. Jie Chen

To my family and all concerned persons who made this journey possible

ACKNOWLEDGMENTS

I would like to express my sincere gratitude to my thesis advisor Dr. M. Razi Nalim for giving me the opportunity to work on the wave rotor analysis programs. His immense knowledge and guidance helped me in all the time of research and writing of this thesis.

I would also like to extend my thanks to my thesis committee, Dr. Carlos Larriba-Andaluz and Dr. Eric Adams, for their encouragement and insightful comments.

Last but not least, I am genuinely appreciative of the Department of Mechanical and Energy Engineering and IUPUI for making all the valuable resources available.

TABLE OF CONTENTS

LIST OF TABLES

LIST OF FIGURES

LIST OF SYMBOLS

Symbols and Units	Description
A [in^2]	Cross-sectional area
a [in/s]	Sonic speed (local)
b [in]	Passage width
c_p [$(ft.lb_f)/(lb_m.^\circ R)$]	Specific heat at constant pressure
c_v [$(ft.lb_f)/(lb_m.^\circ R)$]	Specific heat at constant volume
e [$(ft.lb_f)/lb_m$]	Total energy per unit mass
γ	Specific heat ratio
H [$(ft.lb_f)/lb_m$]	Enthalpy (total)
h [$(ft.lb_f)/lb_m$]	Enthalpy (local)
h [in]	Passage height
L [in]	Passage length
M	Mach number
m [lb_m]	Mass
$\dot{m}$ [lb_m/min]or[$non-dimensional$]	Mass flow rate
P [lb_f/in^2]	Stagnation (total) pressure
p [lb_f/in^2]	Static pressure
$\boldsymbol{\pi}$ [$Non-dimensional$]	Pressure ratio
R [$(ft.lb_f)/(lb_m.^\circ R)$]	Gas constant
ρ [lb_m/ft^3]	Density
T [$lb_f.ft$]	Torque
T [$^\circ R$]	Stagnation temperature
t [$^\circ R$]	Static temperature
t [s]	Time
τ [$Non-dimensional$]	Temperature ratio
u [ft/s]	Velocity
V [ft^3]	Volume
W [hp]	Power

ABBREVIATIONS

NASA Q1D	NASA Quasi-One-Dimensional: wave rotor analysis code
SCW1D-A	Simulation of Combustion and Waves: wave rotor analysis code used for axial passage wave rotor analysis (version A)
SCW1D-B	Simulation of Combustion and Waves: wave rotor analysis code used for non-axial passage wave rotor analysis (version B)
PWS	Pressure Wave Supercharger
BBC	Brown Boveri and Company
GRC	NASA Glenn Research Center
IUPUI	Indiana University Purdue University, Indianapolis
AI	Air Inlet Port
AO	Air Outlet Port
EI	Exhaust Inlet Port
EO	Exhaust Outlet Port
CP	Compression Pocket
EP	Expansion Pocket
GP	Gas Pocket

ABSTRACT

Pressure wave supercharger is an application of wave rotor technology that utilizes compression waves produced by high-pressure engine exhaust gas to compress the fresh intake air within the channels. The phenomena within the wave rotor channels are governed by compression and expansion waves initiated when the channel ends are periodically exposed to differing pressure ports. Two incoming fluids are brought into contact for a very short amount of time to facilitate efficient energy and momentum transfer, thereby exchanging pressure dynamically between the fluids by means of unsteady pressure waves. Since the energy transfer is based on unsteady pressure waves, correct matching of waves and ports is essential for optimum results. Mistiming of the waves in the channels is detrimental to the efficient exchange of pressure and low-pressure exhaust scavenging, which ensures minimum exhaust gas recirculation. Due to varying speed and load conditions of the unit to be supercharged, it is not always possible to maintain the rotor speed constant at the design point.

To mitigate the effects of wave mistiming due to varying speed, a well-designed combination of wall-pockets was used in Comprex® pressure wave supercharger. The wall-pockets are the recesses provided in the endplates of pressure wave superchargers to create necessary pressure zones at desired locations. This thesis details an extensive qualitative and computational investigation of the performance of pressure wave superchargers with pockets. Numerical simulations of pressure wave superchargers have been performed using the wave rotor analysis codes employed at the Combustion and Propulsion Research Laboratory at IUPUI. This work also pays close attention to inspecting the numerical schemes and modeling of different physical phenomena used in each code. A comparative verification of the wave rotor analysis codes has been conducted to ensure that the same fundamental numerical scheme is correctly implemented in each code. The issue of low-pressure scavenging has been demonstrated by simulating the four-port (pocketless) pressure wave supercharger operating at lower speeds. The wall-pockets have been modeled using a simple lumped volume technique. The gas state in the lumped volume of pockets is estimated using the continuity and energy equations such that the net mass and energy fluxes between each pocket and

the wave rotor channels are close to zero. The lumped volume models of pockets have been implemented in the four-port wave rotor configurations to simulate the pressure wave superchargers with pockets. The simulation results show that the pockets assist to maintain sufficient pressure in the desired zones to facilitate proper low-pressure scavenging during lower rotor speed operations. The Comprex simulation results have been observed to be in good agreement with experimental data and qualitative analysis. Specific observations on the performance of each code and comprehensive simulation results have been presented.

1. INTRODUCTION

1.1 Literature Review

The concept of harnessing the unsteady and periodic flows for practical purposes has been recognized since the early twentieth century. Despite the evolution of concept into the successful development of operating cycles and unsteady-flow devices, it had not been able to catch enough attention from the engineers. Further, sporadic efforts have been noted in making substantial improvements to the earlier invented wave machines until recent years. Shock tubes, shock tunnels, pulse combustors, pulse detonation engines, and wave rotors are some of the well-known applications of the unsteady wave machines. The wave machines employ the unsteady pressure waves generated in appropriate confined volumes to directly exchange the energy and pressure between different fluids without involvement of mechanical parts. The main advantage of these wave machines is their capacity to achieve higher pressure exchange in shorter time or length. Also, wave compression is a relatively efficient process at moderate pressure ratios compared to mechanical compression. Despite the most appealing features, the unsteady-flow machines have been relatively overlooked by the engineers considering the limited computational resources available to perform detailed flow calculations and analysis of unsteady wave phenomena. The wave machines have the potential to significantly improve the performance of engines if the unsteady flow taking place in the wave machines is deciphered and appropriately analyzed [1].

Wave rotor machines are the earliest types of unsteady-flow devices, with the first application dating back to 1906. A wave rotor is essentially comprised of an array of passages arranged around the axis of a cylindrical rotor. The rotor rotates between two stationary endplates that carry a few ports or manifolds. As the rotor rotates, the passages are exposed to differing pressure ports. By carefully selecting the numbers and positions of ports, a wave rotor can be used for a variety of applications. The four-port configuration of wave rotor, known as pressure wave exchanger/supercharger, has been focused on in this study. First attempts to commercialize the wave rotor pressure wave supercharger technology initialized in the early 1940s, when Brown Boveri Company (BBC) in Switzerland designed a wave rotor as topping stage for a 1640 kW gas turbine [2], [3]. The BBC's work was based on

several patents of Claude Seippel, filed from 1940 to 1949 [4], [5], [6], [7]. Although this first application could not deliver the results as expected, its satisfactory integration and continuous working led to the idea of using wave rotors for diesel engine supercharging. The first units were manufactured and tested between 1947 and 1955 after joint efforts of ITE Circuit Breaker Company, U.S. Bureau of Aeronautics, and Cornell University [8], [9]. In 1955, a cooperative program was started with BBC to pursue the development of pressure wave supercharger for diesel engines [10]. BBC's pressure wave supercharger, commonly known by its tradename Comprex, was first installed on a truck engine in 1971 [10]. After testing successfully on Opel 2.1 l diesel engine in 1978, the Comprex appeared in passenger cars as the primary supercharging device [11], [12], [13]. Around 1980, the Comprex research was handed over to MAZDA in Japan, when the BBC researchers returned to work on the wave rotor topping stage for gas turbine engines. The most successful commercial application of Comprex was found in MAZDA 626 Capellas with 2.0 l RF-series engines. From 1987 to the late 1990s, over 150,000 MAZDA diesel cars were produced, with Comprex being the primary supercharging device. Additionally, the Comprex has been tested effectively on vehicles such as Mercedes-Benz, Peugeot and Ferrari, and on other heavy-duty engines.

Successful commercialization of Comprex attracted the interest of many research groups around the world. After 1985 wave rotor workshop, there has been significant progress in the development of wave rotor technology supported by precise experimental techniques and high-performance computational resources to simulate the unsteady flow field inside the wave rotor passages. The wave rotor program at NASA Glenn Research Center, started in 1988, has aimed to investigate the benefits of using wave rotor technology for improving the performance of future aeroderivative engines [14]. In 1993, Wilson and Paxson at NASA GRC, published a feasibility study of wave rotor topping cycle for gas turbine engines [15]. Welch et al. in 1995, investigated the advantages of using wave rotor topping cycle for baseline turboshaft engines by predicting a 19-21% increase in specific power and a 16-17% decrease in specific fuel consumption. Welch later studied the effects of wave rotor channel curvature to demonstrate the wave turbine [16], [17].

Paxson in the early 1990s developed a gas-dynamic model and computational code implemented in FORTRAN to predict the performance characteristics of wave rotors by simulating

the unsteady flow field inside the channels of wave rotors. The code uses an explicit, second order, Lax-Wendroff type TVD scheme based on Roe's approximate Riemann solver to numerically solve the one-dimensional Euler equations, which are used to describe the unsteady, compressible and viscous flow occurring in the wave rotor channels. Paxson's wave rotor analysis tool, popularly known as NASA quasi-one-dimensional (Q1D) code, uses simplified models to account for channel area variation (hence, 'quasi' 1D), and for various physical phenomena and loss mechanisms associated with the wave rotor operation, such as gradual passage opening and closing, leakage to the central cavity, viscous (frictional) and heat transfer effects and other non-uniformities arising due to incorrect shock incidences and improperly mixed port flows. Nalim at NASA GRC investigated and developed a combustion model for wave rotors for use as constant volume pressure gain combuster [18]. Nalim and Paxson later extended the capability of NASA Q1D code to predict the combustion in wave rotors by both detonation and deflagration modes [19], [20].

Nalim, after joining Indiana University Purdue University Indianapolis (IUPUI) in 1997, continued the research on combustion wave rotor. From 1997 to 2020, IUPUI wave rotor research program has recorded continuous and significant progress in the development of wave rotor combustor test rig. Nalim and other researchers at IUPUI wave rotor program have been working on a wide variety of wave rotor applications, ranging from four-port wave rotor to pulse detonation engines. A computational and experimental program is currently being conducted at IUPUI in collaboration with Rolls-Royce to investigate the performance of combustion wave rotors. Some of the important publications and insights about the programs can be found in ref. [1]. The computational research conducted at IUPUI by Nalim and coworkers has resulted into a flexible and robust wave rotor analysis code, termed as Simulation of Combustion and Waves One-Dimensional (SCW1D), which retains the methodology of the NASA Q1D unsteady combustion code, generalized for any number of ports, and with substantial reorganization for modularity and modern coding practices. Various researchers have worked on the SCW1D program to extend its capability to incorporate additional processes such as two-step, four-species combustion, radial (passage-to-passage) leakage [21] and passage curvature [22]. Researchers at Nalim's lab at IUPUI have also investigated the possibility of using a pressure wave supercharger for Kubota diesel engine used in IUPUI

racing vehicle for Snowmobile competition. A four-port wave rotor scaling study has been performed to design a pressure wave supercharger for the specifications of diesel engine used. The main drawback of a four-port wave rotor as a pressure wave supercharger is its variable speed compatibility. Four-port wave rotors are effective only at design speed. If the rotor speed is decreased, the performance of pressure wave supercharger gets drastically affected, leading to a possible collapse. Further, the reduced rotor speed results in the issue of low-pressure scavenging and excessive exhaust gas recirculation. One of the possible solution to extend the operability of a four-port wave rotor supercharger is to provide the wall-pockets or recess in the endplates to ensure proper low-pressure scavenging as described in a 1964 patent by J. Waleffe [23]. Despite a successful commercial application, the pocket combinations have not gained enough attention in terms of computational modeling and simulation. Similar study has been conducted earlier by S. Basu at Nalim's lab to incorporate the wall-pockets in available NASA Q1D version [24],[25]. This work aims to extend the capacity of SCW1D code to incorporate the wall-pockets used in four-port wave rotors for the speed and load range extension, based on waleffe's patent. Observations and simulations presented in this thesis have satisfactorily predicted the performance of a pressure wave supercharger with pockets.

1.2 Background

Wave rotors have a variety of configurations for different applications. Four-port wave rotors, commonly known as pressure wave superchargers, are mainly used as superchargers for IC engines. PWS utilizes unsteady pressure waves produced by high-pressure engine exhaust to compress fresh intake air. Even if the purpose of PWS is similar to conventional turbochargers, their working principles are entirely different. Conventional turbochargers separate exhaust and intake charges into the separate turbine and compressor chambers, respectively. Energy from high-pressure engine exhaust gases is extracted to drive a turbine, coupled to a compressor where fresh intake air is compressed. Turbochargers are popularly and prevalently used in automotive applications for their manufacturing simplicities. Wave rotor PWS is an unsteady wave machine, which can be used as an alternative to conventional turbochargers, to perform efficient inter-fluid pressure exchange. Unlike conventional

turbomachines, PWS brings high-pressure and low-pressure fluids into contact for a very short amount of time, thereby allowing energy and momentum transfer dynamically, without significant involvement of mechanical parts. The most successful application of PWS for automotive supercharging was in Mazda RF series diesel engines, found in 1988 Mazda 626 Capella. Mazda produced over 150,000 diesel cars fitted with Comprex pressure wave supercharger from 1988 to 1995.

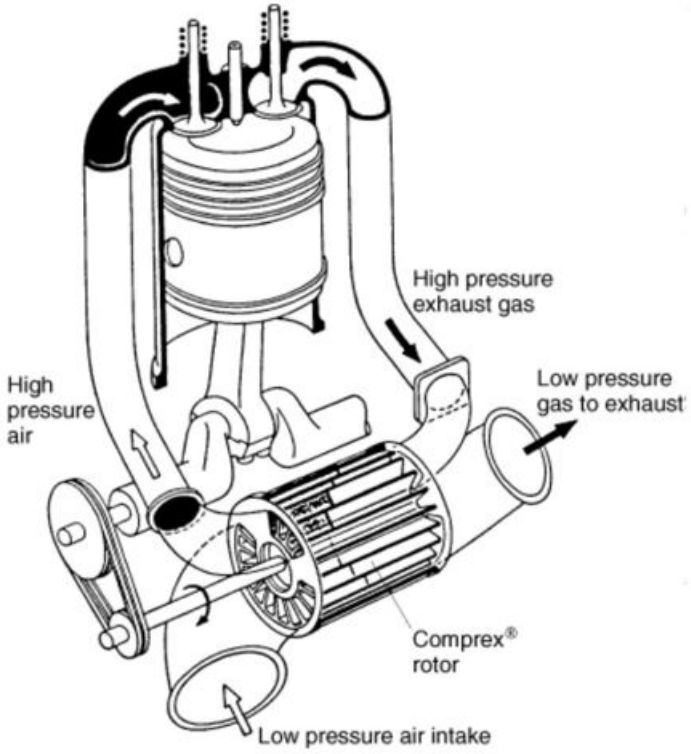

Figure 1.1. Wave rotor pressure wave supercharger operating principle [26]

A wave rotor PWS comprises a cylindrical rotor containing rows of circumferentially distributed channels, two stationary endplates having inlet and exhaust ports, and a cylindrical shroud to enclose the rotor and to connect the endplates together. Rectangular wave rotor channels are arranged around the axis of rotor, typically in a row or two. The rotor is mounted on a drive shaft, which is driven by the unit to be supercharged. The stationary endplates must be placed at the rotor ends with minimum clearance to avoid leakage while ensuring there is no rubbing contact between rotor and endplates under any operating and thermal condition. The outer shroud connects the endplates while preventing leakage of

fluids to the ambient. A four-port PWS can be of through-flow or reverse-flow type. As the rotor rotates, the channels are periodically exposed to the differing pressure inlet and exhaust ports in the endplates. When the channels are exposed to the exhaust outlet port, residual exhaust gases are expelled out of the rotor, and expansion waves are produced, allowing the suction of fresh air into the channels through the air inlet port. Eventually, when the channels are exposed to the high-pressure exhaust inlet port, compression waves propagate into the channel, compressing the fresh air inside the channels. The compressed fresh air is then allowed to exit the rotor and fed to the engine. During an ideal cycle, the interface between air and exhaust should not reach the air outlet port in order to avoid the penetration of exhaust gas into the engine cylinder. The pressure wave phenomena and correct wave timings will be discussed in detail in Chapter 4.

Since the PWS is generally driven by the engine to be supercharged, it is not always possible to maintain the rotor speed constant at the design point. As the pressure waves traveling in wave rotor channels do not change their speed, fluctuating speed of rotor results in inappropriate shock incidences. Reflection of pressure waves from imprecise locations causes a significant reduction in compression efficiency as well as undesirable backflows resulting in reduced mass flow rates through the ports. Further, the reduced speed of the rotor is detrimental to the low-pressure scavenging. These shortcomings can be overcome by providing pockets between the high-pressure and low-pressure parts of a reverse-flow PWS. Wall-pockets are the recesses provided in the walls of PWS for creating or maintaining high-pressure zones at desired locations. Commercial PWS Comprex was provided with three wall-pockets along with the inflow and outflow ports. Each pocket serves to either create or

Figure 1.2. Components of Comprex Pressure Wave Supercharger. a. rotor; b. hot stator plate; c. cold stator plate; d. Comprex unit [27]

maintain sufficient pressure zones at desirable locations to assist proper low-pressure scavenging while operating at lower rotor speeds. Details on the working of pockets combination will be presented in Chapter 6.

1.3 Problem Statement

A well-designed wave rotor PWS operating at the design point is theoretically highly efficient device due to the less involvement of mechanical parts. The energy is exchanged dynamically between the fluids by bringing them into contact for a precise amount of time. However, the complex gas dynamics present a variety of problems under practical operating conditions. Hence regardless of the most appealing highlights, a few difficulties have obstructed the general commercialization of wave rotors. Various research efforts have been completed during the past century to comprehend the complex unsteady flow field and innovatively design and optimize the wave rotors. The challenges have been fundamentally of a mechanical sort, such as leakage and thermal expansion. However, the performance of four-port wave rotor under variable speed and load conditions still remains a major issue. Incorrect shock incidences as a result of off-design rotor speed tend to reduce the compression efficiency significantly. As the rotor speed is reduced, the compression wave coming formed by the exhaust gas will strike the solid wall before reaching the air outlet port. The air will be compressed before opening the air outlet port, and the compression wave will reflect back into the channel. This phenomenon creates a low-pressure zone at the opening of air outlet port, causing undesirable backflow from the port.

Consequently, the reflected shock creates a high-pressure field in the channel, obstructing the inflow from the exhaust inlet port. Inadequate exhaust inflow results in reduced pressure between the low-pressure part and the high-pressure part of the PWS. The low-pressure field established at the beginning of the low-pressure part adversely affects the exhaust outflow through the low-pressure outlet port. As a result, sufficient fresh air inflow will be restricted, and excessive exhaust gas will be recirculated.

To overcome the unfavorable outcomes of the reduced speed, a PWS can be provided with some means to establish sufficient pressure zones at the beginning of the low-pressure part. The Comprex PWS accommodates the constructions between the low-pressure and

the high-pressure parts to develop ample pressure zones at the desired locations. These constructions are referred to as wall-pockets. The qualitative analysis of PWS wall-pockets was first presented in a 1964 patent by J. Waleffe et al. [23]. The pocket combination was later implemented into the design of Mazda Comprex PWS to provide it with variable speed operability.

The previous experimental and computational research on Comprex focused on the characterization and its integration with the baseline engines. Hence most of the numerical work concentrates on Comprex analysis as a four-port port wave rotor. Despite being a convenient solution, the strategy of using wall-pockets has caught very less attention. The approaches to numerically simulate the pocket combination have been previously examined at Dr. Razi Nalim's lab by Siddharth Basu. To the author's information, the current work is only the second to investigate the numerical modeling of the wall-pockets and identify their effects on the off-design performance. The wave rotor analysis codes used in this study provide a superlative platform to design and scale different wave rotor configurations. In the current work, an attempt has been made to enable the wave rotor analysis codes to simulate the wall-pocket combinations used in the Comprex-like PWS. The pocket locations can be decided by conducting some qualitative analysis of the PWS cycle. The capacity of the codes to incorporate the wall-pockets is highly advantageous when scaling a Comprex-like wave rotor configurations for custom applications.

1.4 Methodology

In order to investigate the complex phenomena inside the rotating PWS channels, it is crucial to study the dynamics of pressure waves, which take place inside the wave rotor channels. Different versions of a well-known wave rotor numerical analysis codes have been used for numerical simulation of dynamic pressure waves in this work. Three versions of numerical analysis tools are currently employed at the Combustion and Propulsion Research Laboratory (CPRL) at Indiana University-Purdue University, Indianapolis (IUPUI). The original program developed at NASA and documented in Paxson [28], [15], [29], [30] and Nalim [31], is generally referred to as NASA quasi-one-dimensional (Q1D) wave rotor code. Additional modifications to the original Q1D code, performed by Dr. Razi Nalim and other

researchers from IUPUI wave rotor group over the past 20 years, have been consolidated into functional modules so as to improve the organization and flexibility of the program and yield additional features. The class of these modified codes is named as Simulation of Combustion and Waves- 1D (SCW1D). SCW1D has two versions, SCW1D-A for wave rotors with axial passages and SCW1D-B for bent (slanted or curved) passages (wave turbine). The computational tools will be elaborated in Chapter 2. Performance assessment of the different versions of code has been carried out in Chapter 3.

The preliminary performance assessment study has been performed on the wave rotor analysis codes to verify their accuracy and sensitivity. The codes were used to simulate the basic unsteady flow processes, and their predictions were compared against the analytical solutions. The codes seem to be in good agreement with each other as well as with the analytical solution. The details on this study will be provided in chapter 3.

Chapter 4 concentrates on the simulation of Comprex under various operating conditions. The simulation run conditions are chosen from the only experimental testing work available on the Comprex, described in the ref. [32]. Additionally, attempts have been made to investigate the performance of Comprex under variable speed and load range of the engine. It is quite challenging to predict the properties of Comprex based on the numerical simulation, considering the limitations to account for aerodynamic losses in the ports and techniques to impose proper boundary conditions. However, the variable speed investigation gives valuable insights into the pressure fields established at various locations during the different speed cycles.

The main objective of this thesis is to simulate the pocket combination used in PWS and identify their effects on off-design performance. A simple lumped capacitance model has been developed to integrate pocket density and pressure. The pocket pressure and temperature are updated using simple Euler integration on the lumped capacitance model of the pockets. The wall-pocket simulation modules have been incorporated in the four-port wave rotor configuration to simulate the PWS with pockets. The simulation results have been compared with the available experimental data. It has been observed that the wave rotor analysis codes can satisfactorily predict the performance of PWS with pockets.

2. NUMERICAL TOOLS FOR WAVE ROTOR ANALYSIS

Computational analysis tools used in this study are quasi-one-dimensional wave action models implemented in FORTRAN for numerical simulation of the unsteady flow field inside the channels of wave rotor devices and performance assessment of different wave rotor configurations. The code tracks the progress of wave rotor channels as they rotate about the circumference, past inlet and outlet ports. The code also provides the approach to follow just one channel, but gas dynamic modeling of the internal flow is exactly of the same fashion. Multichannel model of the code has been used throughout this study. Three versions of the code (NASA Q1D, SCW1D-A and SCW1D-B) have been used in this work. However, all of the versions march the same way.

The channel is discretized into volumetric cells, and the conservation laws of mass, momentum, and energy are applied to every cell as a finite volume. Appropriate pressure and temperature boundary conditions are imposed at the passage ends for solid walls, inflow and outflow ports, fuel injection ports, valves, and wall-pockets. The available version of NASA Q1D is capable of incorporation six ports, three on each side, and was intended for non-reacting flow, although versions of Q1D for four ports on each side and for combustion are also well-known. The SCW1D versions can accommodate any number of ports with small modifications due to the modularity of programs. The programs are intended to simulate the performance of wave rotors by solving one-dimensional mass, momentum, and energy conservation equations throughout the cycle while utilizing numerical routines to incorporate the effects of additional physical phenomena such as friction, heat transfer, leakage effects, incidence losses, and partial opening of the channels while moving past the port edges. The flux through each cell is integrated using Roe's integration technique with the end goal is that mass, momentum, and energy are conserved throughout each cycle. At the end of each cycle, the boundary conditions are updated to reflect changes in the PWS external environment so that at the end of several cycles, the program may converge to a realistic solution.

2.1 Governing Equations

The equations used to describe the unsteady, compressible, viscous gas-dynamic flow within a wave rotor passage are the one-dimensional Euler equations in time and one space co-ordinate (hence 'one-dimensional'). The code integrates governing equations numerically using the Lax-Wendroff technique. Roe's approximate Riemann solver is used to calculate the flux across each cell boundary. The integration of Lax-Wendroff scheme with Riemann solver provides the precise shock-capturing capability to the code.

The governing equations in conservation form are written as

$$\frac{\partial \underline{w}}{\partial t} + \frac{\partial \underline{F}(\underline{w})}{\partial x} = \underline{S}(\underline{w}) \tag{2.1}$$

where,

$$\underline{w} = \begin{bmatrix} \rho \\ \rho u \\ \frac{p}{\gamma(\gamma-1)} + \frac{\rho u^2}{2} \end{bmatrix} \tag{2.2}$$

and,

$$\underline{F} = \begin{bmatrix} \rho u \\ \frac{p}{\gamma} + \rho u^2 \\ u(\frac{p}{(\gamma-1)} + \frac{\rho u^2}{2}) \end{bmatrix} \tag{2.3}$$

The code accepts non-dimensional form of the governing equations. Stagnation state at the wave rotor inlet port is generally used as the reference state, p^*, ρ^*, γ, and a^* for deriving non-dimensional form of the governing equations, where a^* is the local speed of sound and γ is the ratio of specific heats. In this form, the perfect gas law is written as $p = \rho T$. The distance has been scaled using the passage length L, and the time has been scaled by the wave transit time, $\frac{L}{a^*}$.

The source vector $\underline{S}(\underline{w})$ accounts for additional physical phenomena such as friction (viscous effects), heat transfer from the passage walls to the gas, leakage from the passage ends to the hollow center cavity, and to the ports. In SCW1D versions, additional terms to

account for passage-to-passage leakage (radial leakage) have been incorporated. Leakage is expected to occur at the passage ends which are exposed to the ports and pockets. In computational terms, the leakage is modeled at the first and last computational cells where port, pockets and leakage volume boundary conditions are specified. Hence, for the internal region (excluding the first and last computational cells) where the leakage is not specified, the source term can be written as,

$$\underline{S}^{int} = \begin{bmatrix} 0 \\ \sigma_2 |\rho u|^{0.75} u \\ \frac{\sigma_2}{\gamma - 1} (\frac{D_h}{2h}) Pr^{-\frac{2}{3}} (T - T_{wall}) |\rho u|^{0.75} \end{bmatrix} \tag{2.4}$$

Where D_h is the passage hydraulic diameter, h is the passage height, Pr is the Prandtl number, T is the gas static temperature, and T_{wall} is the passage wall temperature. The term σ_2 is semi-empirically derived constant based on the passage geometry and reference conditions, which is given as

$$\sigma_2 = -5.448 (\frac{L}{D_h})^{1.081} (\frac{\rho^* a^* L}{\mu})^{-0.3953} \tag{2.5}$$

The dynamic viscosity μ is assumed constant. The third term of the source vector in equation 2.4 is derived from the Reynolds-Colburn heat transfer, skin friction analogy with heat transfer assumed to occur only from the upper and lower surfaces of the passage and not from the sides.

At the passage ends (first and last computational cells in the computing domain), where leakage is modeled, the source term is written as

$$\underline{S}^{leak} = \underline{S}^{int} + \begin{bmatrix} -C_D \gamma_2 (\frac{2\delta_{leak}}{h\Delta x}) \sqrt{p\rho} f(\frac{P_{cav}}{p}) \\ 0 \\ -C_D \frac{\gamma_2}{\gamma - 1} (\frac{2\delta_{leak}}{h\Delta x}) T^0 \sqrt{p\rho} f(\frac{P_{cav}}{p}) \end{bmatrix} \tag{2.6}$$

Where the function $f(\frac{P_{cav}}{p})$ is St. Venant's orifice equation, P_{cav} is the pressure of central cavity, δ_{leak} is the leakage gap between the rotor and endplates, Δx is the non-dimensional numerical spacial step used in the computational scheme (here numerical spacial step or

grid spacing is assumed to be much greater than the leakage gap), $\gamma_2 = \sqrt{\frac{2}{\gamma-2}}, T^0$ is the gas stagnation temperature and C_D is the seal discharge coefficient assumed to be 0.8. If the cavity pressure is greater than cell pressure, then the pressure ratio in equation 2.6 is inverted, sign changes, and p, ρ, T^0 become those of the central cavity. Equation 2.6 is only applied to the first and last computational cells in the computing domain.

2.2 Computational Scheme

The computational tools integrate equation 2.1 numerically using the conservation form of the Lax-Wendroff scheme as described in ref. 1

$$\underline{w}_{\mathrm{i}}^{n+1} = \underline{w}_{\mathrm{i}}^{n} - (\underline{f}_{\mathrm{i}+\frac{1}{2}}^{n} - \underline{f}_{\mathrm{i}-\frac{1}{2}}^{n})\frac{\Delta t}{\Delta x} + \underline{s}_{\mathrm{i}}^{n}\Delta t \tag{2.7}$$

where numerical flux estimate $\underline{f}_{\mathrm{i}+\frac{1}{2}}^{n}$ is

$$\underline{f}_{\mathrm{i}+\frac{1}{2}}^{n} = \frac{\underline{F}_{\mathrm{i}+1}^{n} + \underline{F}_{\mathrm{i}}^{n}}{2} - \frac{\underline{\phi}_{\mathrm{i}+\frac{1}{2}}^{Roe}}{2} + \frac{\Delta t}{4}([A]_{\mathrm{i}+1}^{n}.\underline{S}_{\mathrm{i}+1}^{n} + [A]_{\mathrm{i}}^{n}.\underline{S}_{\mathrm{i}}^{n}) \tag{2.8}$$

and numerical source $\underline{s}_{\mathrm{i}}^{n}$ is

$$\underline{s}_{\mathrm{i}}^{n} = \frac{1}{2}(3\underline{S}_{\mathrm{i}}^{n} - \underline{S}_{\mathrm{i}}^{n-1}) \tag{2.9}$$

The term $\underline{\phi}_{\mathrm{i}+\frac{1}{2}}^{Roe}$ in equation 2.8 refers to the flux limited dissipation based on Roe's approximate Riemann solver for equation 2.1 without a source vector. The matrix [A] is the Jacobian of the flux vector $\underline{F}$. The superscript n indicates the discrete temporal index $n\Delta t$ and the subscript i indicates the spatial index iΔx. Unless otherwise stated, all results in this work used a ratio of $\frac{\Delta t}{\Delta x} = 0.2$, with $\Delta x = 0.02$.

The programs had to undergo some organizational changes, as described in K. Smith [33], in order to increase the speed of computation, to improve the security of the data used by the program, to allow multiple paths of program development, to include conversion between physical properties and physical dimensions and non-dimensional inputs and outputs, and to execute the entire program as a subroutine of a larger control program. Besides, minor changes have been made during the course of this work so that the program compiles using

the latest FORTRAN compiler. Burner and valve modules were turned off since the focus of this work was on PWS wall-pockets modeling. A module has been added to simulate the wall-pockets using lumped volume technique.

The analysis mainly consists of three FORTRAN modules, encompassing the boundary condition computations, the Roe's characteristic scheme for the Euler equations, and the input/output/control software. The input file contains all program inputs in non-dimensional form. The input parameters are nondimensionalized using the standard atmospheric states, passage length, and wave transit time. The program inputs are absolute stagnation pressures and temperatures at assumed inflows, static pressures at assumed outflows, wave rotor dimensions such as port locations, port opening, and closing timings, leakage volumes rotor radius and rotational speed, properties of the operating medium, and other variables, parameters and switches as per the requirement of specific computational routine.

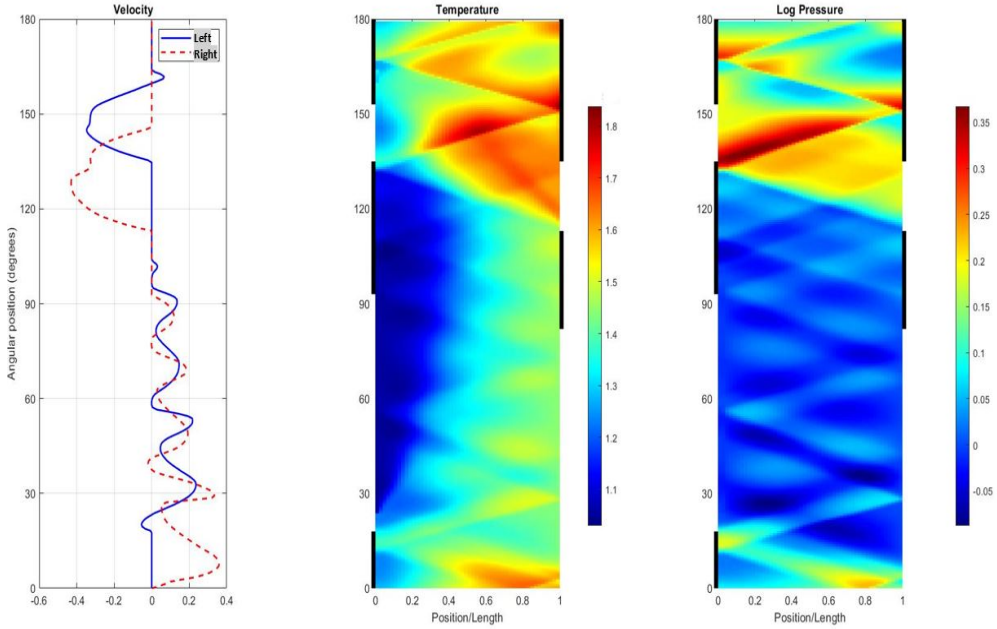

Figure 2.1. Simulation of a pocketless four-port wave rotor pressure wave supercharger. The first diagram shows the velocity profile of the flow as the channels progress in time. The second diagram envisions temperature distribution with inflow interfaces. The third diagram pictures the log-pressure distribution over the cycle showing the timing close to optimum for wave arrivals matched with port transitions.

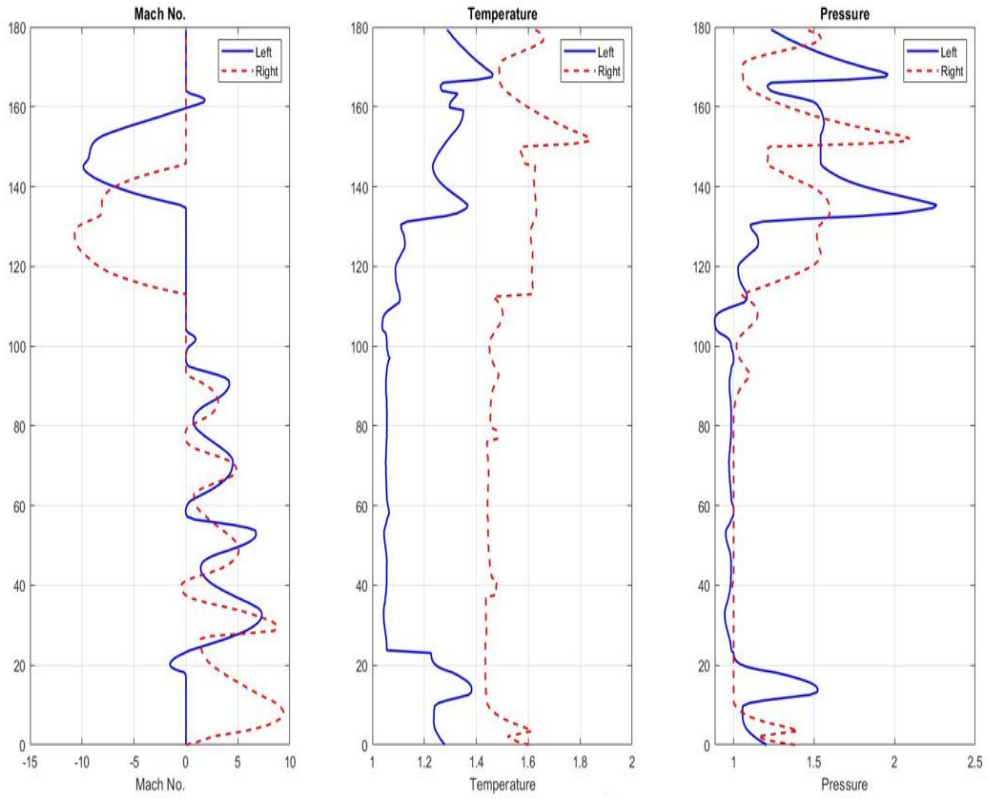

Figure 2.2. Mach Number, Temperature, and Pressure profiles over the cycle

The results are stored in an output file, which is used for post-processing and data visualization. A MATLAB script is developed to extract the data from the output file and visualize it. Figures 2.1 and 2.2 show post-processing of the results produced by a four-port pressure wave supercharger simulation.

3. VERIFICATION OF COMPUTATIONAL CODES FOR BASIC UNSTEADY FLOW SIMULATIONS

Computational programs used for wave rotor analysis use Lax-Wendroff scheme to solve the governing equations numerically. Even if the fundamental numerical procedure is the same for all versions of the code, the original code has gotten through significant changes and modifications. Also, the modeling of some physical phenomena such as flow incidences is slightly different in SCW1D versions from that in NASA Q1D. It is important for version control to track the reasons behind any discrepancies even if the difference is negligible.

For dynamic wave rotor analysis, understanding the dynamics of shock waves, which take place inside the wave rotor channels is essential. The codes have been used to simulate basic unsteady flow processes in order to check the performance of different versions of the code and identify the parameters conducive to introducing the difference in the ultimate results of the complex simulations such as PWS simulation. This study also serves as the verification of different versions of the code for basic unsteady flow processes. The SCW1D A and B versions compute same results when the passages are axial. Hence, the results produced by SCW1D-A program have been compared with the results computed by the NASA Q1D program.

3.1 Dynamics of the Shock Waves inside the Wave Rotor Channels

An unsteady pressure wave traveling in a wave rotor channel can be viewed as a dynamic one-dimensional shock wave, moving in a straight rectangular duct with constant cross-section. The dynamics of such moving shock waves can be approximated with the Rankine-Hugoniot equations. The properties in front of a shock wave can be expressed in terms of the properties behind the shock wave, using Rankine-Hugoniot relations in shock frame of reference. To derive theoretical equations for moving shock, we can proceed in shock frame of reference by considering the shock front as stationary and the medium in front of the shock wave moving towards it with a velocity relative to it. The frame of reference can be later changed to actual (observer or lab) frame of reference once we obtain the difference between the velocities of the regions ahead and behind the shock front. This difference is constant

in both shock frame of reference and observer's frame of reference. Figure 3.1, taken from ref. [34], shows the schematic of stationary and moving shock wave. The region in front of the shock front is denoted as subscript 1 and the region behind it is denoted as subscript 2. The velocities relative to the shock wave, of regions in front of and behind the shock wave are denoted by u1 and u2 respectively. Whereas W is the velocity of the shock wave.

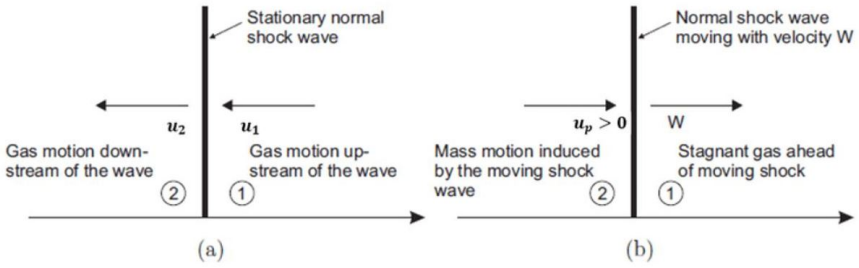

Figure 3.1. Schematic of Stationary (a) and Moving (b) Shock Waves

In the shock frame of reference, the continuity, momentum, and energy conservation equations are, respectively

$$\rho_1 u_1 = \rho_2 u_2 \tag{3.1}$$

$$p_1 + \rho_1 u_1^2 = p_2 + \rho_2 u_2^2 \tag{3.2}$$

$$h_1 + \frac{u_1^2}{2} = h_2 + \frac{u_2^2}{2} \tag{3.3}$$

Rearranging the conservation equations and after some mathematical transformation, the following relations can be obtained for the ratios of properties across the shock front in terms of the Mach number of the upstream flow in the shock frame of reference.

Static pressure ratio

$$\frac{p_2}{p_1} = \frac{2\gamma M^2 - (\gamma - 1)}{\gamma + 1} \tag{3.4}$$

Stagnation pressure ration

$$\frac{P_2}{P_1} = [\frac{(\gamma + 1)M^2}{(\gamma - 1)M^2 + 1}]^{\frac{\gamma}{\gamma - 1}} [\frac{\gamma + 1}{2\gamma M^2 - (\gamma - 1)}]^{\frac{1}{\gamma - 1}} \tag{3.5}$$

Static temperature ratio

$$\frac{t_2}{t_1} = \frac{[2\gamma M^2 - (\gamma - 1)][(\gamma - 1)M^2 + 2]}{(\gamma + 1)^2 M^2} \tag{3.6}$$

Stagnation temperature ratio

$$\frac{T_2}{T_1} = 1 \tag{3.7}$$

Density ratio

$$\frac{\rho_2}{\rho_1} = \frac{(\gamma + 1)M^2}{(\gamma - 1)M^2 + 2} \tag{3.8}$$

Mach Number in front of the shock

$$M_2^2 = \frac{(\gamma - 1)M^2 + 2}{2\gamma M^2 - (\gamma - 1)} \tag{3.9}$$

Here M is the Mach number in front of the shock wave. The above equations have been used to calculate the properties across the shock waves. In this section, the computational wave rotor analysis tools have been used to simulate the optimum duct filling and optimum duct emptying processes. Results produced by the codes have been compared with the analytical solutions for the unsteady duct filling and duct emptying processes. The curved-passage version of the SCW1D code gives the same results as the straight-passage version when the passage curvature angle is set to zero. The codes seem to be in good agreement with each other and with the analytical solution.

3.2 Optimum Duct Filling Process

The process is initiated as a result of pressure differential, which upon sudden duct opening, sets up compression wave inside the duct, which is a shock wave if the opening process is instantaneous. This shock wave reflects as a shock wave from the closed end of the duct. Under optimum design, the duct must close at the instant when the reflected shock wave reaches the open end of the duct. Here the optimum result refers to the maximum residual pressure ratio which can be obtained in the duct at the end of the process.

Consider air stored in a reservoir at certain stagnation conditions flows into a constant area, frictionless, channel, such that it enters the channel at the same static pressure and temperature as air moving in the channel behind the shock wave that it creates. The air in the channel is initially at static pressure 101.325 kPa, and static temperature 300 K. This is similar to the flow into a wave rotor channel, but without considering the rotation of the wave rotor.

Here, the subscripts 1 and 2 indicate the states ahead and behind the shock wave. It is intended to avoid generating a contact interface which can interact with the reflected wave. For this, the entropy of air in the reservoir is chosen to be exactly matched with the air behind the shock. Thus, the subscript 2 also indicates the stagnation state in the reservoir, which will be used as the boundary condition. The code was tested by using a specific case, with the initial shock strength set at a shock mach number of 1.45.

Initially, the air is at $p_1 = 101.325$ kPa and $t_1 = 300$K, and we assume all the air has constant specific heat ratio of 1.4. We also have the static temperature ratio across the normal shock wave generated in the duct.

$$\frac{t_2}{t_1} = 1.29$$

The Mach number in front of the shock wave can be calculated using equation 3.6. All other properties behind the shock wave in shock frame of reference can be expressed in terms of Mach number in front of the shock wave. Using the other relations described in section 3.1, the following properties can be calculated

$$T_2 = 387K$$
$$p_2 = 233.08244 \text{ kPa}$$
$$u_1 = 504.86793 \text{ m/s}$$
$$u_2 = 283.11357 \text{ m/s}$$
$$a_1 = 347.18871 \text{ m/s}$$
$$a_2 = 394.33057 \text{ m/s}$$

Here, the velocity is denoted by u, and a refers to the local speed of sound. The local speed of sound in the medium ahead of the shock wave, denoted by a_1 is used as the reference speed of sound.

Now, switching to wave rotor frame of reference,

$$u_{WR} = |u_1 – u_2| = 221.75436 \text{ m/s}$$
$$M_{WR} = u_{WR}/a_2 = 0.56235$$

Hence, the non-dimensional stagnation pressure and temperature at the open end of the channel can be calculated and used as the boundary conditions for the code to simulate the optimum duct filling process.

$$T_{WR}/t_1 = 1.37159$$
$$P_{WR}/p_1 = 2.85112$$

And the non-dimensional velocity calculated by the code should be,

$$u_{WR}/a_1 = 0.638$$

Since the code accepts the input parameters in non-dimensional form, the non-dimensional pressure and temperature are used as boundary conditions to simulate the optimum duct filling case. In this particular case, friction and rotation have been turned off. Further case studies included alternative consideration of friction and rotation.

3.2.1 Optimum Frictionless Duct Filling Process

Wave rotor analysis tools can predict the non-dimensional velocity to be same as the analytical solution. Table 3.1 shows the velocity and mass flux calculated by the two versions. The x-axis in line plots indicates the non-dimensional properties and x-axis in x-t diagrams indicates the position divided by length

Table 3.1. Velocity and Mass Flux results for optimum duct filling process

Parameters/Code	NASA Q1D	SCW1D	Analytical
MF	1.968	1.967	
Velocity	0.637	0.637	0.638

Figures 3.3 and 3.4 show the temperature and pressure distribution during the process of duct filling. The open-end of the duct is closed at the instance when the shock wave

reflected from the closed-end arrives at the open-end. It can be viewed in the log-pressure diagram produced by the two codes. The codes account for gradual passage opening effects. Considering the passage width, failure to completely close the passage at the arrival of reflected wave gives rise to the residual waves in the passage.

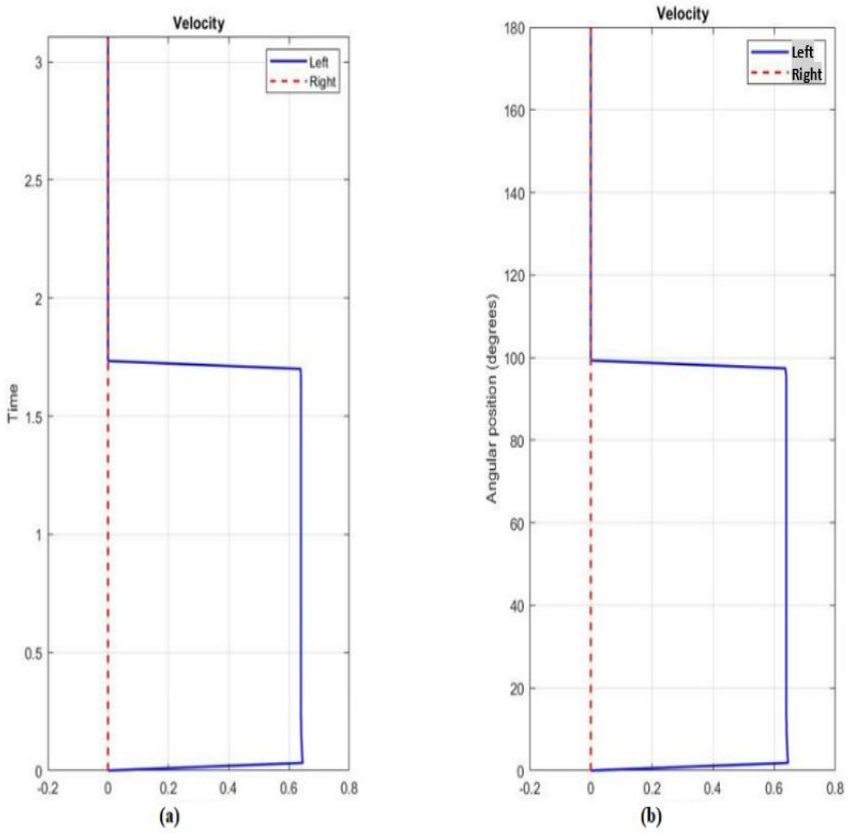

Figure 3.2. Velocity profile for optimum duct filling process without considering friction and rotation by (a) NASA Q1D, (b) SCW1D.

In order to distinguish the results of two codes, different nomenclature has been used for the y-axis. It should be noted that the y-axis indicates the progress of a wave rotor channel as it travels along the circumference of the rotor. During the post-processing of NASA Q1D program, the rotation is shown in radians, whereas in case of the SCW1D post-processing, the rotation is shown in degrees

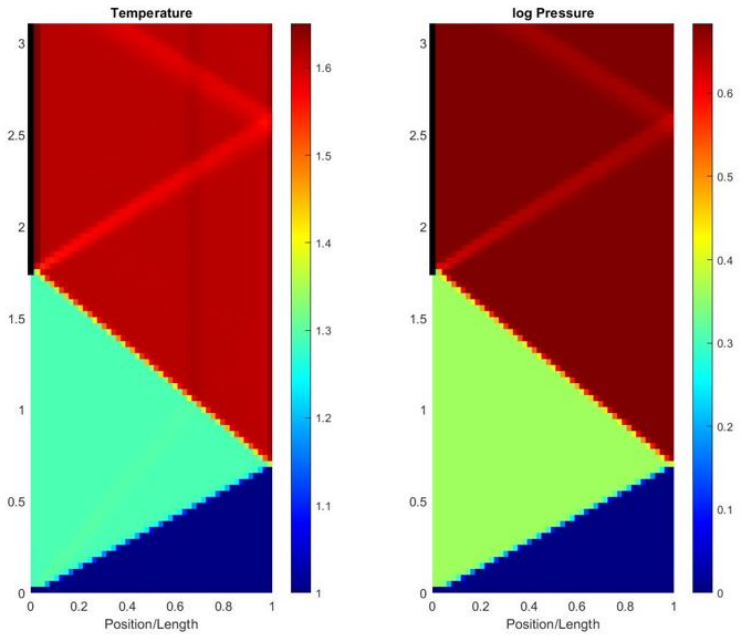

Figure 3.3. Temperature and Pressure distribution during the optimum duct filling process, computed using the NASA Q1D software

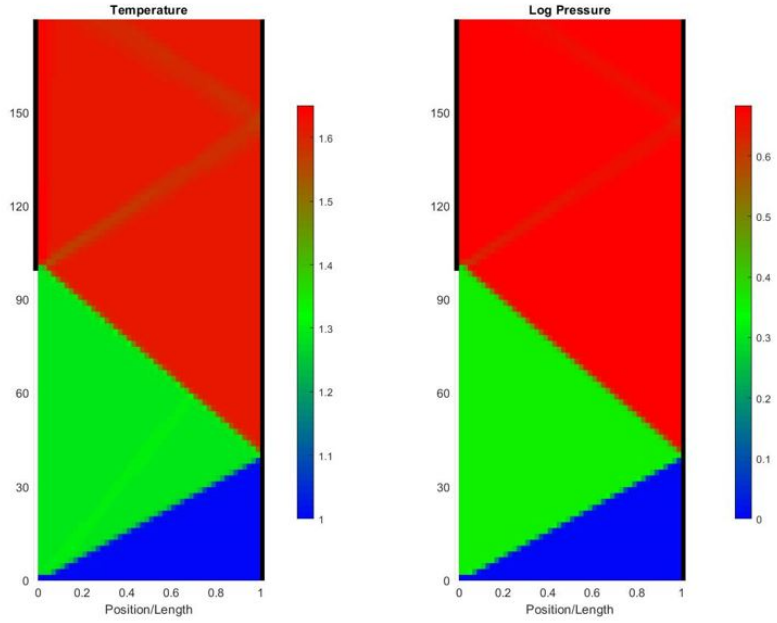

Figure 3.4. Temperature and Pressure distribution during the optimum duct filling process, computed using the SCW1D software

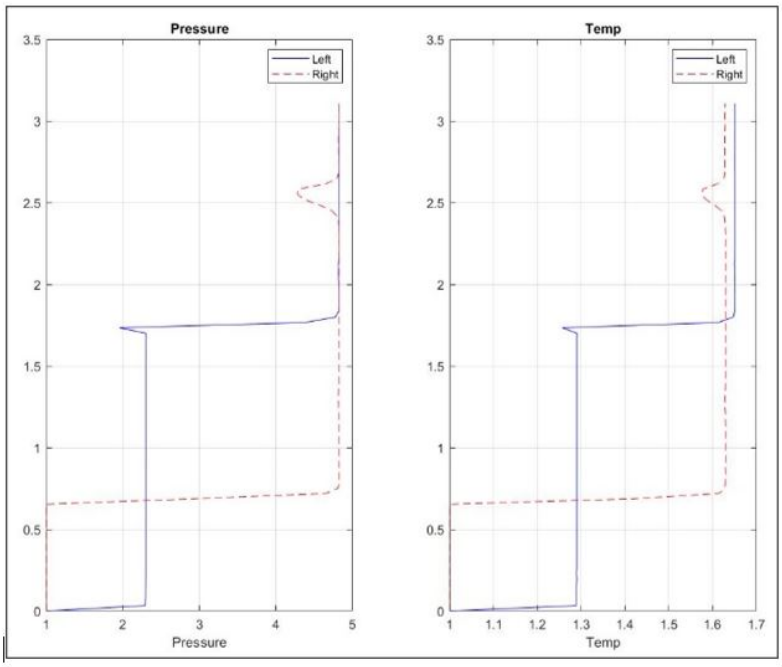

Figure 3.5. Pressure and Temperature variation, computed by NASA Q1D program

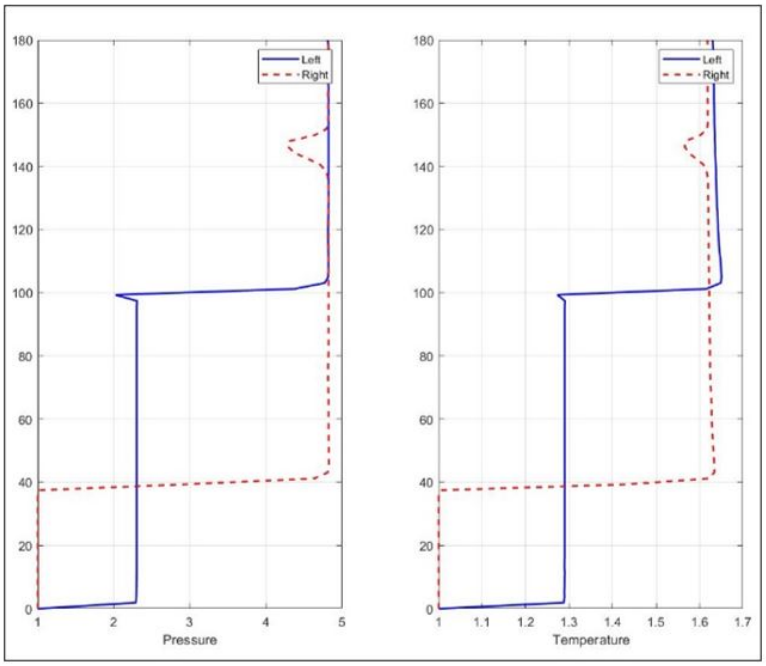

Figure 3.6. Pressure and Temperature variation, computed by SCW1D program

Figures 3.5 and 3.6 show the variation of temperature and pressure during the process. By comparing the results of two programs, it is clear that the programs can compute the results as per expectations.

3.2.2 Optimum Duct Filling Process with Friction

For computational simplicity, the downstream temperature and pressure boundary conditions are set to be the same as those in frictionless duct filling process discussed in the previous subsection. The codes compute mass flux from the pressure and temperature boundary conditions. Results predicted by NASA Q1D and SCW1D (A and B) have been compared with each other to verify that the friction modeling does not introduce any discrepancies in the results. Velocity, pressure, and temperature distribution computed by two codes can be seen in the figures below.

Table 3.2. Velocity and Mass Flux results for duct filling process with friction

Parameters/Code	NASA Q1D	SCW1D	Analytical
MF	1.858	1.858	
Velocity	0.638	0.638	0.638

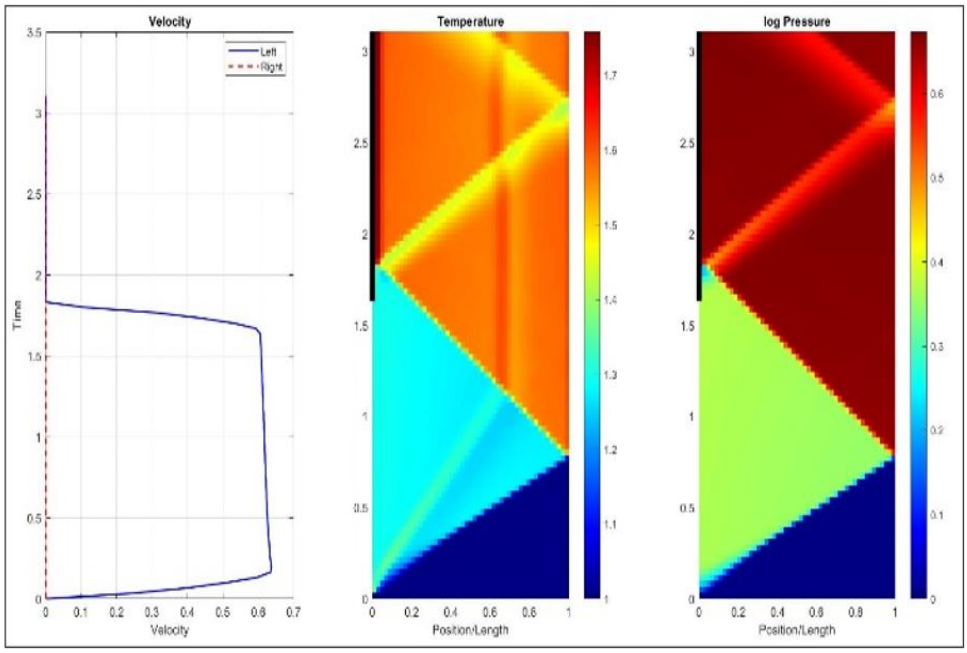

Figure 3.7. Velocity profile, Temperature and Pressure distribution during the duct filling process with friction, computed by NASA Q1D program

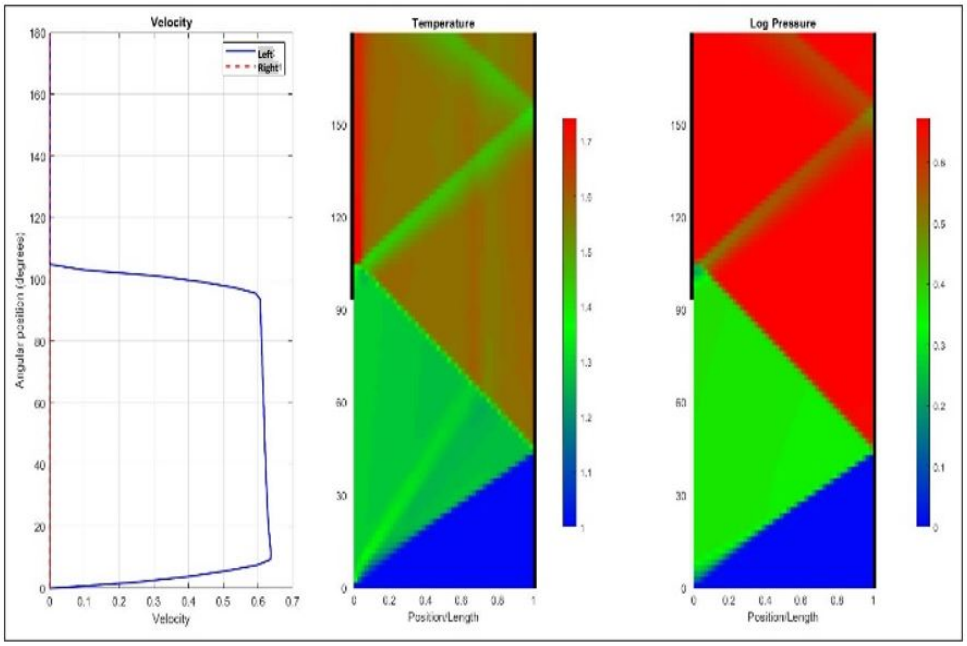

Figure 3.8. Velocity profile, Temperature and Pressure distribution during the duct filling process with friction, computed by SCW1D program

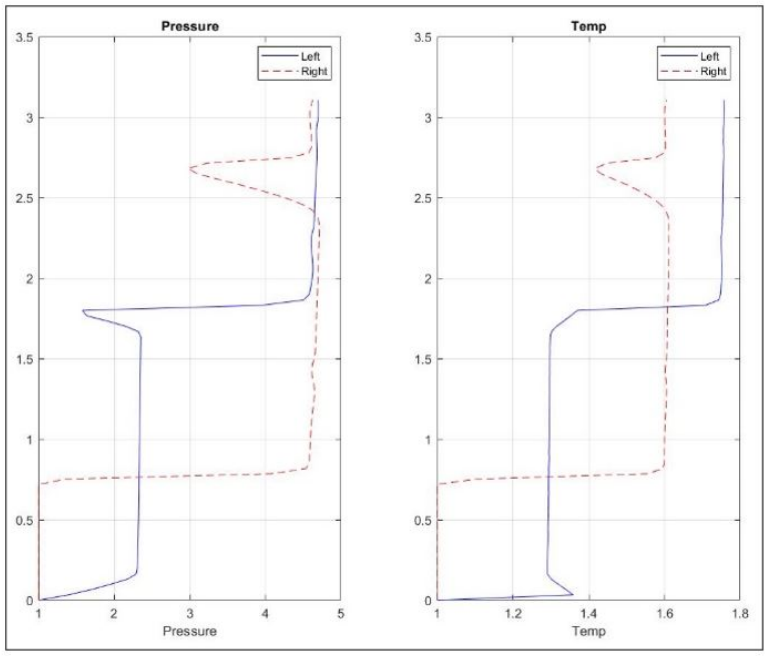

Figure 3.9. Pressure and Temperature variation during the duct filling process with friction, computed by NASA Q1D program

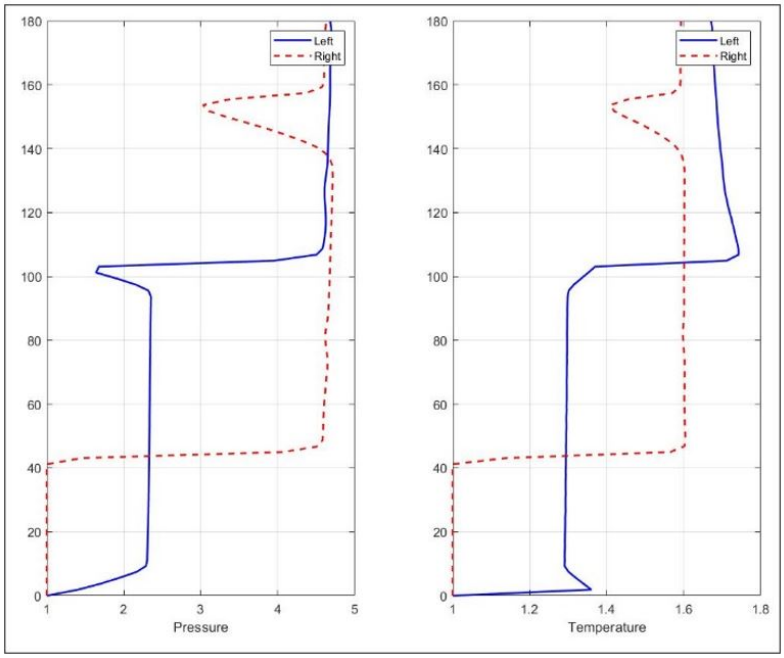

Figure 3.10. Pressure and Temperature variation during the duct filling process with friction, computed by SCW1D program

3.2.3 Optimum Duct Filling Process with Rotation

While simulating the optimum duct filling process with rotation, it is essential to use the correct inlet port duct angle. The duct angle, Beta, plays a crucial role in mixing and turning calculations. It is directly used to obtain mixed absolute static conditions. The parameter ALPH is the difference (in radians) between the actual duct angle and the mixed port flow. The parameter ALPH can serve as a measure of difference between the mixing calculations performed by the programs. Figure 3.11 shows the inlet port and the approaching mixed relative flow. We can calculate the corresponding duct angle for velocity output (u_{rel}) and linear speed of the rotor (ωR) from the velocity triangle. Optimum duct angle for the duct filling cases discussed above is calculated as

$$tan(\beta) = \frac{\omega R}{u_{rel}}$$

For non-dimensional rotor radius 0.40327, angular speed 0.28704, and relative velocity predicted by the duct filling simulations, the optimal duct angle is

$$\beta = 0.1806$$

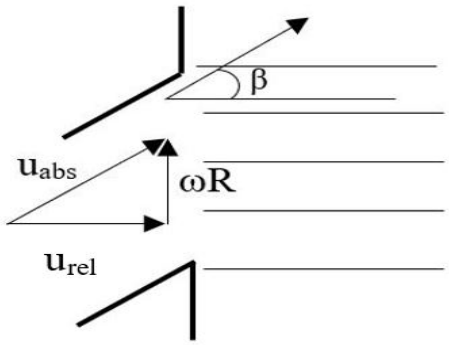

Figure 3.11. Mixed relative flow at the inlet port

Table 3.3. Velocity and Mass Flux results for duct filling process with rotation

Parameters/Code	NASA Q1D	SCW1D	Analytical
MF	1.950	1.949	
Velocity	0.634	0.634	0.634
ALPH	-0.000	-0.000	

Figures 3.12 and 3.13 show the velocity profile, temperature and pressure distribution during the process of duct filling with rotation.

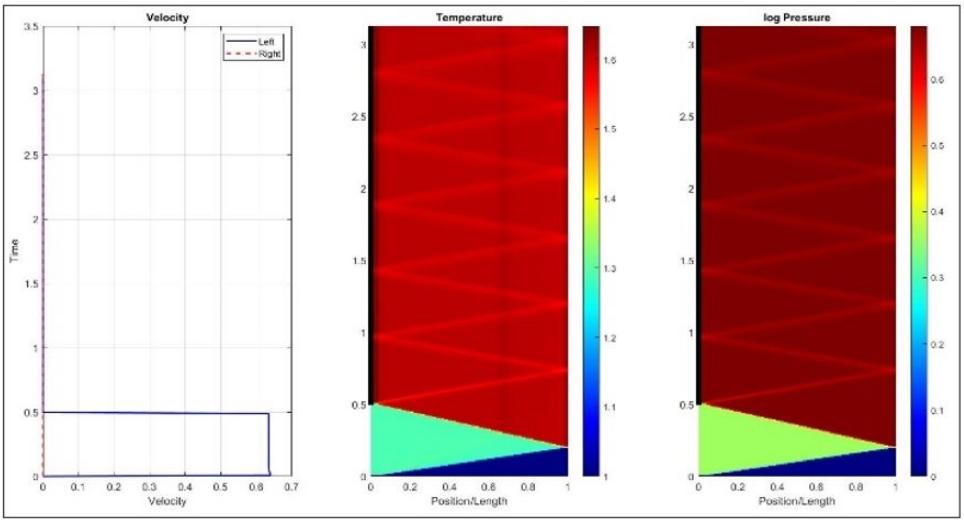

Figure 3.12. Velocity profile, Temperature and Pressure distribution during the duct filling process with rotation, computed by NASA Q1D program

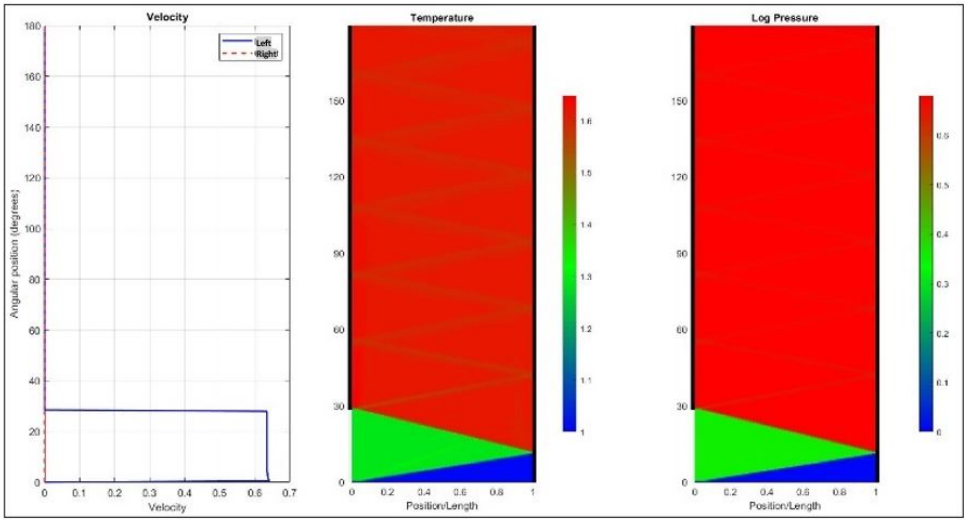

Figure 3.13. Velocity profile, Temperature and Pressure distribution during the duct filling process with rotation, computed by SCW1D program

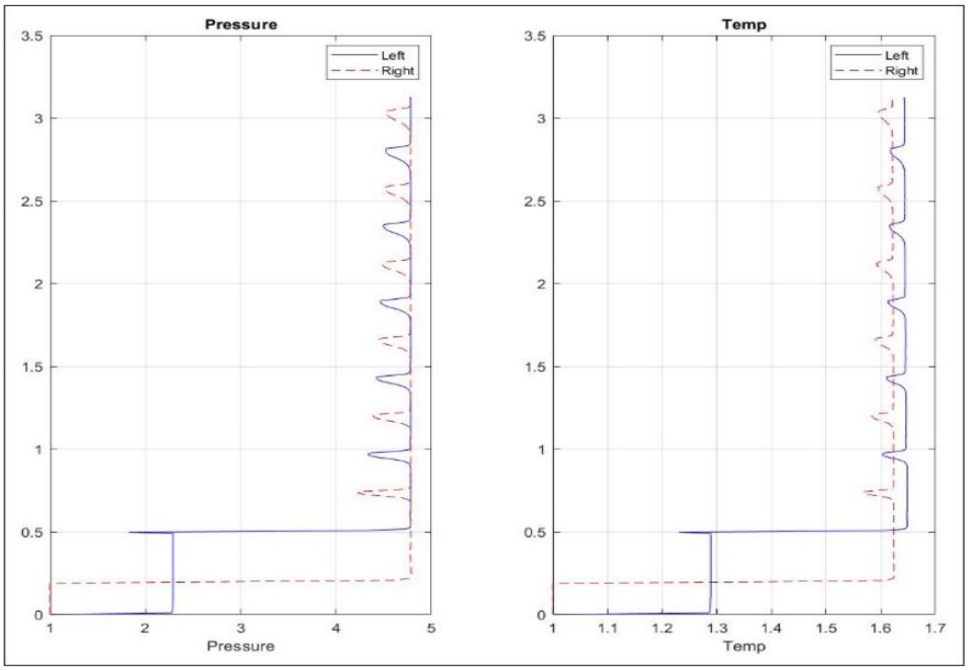

Figure 3.14. Pressure and Temperature variation during the duct filling process with rotation, computed by NASA Q1D program

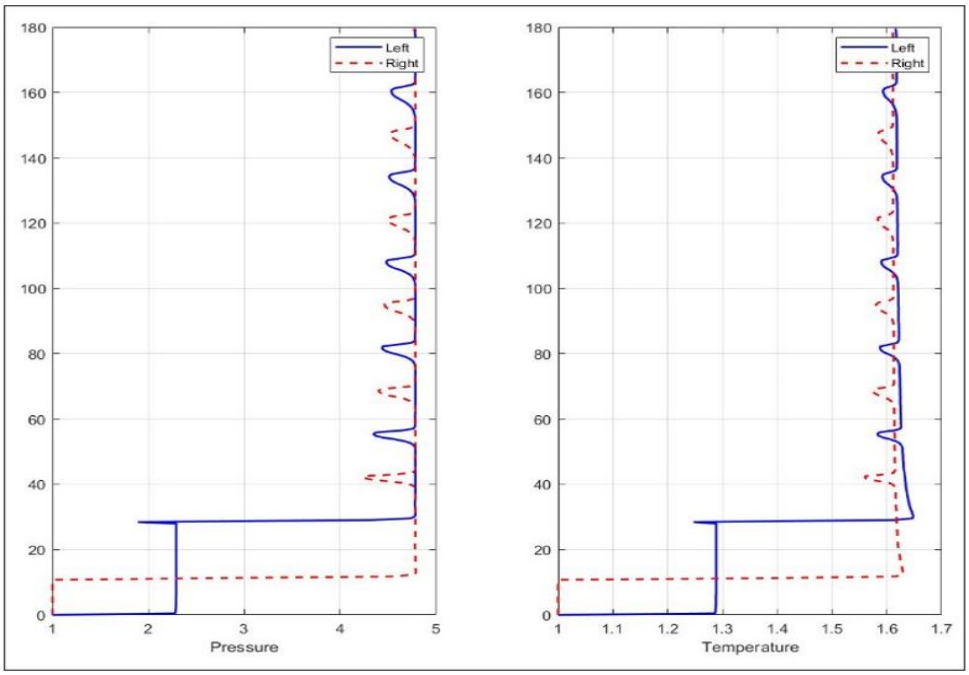

Figure 3.15. Pressure and Temperature variation during the duct filling process with rotation, computed by SCW1D program

3.3 Optimum Duct Emptying Process

The process is started when one end of a duct initially filled with high-pressure gas is opened to a low-pressure ambient. Outflow occurs by virtue of an expansion wave, which propagates into the duct. This expansion wave is reflected from the closed end as an expansion wave. For optimum duct emptying, the duct should close at the instant when the reflected wave reaches the open end of the duct. Here the optimum result refers to the minimum residual pressure that will be present in the duct at the end of the process.

Consider a constant area, frictionless duct, initially pressurized at 200 kPa and 300 K. The right end of the duct is suddenly opened to static pressure 100 kPa and 288 K. It should be noted that, the subscript 0 refers to the state inside the duct and subscript e refers to the state outside the duct.

The properties of air inside the duct are used as the reference states to nondimensionalize the properties. The non-dimensional sonic speed, velocity, pressure and temperature outside the duct can be calculated.

$$a^* = \frac{a_e}{a_0}$$
$$u^* = \frac{u_e}{u_0}$$
$$p^* = \frac{p_e}{p_0}$$
$$t^* = \frac{t_e}{t_0}$$

From the method of characteristics,

$$a^* + 0.2u^* = 1$$

Using isentropic relations,

$$a^* = (t^*)^{\frac{1}{2}} = 0.90572$$
$$a_e = a^*.a_0 = 347.7 \text{ m/s}$$
$$u^* = 0.47140$$
$$u_e = u^*.a_0 = 163.67 \text{ m/s}$$
$$M_e = \frac{u^*}{a^*} = 0.52047$$

The codes should calculate the non-dimensional velocity equal to 0.47140 and the non-dimensional Mach number 0.52047, when provided given pressure and temperature boundary conditions.

3.3.1 Optimum Frictionless Duct Emptying Process

The non-dimensional pressure 0.5 and non-dimensional temperature 0.96 have been used as the boundary conditions to simulate the optimum duct emptying process.

Table 3.4 shows the velocity and mass flux results for the process.

Table 3.4. Velocity and Mass Flux results for optimum duct emptying process

Parameters/Code	NASA Q1D	SCW1D	Analytical
MF	0.492	0.491	
Velocity	0.471	0.471	0.471

Figures 3.16 and 3.17 show the velocity profile, temperature and pressure distribution during the process of optimum duct emptying.

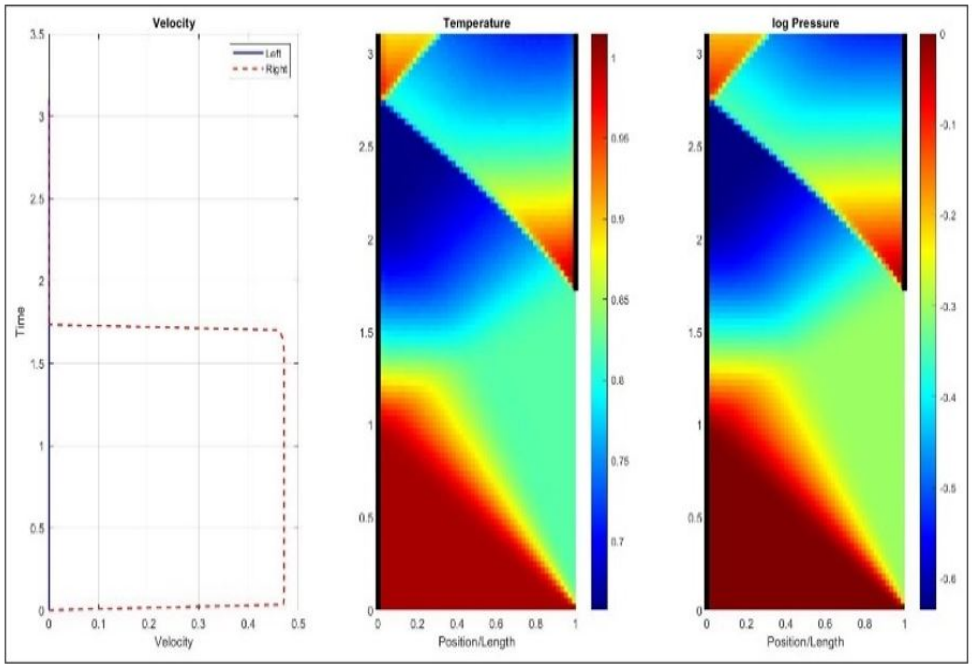

Figure 3.16. Velocity profile, Temperature and Pressure distribution during the optimum duct emptying process, computed by NASA Q1D program

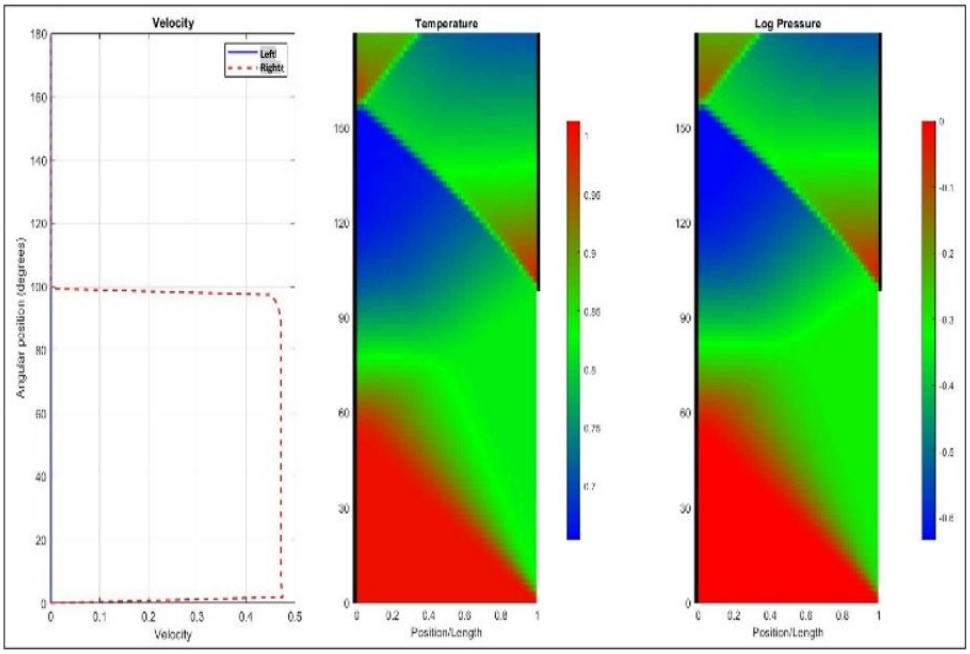

Figure 3.17. Velocity profile, Temperature and Pressure distribution during the optimum duct emptying process, computed by SCW1D program

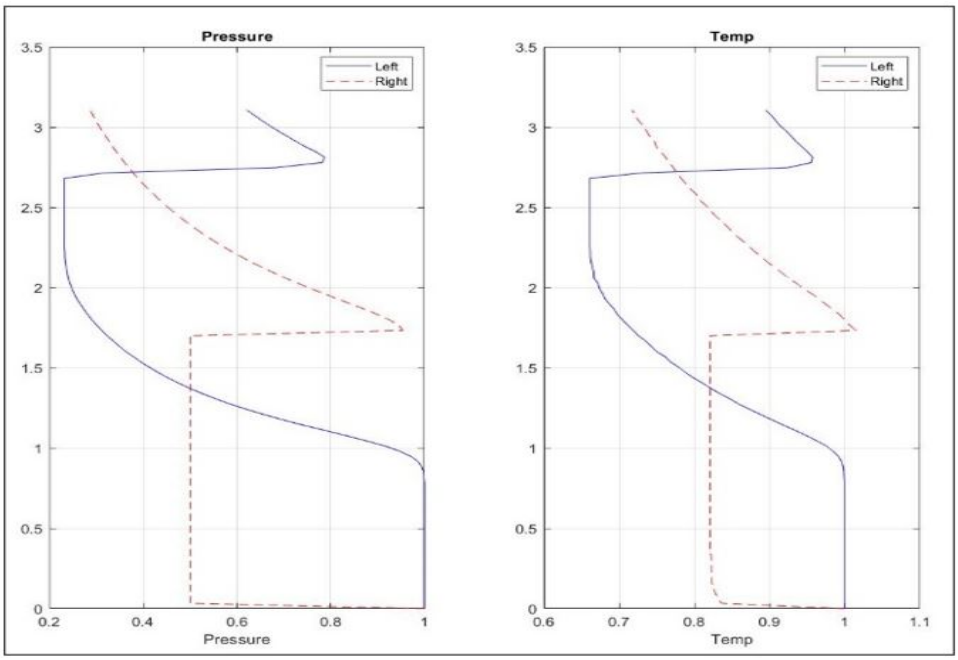

Figure 3.18. Pressure and Temperature variation during the optimum duct emptying process, computed by NASA Q1D program

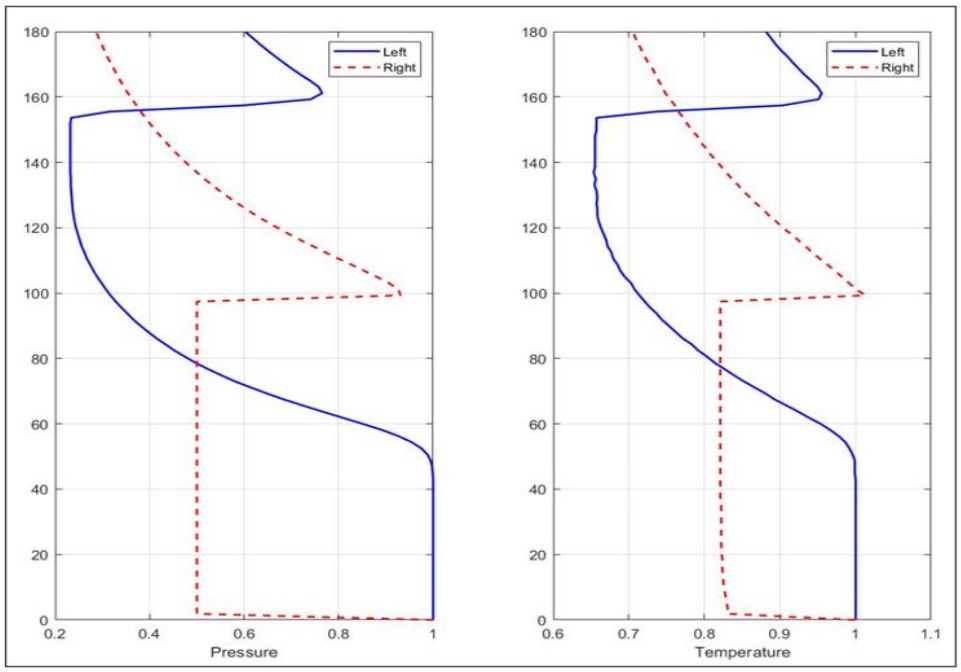

Figure 3.19. Pressure and Temperature variation during the optimum duct emptying process, computed by SCW1D program

3.3.2 Optimum Duct Emptying Process with Friction

The approach to simulate the duct emptying process with friction is similar to the duct filling process with friction. The results predicted by NASA Q1D and SCW1D (A and B) programs have been compared with each other to inspect the friction modeling. Table 3.5 shows the result for duct emptying process with friction. Figures 3.20 and 3.21 show the velocity profile, temperature and pressure distribution during the optimum duct emptying process with friction.

Table 3.5. Velocity and Mass Flux results for duct emptying process with friction

Parameters/Code	NASA Q1D	SCW1D	Analytical
MF	0.521	0.520	
Velocity	0.472	0.472	0.471

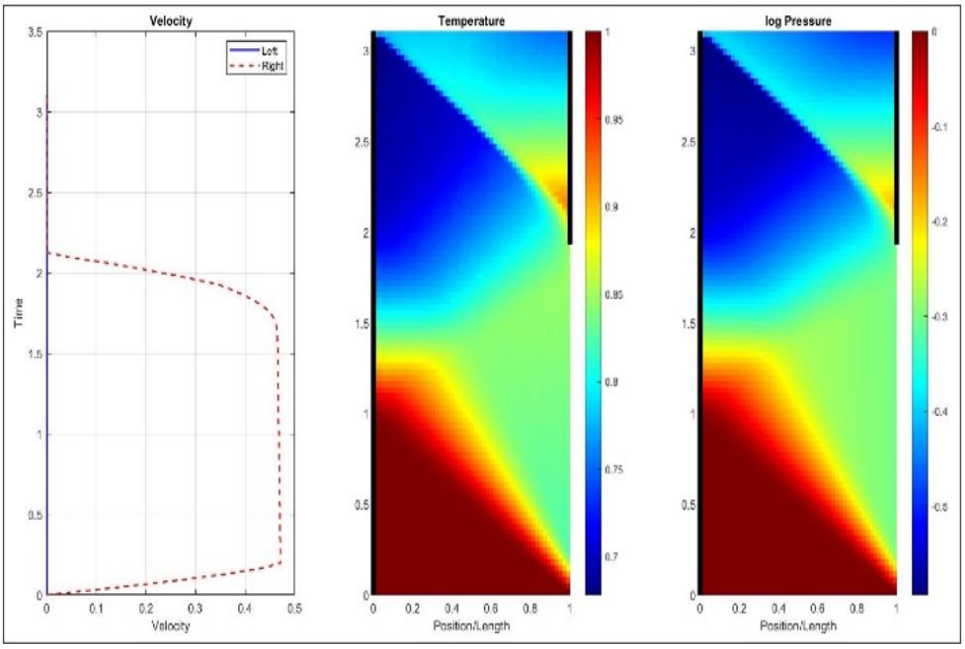

Figure 3.20. Velocity profile, Temperature and Pressure distribution during the duct emptying process with friction, computed by NASA Q1D program

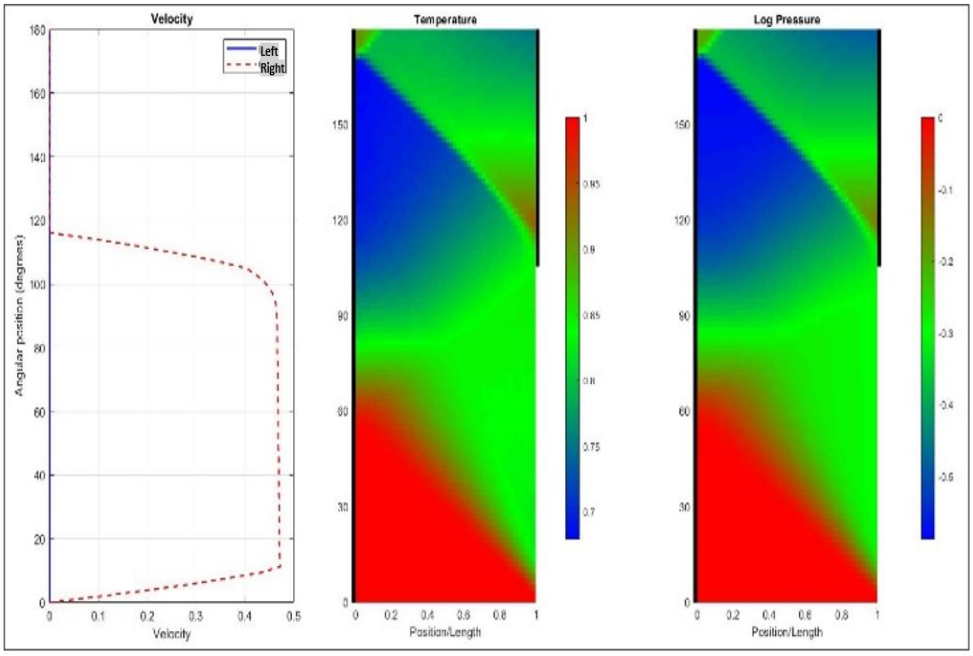

Figure 3.21. Velocity profile, Temperature and Pressure distribution during the duct emptying process with friction, computed by SCW1D program

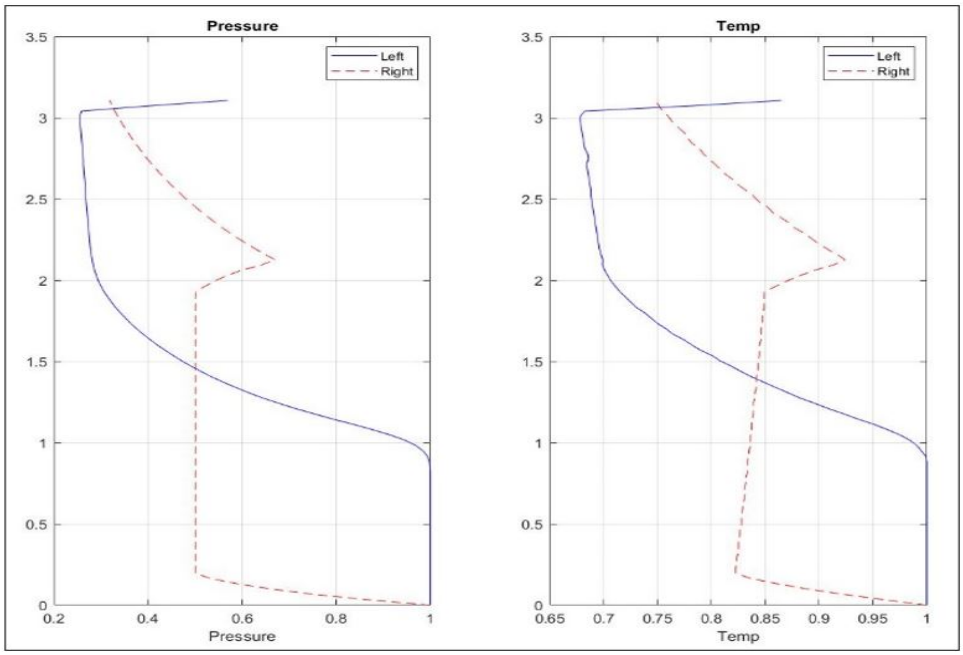

Figure 3.22. Pressure and Temperature variation during the duct emptying process with friction, computed by NASA Q1D program

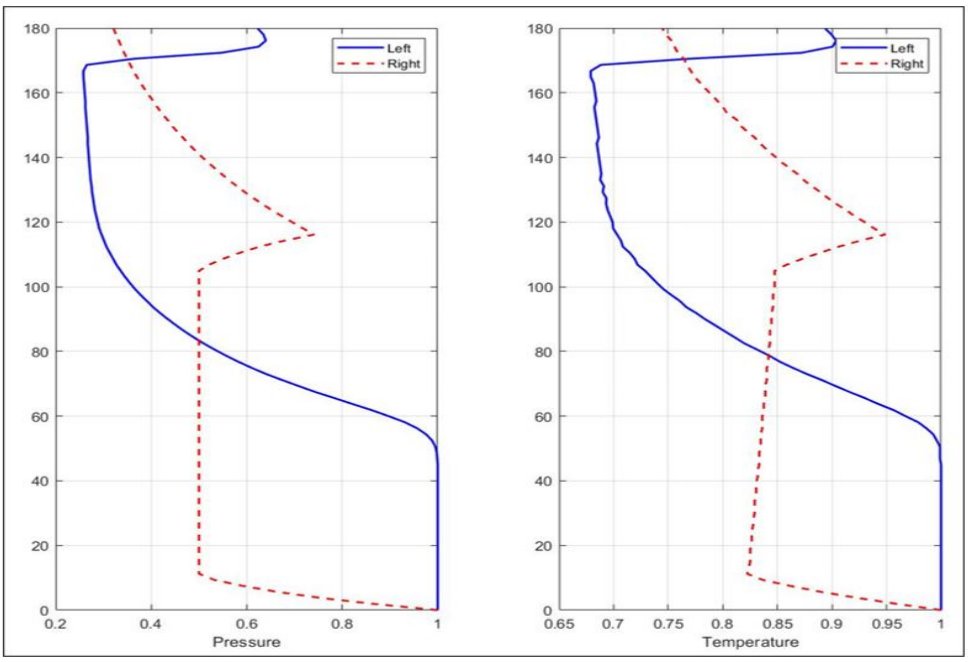

Figure 3.23. Pressure and Temperature variation during the duct emptying process with friction, computed by SCW1D program

3.3.3 Optimum Duct Emptying Process with Rotation

The approach to simulate the duct emptying process with rotation is similar to the duct filling process with rotation. The duct angle in case of the duct emptying process is shown in figure 3.24. The optimum duct angle is calculated in the same way as in the duct filling with rotation. The duct angle's significance has been discussed during the rotating duct filling case and remains equally important in the duct emptying case.

The optimum duct angle in this case,

$$tan(\beta) = \frac{\omega R}{u_{rel}}$$

For non-dimensional rotor radius 0.40327, angular speed 0.28704, and relative velocity predicted by the duct emptying simulations, the optimal duct angle is

$$\beta = 0.24093$$

Table 3.6. Velocity and Mass Flux results for duct emptying process with rotation

Parameters/Code	NASA Q1D	SCW1D	Analytical
MF	0.578	0.574	
Velocity	0.471	0.471	0.471

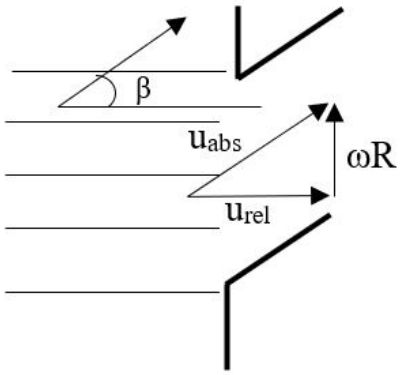

Figure 3.24. Mixed relative flow at the outlet port

Table 3.6 shows the velocity and mass flux results computed by the codes. Figures 3.25 and 3.26 show the pressure and temperature distribution during the process the optimum duct emptying with rotation.

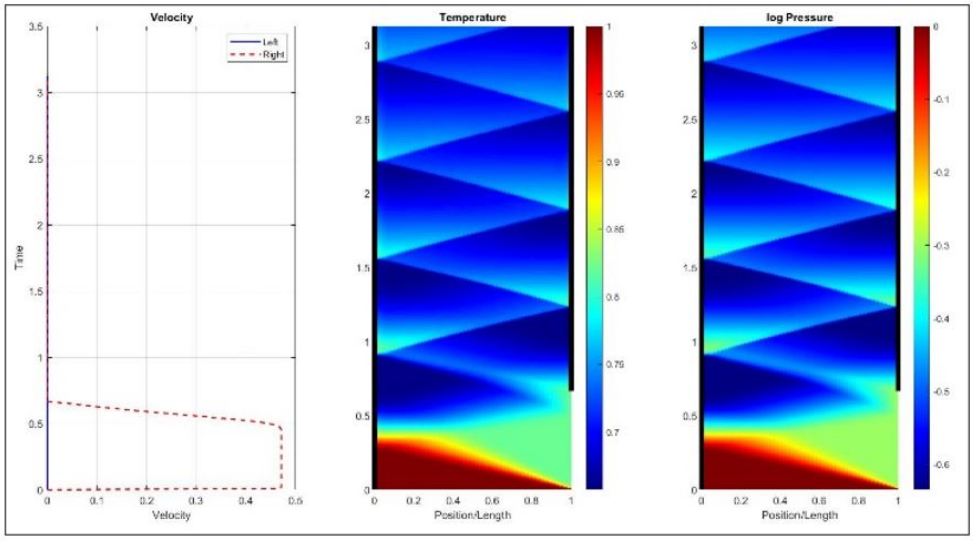

Figure 3.25. Velocity profile, Temperature and Pressure distribution during the duct emptying process with rotation, computed by NASA Q1D program

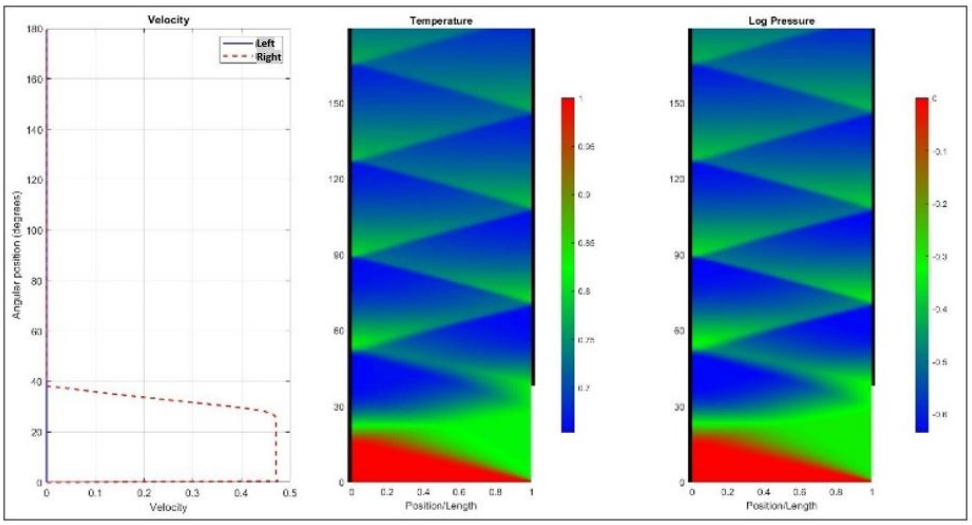

Figure 3.26. Velocity profile, Temperature and Pressure distribution during the duct emptying process with rotation, computed by SCW1D program

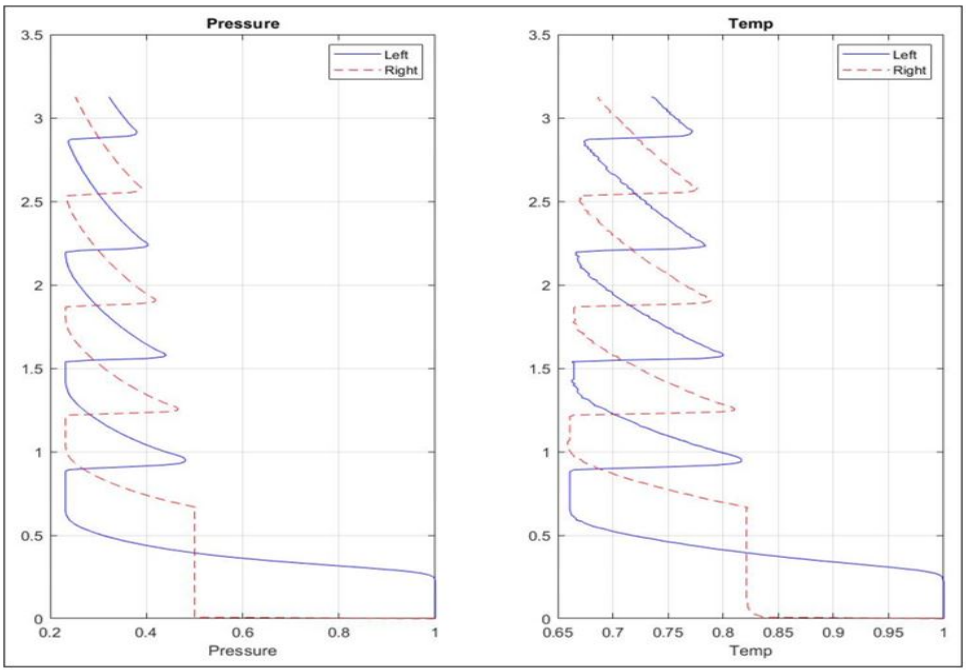

Figure 3.27. Pressure and Temperature variation during the duct emptying process with rotation, computed by NASA Q1D program

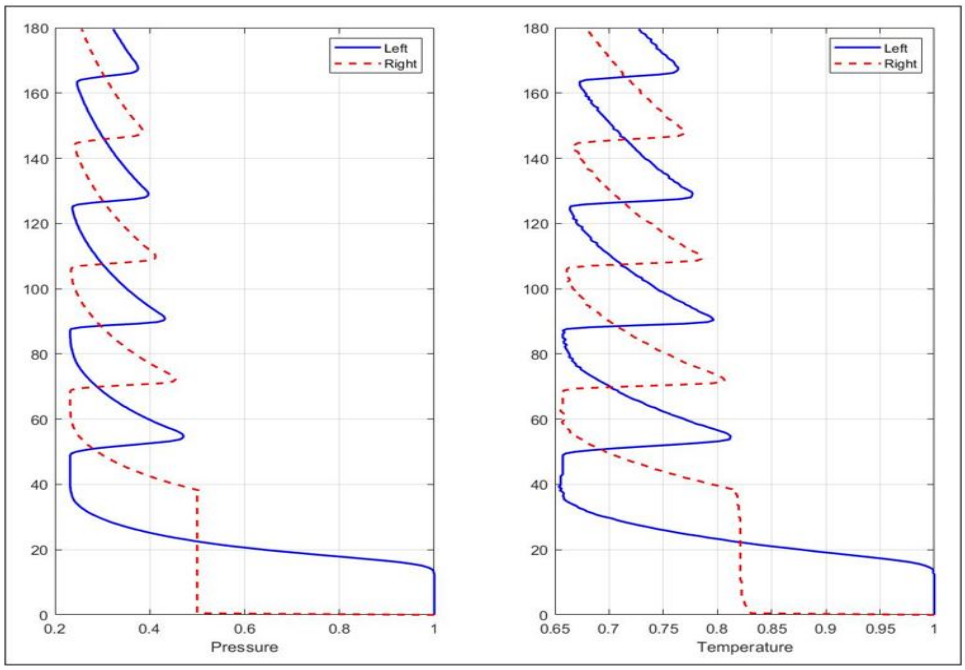

Figure 3.28. Pressure and Temperature variation during the duct emptying process with rotation, computed by SCW1D program

3.4 Discussion

The overall purpose of this study was to identify the parameters that influence the difference between the end results computed by three versions of the wave rotor analysis codes. Since all three codes utilize the same fundamental numerical method to integrate the governing equations, it is expected that the end results should be identical. Yet some complex phenomena simulated earlier had shown a slight variance between the mass flux and other results computed by NASA Q1D and SCW1D-B. It was observed that the SCW1D-B (curved-passage version of the SCW1D program) computes exactly the same results as the SCW1D-A (axial-passage version) when the passage curvature angle is set to zero. The comparison of the NASA Q1D program with SCW1D-A is given in section 4.4.2. The comparison between the SCW1D versions A and B can be seen in section 4.4.3.

As both NASA Q1D and SCW1D programs have gone through extensive modifications and changes earlier, it was also important to track those changes. Initially, the modeling approaches for different physical phenomena such as friction and heat transfer were examined.

Some minor discrepancies were detected in the friction modeling, which were due to incorrect input set up. Upon resolving, the codes were tested again for the end results. Though the margin of difference was decreased, the results were not precisely the same. Simulation results for the basic unsteady flow processes provide short insights about the parameters accountable for the difference between the end results estimated by the two codes.

The mixing calculations account for the losses incurred due to non-uniformities in the flow. These non-uniformities arise from various sources such as partial passage opening, inaccurate shock incidences, and broader expansion waves whose trailing edges reflect from the open ports and establish undesirable high-pressure zones. In the simulations with incorrect shock incidences, the flow emerging from the rotor must be turned by the port walls. The mixing and turning processes have been modeled separately in the codes. The difference between the actual duct angle and the mixed port flow angle, referred to as ALPH, has not been directly used in the mixing calculations, but it can be used as a comparison parameter. If the difference ALPH is smaller, the codes tend to be in good agreement. It is worth noting that, even at a large value of ALPH, the difference in mass ans energy flux values computed by two codes is not significant. Also, the non-dimensional velocity, total pressure, and total temperature values estimated by the codes are nearly the same.

The mixed port flow angle is calculated from the non-dimensional mixed relative velocity, as discussed in the duct filling with rotation case. Since the non-dimensional rotational speed, radius, and duct angle are constant, the parameter ALPH solely depends on the mixed relative velocity at the port. Hence, it can be inferred that the mixing calculations used in each program need to be closely examined against each other.

4. APPLICATION OF WAVE ROTOR ANALYSIS TOOLS FOR COMPREX PWS SIMULATION

Pressure wave supercharger is a four-port wave rotor configuration which can be integrated with an internal combustion engine for supercharging purposes. Comprex® is a tradename given to the PWS developed by Brown Boveri and Company for the supercharging of diesel engines. Although the notion of using a PWS for small diesel engines roots back to the early 1940s, its most successful application with commercial diesel engines pioneered in RF series diesel engines found in Mazda 626 or Capella models. After 1988, Mazda produced over 150,000 passenger cars with Comprex fitted diesel engines. In addition, Comprex was tested successfully by other manufacturers such as Mercedes-Benz, Opel, and Peugeot, with different sizing.

4.1 Operating Principle of Four-Port PWS

Comprex is a four-port, reverse-flow PWS with two operating cycles per revolution of the rotor drum. Two rows of 34 channels of irregular width are arranged around the Comprex rotor axis. The irregular width is deliberate and intended to reducing single-tone noise. Figure 4.1 shows the unwrapped view of the PWS rotor and port arrangements without pockets. The operating principle is illustrated using a simulation of the gas dynamics within the channels, neglecting the role of pockets for now.

For the simulations of PWS without pockets presented in this chapter, at the beginning of the cycle, the gas is assumed to be at medium pressure just before the scavenging and air intake processes. It is noted that in principle the cycle simulation can start at any point of time in the cycle. However, to avoid a partially open or closed channel at the start of end points, a different starting point will be found more convenient when pockets are included in later chapters. As the cycle starts, the channel end is exposed to the low-pressure outlet (EO) port. An expansion fan is generated from the trailing edge of the EO port because of the pressure differential between the channel insides and the rotor outsides. This expansion fan travels into the channel and causes discharging of the gas through the EO port. Upon reflecting on the cold-side wall, the reflected expansion waves tend to drop

the channel's pressure and temperature further. As the rotor continues to rotate, the low-pressure inlet (AI) port starts to open. Because of the pressure gradient created by earlier reflected expansion waves, fresh air is drawn into the channel. The EO port closes when the reflected expansion wave reaches the channel's right end. When the reflected expansion fan arrives at the outlet port, it eases back the outflow and reflects back as compression waves. These compression waves together with compression waves from the outlet closing form a solitary hammer shock wave that travels toward the AI port. The AI port closes when the hammer wave arrives at the trailing edge of the AO port. At this point, some fraction of the residual gas will be present with the trapped fresh air in the channel. The above sequence of processes describes the working of the low-pressure part of a PWS. The purpose of this process is to facilitate proper low-pressure scavenging and refill the channel with fresh air.

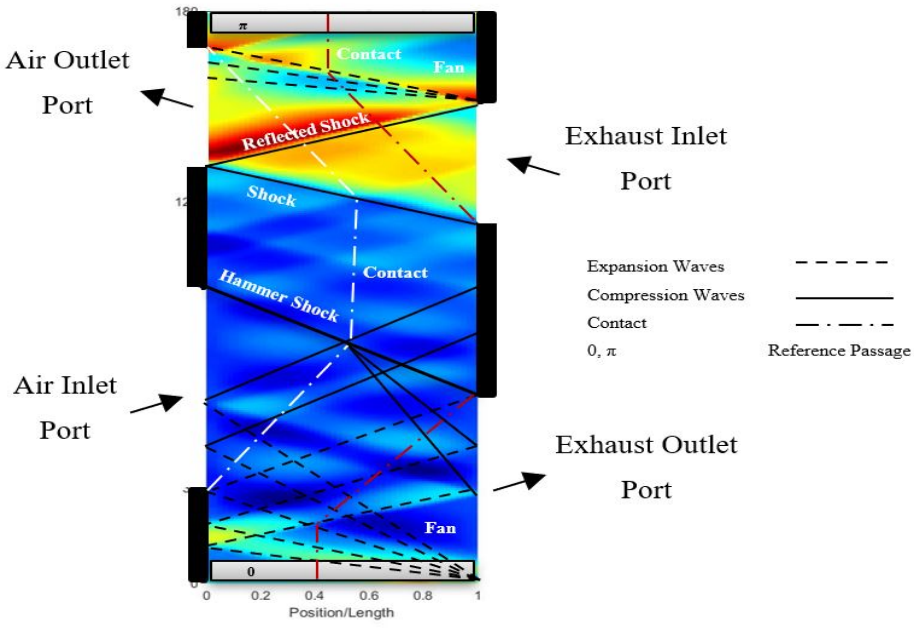

Figure 4.1. Wave Diagram for Comprex like PWS without pockets

In the high-pressure part of the cycle, the channel is first exposed to the high-pressure inlet (EI) port. The high-pressure and high-temperature exhaust gas coming from the engine penetrates into the channel, forming a strong compression wave originating from the leading edge of the EO port. As the compression wave moves towards the left wall, the previously present charge of fresh air will be compressed. As the high-pressure and high-temperature

exhaust gas come directly in contact with the fresh air charger, the energy is exchanged dynamically, increasing the pressure of the charge. The compression wave originated from the leading edge of the EI port must be incident on the leading edge of the high-pressure outlet (AO) port for optimum compression. If this compression wave reflects on the open AO port, the excessive exhaust gas will be recirculated to the engine, and undesirable backflows will occur. The compression wave reflects on the opening of AO port as a compression wave and twice compressed charge, comprising both air and exhaust gas, leaves the channel through the AO port. The closure of EO port should be designed to match the time when the reflected shock arises at the right end of the channel. An expansion fan initiates from the EI port's trailing edge and travels into the channel, causing the channel flow to slow down. The AO port closes when the expansion fan reaches the left end of the channel. At this moment, the channel flow comes to the rest, and the gas state inside the channel is similar to the gas state at the beginning of the cycle.

It should be noted that the objective of this subchapter is to explain the flow field in Comprex by considering it as a four-port PWS. The effects of wall-pockets have been excluded so that the their benefit can be evaluated relative to this simpler case as a baseline. The functioning and effects of the wall-pockets will be discussed in detail in the next chapter.

4.2 Boundary Conditions

The governing equations for the unsteady flow field inside the wave rotor channels have been discussed in Chapter 2. The codes integrate the governing equations numerically to estimate the properties inside the channels and at the ports. Proper geometrical inputs are required to be given to the code in order to simulate different wave rotor configurations. The codes accept the geometrical input parameters in non-dimensional form where the length is scaled by the passage length.

The measurements were taken on the Comprex CX-93 unit available at the Combustion and Propulsion Research Laboratory (CPRL) at IUPUI, which had been provided by CPRL to the Air Force Institute of Technology in a collaboration for experimental evaluation by AFIT. Additionally, certain assumptions were made for computational simplicity. The gap between the rotor and the end wall is assumed to be 0.0025' on each end. This value was

taken from the difference between the rotor length and the shroud length. Comprex has two rows of 34 varying width passages arranged around the rotor axis. Two rows of passages and variable width are difficult to model in the one-dimensional analysis. Hence, the passage arrangement is assumed to be of single row and uniform width, similar to that in the NASA four-port wave rotor experiment. The passage width was obtained by dividing the length of two cycles (As the Comprex completes two cycles in one revolution) by the number of channels. The passage height is calculated from the difference between the outer diameter and the inner diameter of the rotor. All of these parameters were non-dimensionalized by the passage length. The port opening and closing locations, as well as the pocket angular width, were measured in radians.

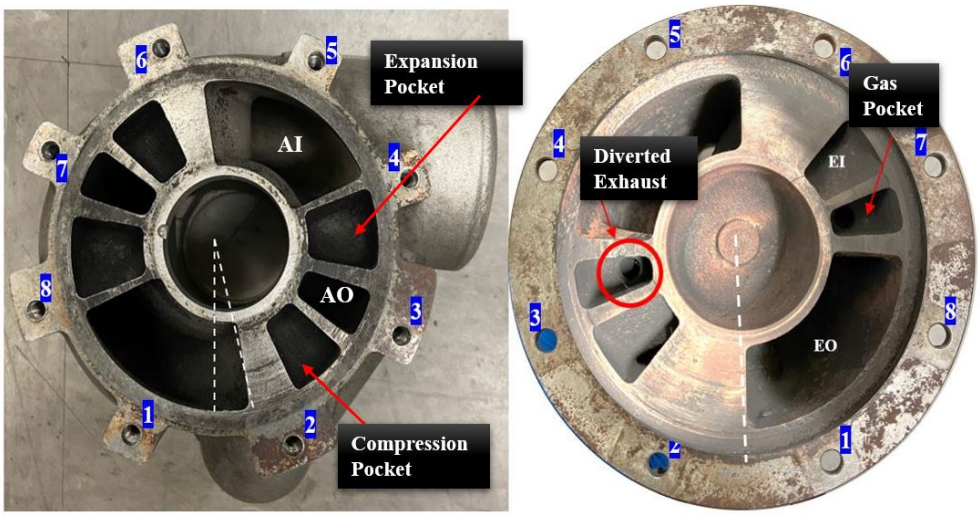

Figure 4.2. Matching bolt locations to decide relative positions of the ports. (Left- Cold stator plate, Right- Hot stator plate)

The relative positions of the ports need to be measured accurately in order to decide the design speed. To measure the relative positions of the ports, the cold stator plate was bolted to the hot stator plate and horizontal position the cold stator plate was determined. It can be observed in figure 4.2 that the trailing edge of the EO port is perpendicular to the horizontal datum. The angle in radians between the AI port trailing edge and the EO port trailing edge was measured to determine the relative positioning of the two manifolds. The duct angles are used in the application of boundary conditions, incidence loss modeling, and were also measured as accurately as possible.

The codes require absolute stagnation pressure and temperatures (in duct frame of reference) at the inflow ports and static pressures at the outflow ports. The temperatures are not used at the outflow ports, unless there is back flow. The pressure and temperature boundary conditions were chosen from the experimental work conducted by B. Smith [32] at the Air Force Institute of Technology, using exactly the same CX-93 unit that was measured. It is the only experimental study conducted on Comprex with measurements of flow rates of each port, known to the author to be published. The experimental testing method involved the mass flow rate input to the EI port, and corresponding pressure and temperature conditions were measured at each port. The test points selected by Smith were 9,420 RPM and 12,960 RPM with 13.1 lbm/min, and 12,000 RPM with 15 lbm/min. These test points were then simulated using the NASA Q1D code. The mass flow through the EO port was adjusted by varying the simulated exhaust outlet valve area such that the mass flow rate through the AI port matches the experimental value. The code requires static pressure as a boundary condition at the outflow ports, which was difficult to estimate during the experiment. The static pressure values imposed at the AO port were adjusted to obtain the computed EI to AI mass flow rate ratio matches the experimental EI to AI mass flow rate ratio.

This chapter aims to simulate the Comprex cycle without making any adjustments to the mass flow rates to match the experimental conditions. The simulation emphasizes the computational analysis of the Comprex performance, more than just emulating the experimental approaches. However, the boundary conditions have been chosen to imitate the working of Comprex under realistic conditions. The engine calculations performed by Smith [32] explain the mass flow rate requirements for the 2.0 l Mazda RF series engine. Table 4.1 shows the engine specifications. The exhaust mass flow rates to the EI port at different speeds are listed in table 4.2.

The experimental testing also gives insights about the pressures and temperatures at each port. The principal interest here is to investigate the Comprex performance. Hence the additional modules such as combuster and valve have not been used. The channel is divided into 50 axially uniform computational cells, and the convergence check for grid spacing has been presented in Appendix A.

Table 4.1. MAZDA Engine Specifications

Mazda 626 IV GE	
Engine	2.0 D GLX Comprex
Fuel	Diesel
Fuel Consumption	34.59 US mpg
Power	75 HP @ 4,000 RPM
Power per ltr	37.5 HP/ltr
Torque	179 N-m @ 2000 RPM
Displacement	1998 cc / 121.93 in3
No. of Cylinders	4-inline
Cylinder Bore	86 mm
Piston Stroke	86 mm
Compression Ratio	21:1

Table 4.2. Volumetric and mass flow rates for different engine speeds in Mazda 626 2.0 D engine, from ref. [32]

Engine Speed (RPM)	Volumetric Flow Rate (ft^3/min)	Mass Flow Rate (lb/min)
1,000	70.63	5.30
1,500	105.95	7.95
2,000	141.26	10.59
2,500	176.58	13.11
3,000	211.89	15.89
3,500	247.21	18.54
4,000	282.52	21.19
4,500	317.84	23.84

4.3 Comprex Simulation and Results

The measurements taken on the Comprex unit have provided the input parameters required by the codes. An unknown version of the NASA Q1D program has been previously utilized to model flow for the Comprex PWS by Smith [32] and Metaczynski [35]. The SCW1D-A and SCW1D-B programs have not been validated for this type and size of wave rotors. The numerical simulations performed using the SCW1D programs have served as an attempt to validate the SCW1D programs for the wave rotors with Comprex like design elements.

The run conditions are chosen from the experimental work described in the previous subchapter. The simulation results for the Comprex test case at 12,960 RPM have been explained in this subchapter.

The absolute stagnation pressure and temperature at the AI port are 14.7 psi and 518 R, respectively. These values have been used as the reference conditions throughout this chapter. The mass flow rate through the EI port at this speed was 13.1 lbm/min, with the total pressure and temperature equal to 24.9 psi and 859.8 R, respectively. The total pressure and temperature at the AO port were measured to be equal to 22.64 psi and 673.4 R, respectively.

4.3.1 Comprex Simulation without pockets using NASA Q1D

Table 4.3 shows the comparison between the experimentally measured and the computationally predicted mass flow rates, non-dimensional total pressures ($\boldsymbol{\pi}$), and total temperatures (τ). The mass flow rate values are in lbm/min. It is noted that mass inflow at EI is substantially greater than mass outflow in AO in the experiment and in the simulation for the same boundary conditions. This will not be the case in a real diesel engine operating condition, even accounting for fuel flow.

Table 4.3. Comparison of experimental and computational results for Comprex test at 12,960 RPM rotor speed (NASA Q1D)

	Experimental				Computational			
	AI	AO	EI	EO	AI	AO	EI	EO
$\dot{m}$	10.05	11.07	13.04	12.02	8.01	10.97	12.02	8.97
$\boldsymbol{\pi}$	1.00	1.47	1.78	1.02	1.01	1.57	1.62	1.02
τ	1.06	1.27	1.66	1.46	1.05	1.32	1.64	1.46

Table 4.4. Difference between experimental and computational results (NASA Q1D)

	AI	AO	EI	EO
$\dot{m}$	20%	0.9 %	8 %	25 %
$\boldsymbol{\pi}$	1%	6%	9%	0%
τ	0.94%	4%	1.21%	0%

As shown in Table 4.4, the basic NASA Q1D code can predict the mass flow rates with an average difference of 13% and a maximum difference of 25%. The pressure ratios are predicted with a maximum difference of 9% and an average difference of 4.20%. The temperature ratios are predicted with a maximum difference of 4% and an average difference of 1.52%. The overall results and the differences between the experimental and computational values will be elaborated in subchapter 4.4.

Figures 4.3 and 4.4 show the series of x-t diagrams of the Comprex cycle at 12,960 RPM simulated using the NASA Q1D program. The temperature diagram clearly shows the interface between the fresh air and the exhaust gases. In the figures, the AI port is located at the bottom on the left side. The top port on the left side is the AO port. On the right side, at the bottom, is the EO port, whereas at the top is the EI port. Unless otherwise stated, the port convention will be the same throughout this chapter.

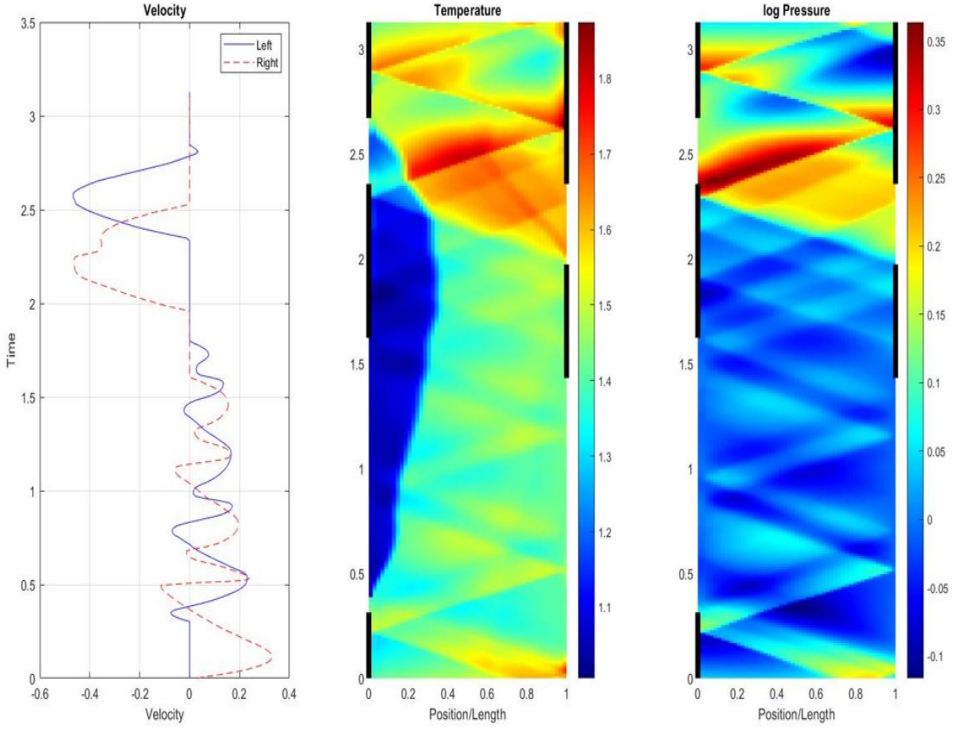

Figure 4.3. Comprex simulation at 12,960 RPM rotor speed (NASA Q1D)

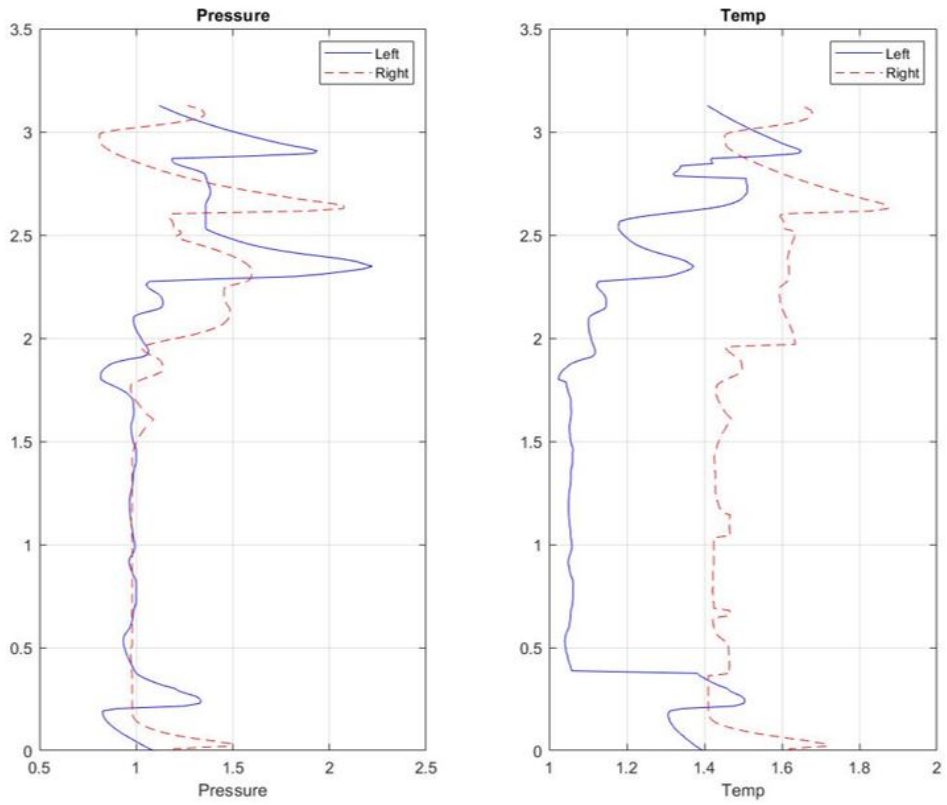

Figure 4.4. Temperature and Pressure variation during the Comprex cycle at 12,960 RPM rotor speed (NASA Q1D)

4.3.2 Comprex Simulation without pockets using SCW1D

The results produced by the SCW1D-A and the SCW1D-B programs are identical when the passage curvature angle is set to zero (in SCW1D-B). Hence the results included in this chapter are conducted using the SCW1D-A version. However, the results have been verified using the two versions, and they represent both of the versions. Table 4.5 shows the comparison between the experimentally measured and the computationally predicted mass flow rates, non-dimensional total pressure (π) and total temperature (τ). The mass flow rate values are in lbm/s.

As shown in Table 4.6, the SCW1D code can predict the mass flow rates with an average difference of 14% and a maximum difference of 25%. The pressure ratios are predicted with a maximum difference of 9% and an average difference of 4.73%. The temperature ratios

Table 4.5. Comparison of experimental and computational results for Comprex test at 12,960 RPM rotor speed (SCW1D)

	Experimental				Computational			
	AI	AO	EI	EO	AI	AO	EI	EO
$\dot{m}$	10.05	11.07	13.04	12.02	7.95	12.13	13.3	9.06
π	1.00	1.47	1.78	1.02	1.03	1.61	1.70	1.04
τ	1.06	1.27	1.66	1.46	1.05	1.36	1.65	1.48

Table 4.6. Difference between experimental and computational results (SCW1D)

	AI	AO	EI	EO
$\dot{m}$	21%	10%	2%	25%
π	3%	9%	4%	2%
τ	0.94%	7%	0.6%	1%

are predicted with a maximum difference of 7% and an average difference of 2.5%. A severe difference can also be observed even at the inflow port, where stagnation properties are correctly used as per experimental measurements. One of the possible reasons behind this is the off-design rotor speed which is conducive to undesirable flow reversals in the low-pressure ports. The overall results and the difference between the computational and experimental values will be discussed in the subsequent chapter. Figures 4.5 and 4.6 show the series of x-t diagrams of the Comprex cycle at 12,960 RPM, produced by the SCW1D program.

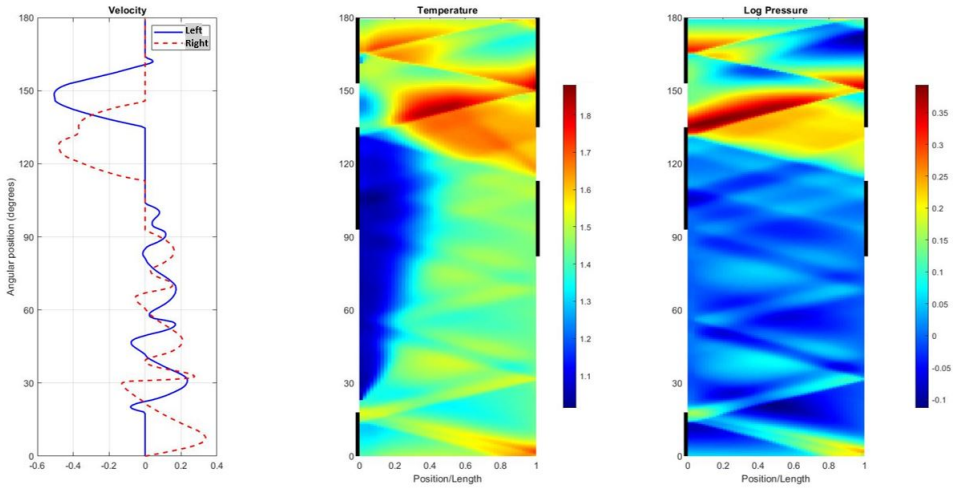

Figure 4.5. Comprex simulation at 12,960 RPM rotor speed (SCW1D)

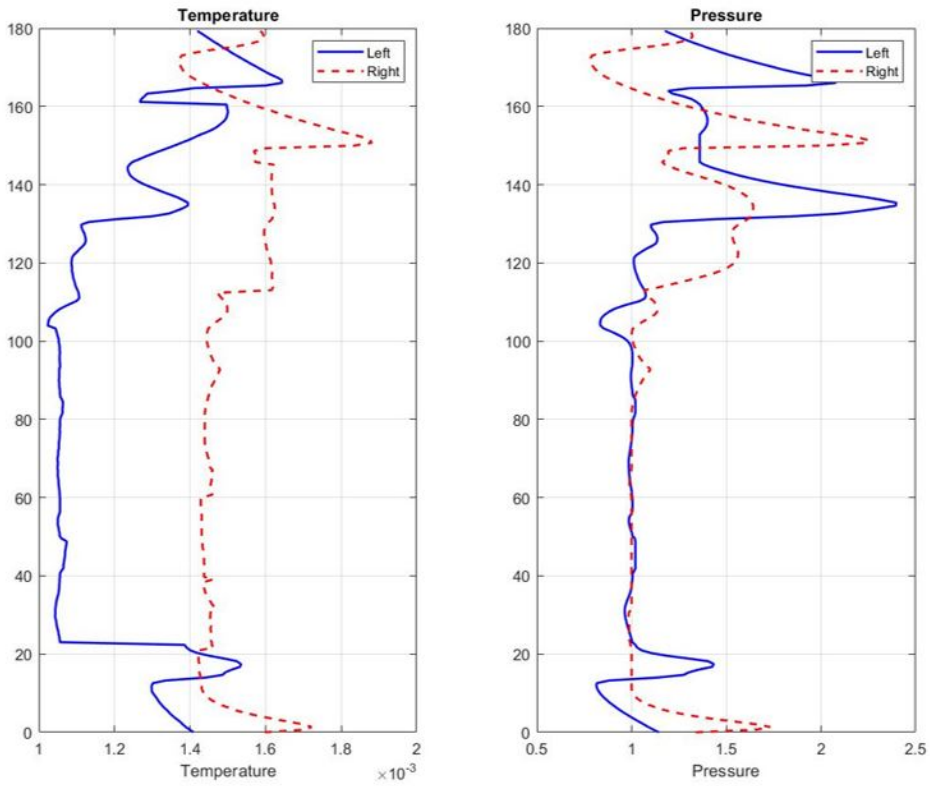

Figure 4.6. Temperature and Pressure variation during the Comprex cycle at 12,960 RPM rotor speed (SCW1D)

4.4 Discussion

Figures 4.3 to 4.6 represent a Comprex cycle simulated from the low-pressure part to the high-pressure part. This approach is conventionally used in computational simulations of the wave rotors. The right side represents the hot side of the Comprex, whereas the left side represents the cold side. The port arrangements are as explained in figure 4.1.

4.4.1 Comparison between Experimental and Computational Results

It should be noted that the test case selected by Smith [32] in the experimental testing does not emulate the actual operating condition of a Comprex. Also, the speed chosen, i.e., 12,960 RPM, is not the design point speed of the Comprex. Hence by looking into the

velocity diagram, some backflows can be observed in certain areas. The backflows occur as a result of incorrect shock incidences due to far off-design operation of the Comprex.

The computational tools require the static values at the outflows. But only total pressure and temperature values were recorded during the experiment. Higher pressure values at the outflow ports adversely affect the mass flux through the port. Hence the mass flow rates at the outflow ports, computed by the codes, are considerably lower. The pressure variation during the cycle indicates that the fresh air attains the maximum pressure just before the AO port opens. It can be observed that at this rotational speed and boundary conditions, the compression wave originated from the leading edge of the EI port is unable to strike the leading edge of the AO port. The reflected wave then reciprocates in the channel as a compression wave. As the channel is exposed to the EO port, the strong compression wave reflects on the open port and forms a broader expansion wave.

Significantly, the trailing edges of broader expansion waves reflect on the open ports and establish high-pressure zones at undesirable locations. This phenomenon is conducive to backflows and restricts the low-pressure scavenging process. As a result, sufficient pressure depression is not obtained when the channels are exposed to the AI port, and the inflow through the AI port falls off. CFD results normally overpredict the scenarios, and the more considerable difference can be seen in the mass flow rates through AI and EO ports.

4.4.2 Comparison between NASA Q1D and SCW1D-A

Though there is a small difference between the results produced by the two codes, the solution marching is identical. Hence the velocity profile, pressure, and temperature variations are precisely similar in every respect. Figure 4.7 shows the comparison between the velocity profiles predicted by the two codes. It is evident that the programs can compute the Comprex characteristics precisely and the two programs work in the same way.

Comparison between the results predicted by the two codes can be seen in Table 4.7. The differences between the results have been listed in Table 4.8.

As shown in Table 4.8, the maximum difference between the mass flow rates predicted by the codes is 9%. The more severe difference can be observed in the high-pressure part of the cycle. It is likely to result from the methods used to update the port pressure and

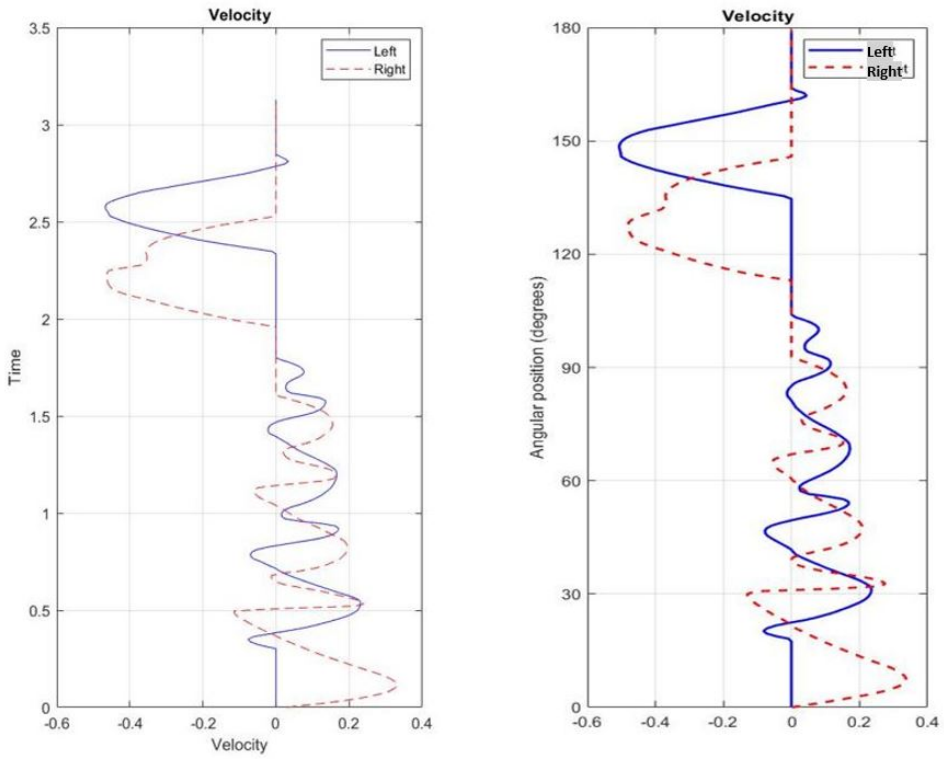

Figure 4.7. Velocity profile computed by NASA Q1D (on left) and SCW1D (on right)

Table 4.7. Comparison between the results predicted by NASA Q1D and SCW1D

	NASA Q1D				SCW1D			
	AI	AO	EI	EO	AI	AO	EI	EO
$\dot{m}$	8.01	10.97	12.02	8.97	7.95	12.13	13.3	9.06
π	1.01	1.57	1.62	1.02	1.03	1.61	1.70	1.04
τ	1.05	1.32	1.64	1.46	1.05	1.36	1.65	1.48

Table 4.8. Difference between the results predicted by NASA Q1D and SCW1D

	AI	AO	EI	EO
$\dot{m}$	0.75%	9%	9%	0.99%
π	0.98%	2%	4%	2%
τ	0%	3%	0.6%	1%

temperatures after performing the mixing calculations. Another possible reason is the data types used in the mixing calculations and other subroutines. The SCW1D programs have been through extensive organizational and optimizing changes. All of the subroutines have

been organized to accommodate good programming practices. But only a few modifications have been performed on the NASA Q1D program. The real numbers calculated by the code have been used at most places in NASA Q1D, such as in conditional statements for comparisons. Although the effect of this approach seems trivial locally, it can introduce considerable errors in the end results.

In this chapter, the simulation of Comprex has been performed by considering it as a four-port wave rotor. But Comprex is a quite complicated device, with some unique design elements. It is provided with wall-pockets to facilitate the low-pressure exhaust without affecting the other inflows or outflows. The subsequent chapter will elaborate on the pocket combination modeling and simulations.

4.4.3 Comparison between SCW1D-A and SCW1D-B

The SCW1D-B program, as described in the introduction, is an extension of the SCW1D-A program and is used for non-axial (bent, slanted or curved) channel wave rotor or wave turbine analysis. The SCW1D-B program has also been used to simulate the same test case discussed above. It was noted earlier that the SCW1D-B program predicts the results exactly in the same fashion as the SCW1D-A, when the passage slant angle and curvature are set to zero. It is because the conservation equations to account for the passage curvature have been manipulated algebraically such that the additional terms from the passage curvature are transferred to the source vector, which should in principle become zero for axial passages. The version A and B of the SCW1D program basically use the same numerical scheme. However, there implementation of some flow loss mechanisms, particularly flow incidence has not been verified to be equivalent.

Figures 4.8 and 4.9 show the results computed using the SCW1D-B code with same boundary conditions and duct angles. A different color scheme has been used to indicate the results for distinguishing purposes. However, closely observing, there is no difference between the results computed by the SCW1D-B and the SCW1D-A.

Table 4.9 shows the comparison between the mass flow rates, pressure, and temperature ratios predicted by the two versions of the SCW1D program. As can be seen in the table 4.9, the results computed by the two codes are identical when the passage curvature angle

is set to zero in version B. As the duct angle provided may result in some flow incidence during the process of inflows, it appears that the SCW1D-B code computes flow incidence as well as other loss processes very similarly to SCW1D-A.

Table 4.9. Comparison between the results predicted by SCW1D-A and SCW1D-B

	SCW1D-A				SCW1D-B			
	AI	AO	EI	EO	AI	AO	EI	EO
$\dot{m}$	7.95	12.13	13.3	9.06	7.95	12.13	13.3	9.066
π	1.03	1.61	1.70	1.04	1.03	1.61	1.70	1.04
τ	1.05	1.36	1.65	1.48	1.05	1.36	1.65	1.48

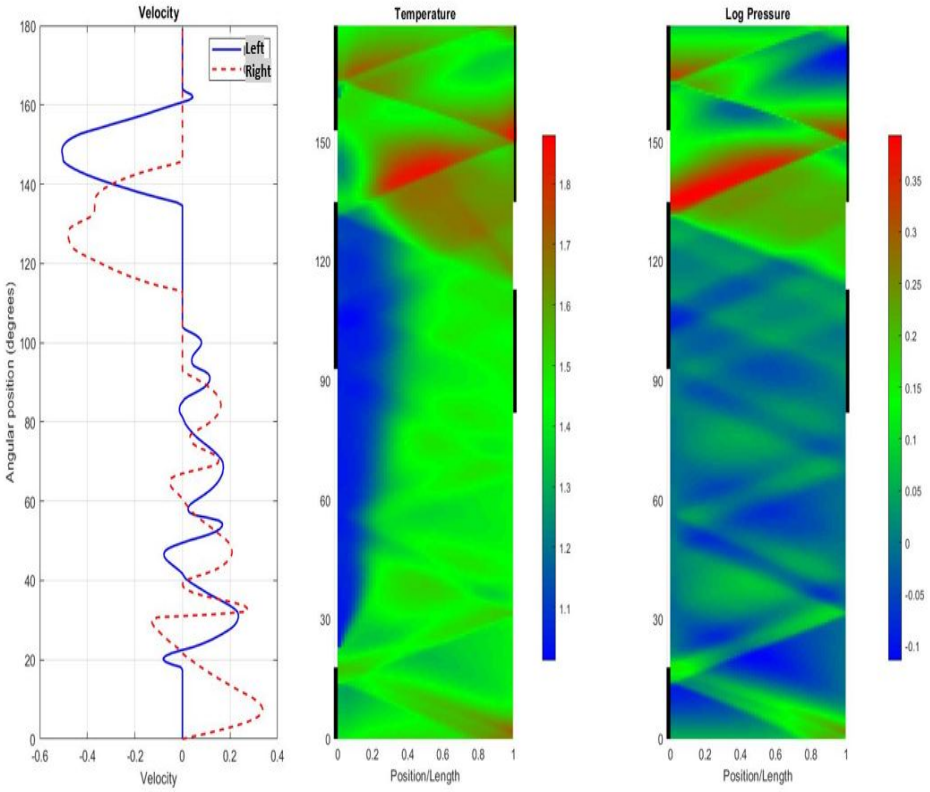

Figure 4.8. Comprex Simulation at 12,960 RPM (SCW1D-B)

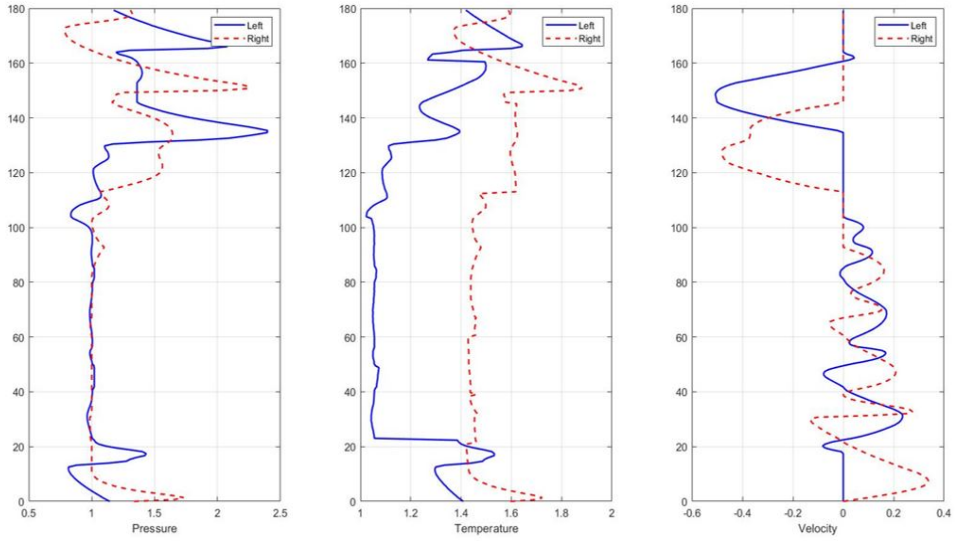

Figure 4.9. Temperature and Pressure variation during the Comprex cycle at 12,960 RPM rotor speed (SCW1D-B)

4.5 Additional Comprex Simulation Test

As stated earlier, the SCW1D programs have not been validated for the Comprex type PWS geometries. This work serves to validate the SCW1D programs for the size, geometry, and design of Comprex. In order to assess the performance of the codes, another test point from the experimental work described in ref. [32] was selected.

The experimental data is available for the Comprex simulation at 12,000 RPM with 15.9 lbm/min mass flow rate provided to the EI port. The pressure and temperature boundary conditions are selected in the same way, as described in section 4.3. The codes seem to be in good agreement with the experimental results.

4.5.1 Comprex Simulation at 12,000 RPM with NASA Q1D

Table 4.10 shows the experimentally measured and computationally predicted mass flow rates, pressure and temperature ratios. Table 4.11 points out the difference between experimental and computational values.

As shown in Table 4.11, the NASA Q1D code can predict the mass flow rates with an average difference of 10% and a maximum difference of 15%. The pressure ratios are predicted

Table 4.10. Comparison of experimental and computational results for Comprex test at 12,000 RPM rotor speed (NASA Q1D)

	Experimental				Computational			
	AI	AO	EI	EO	AI	AO	EI	EO
$\dot{m}$	10.03	12.59	15.87	13.31	11.01	13.01	13.51	11.29
$\boldsymbol{\pi}$	1.00	1.54	1.98	1.02	1.02	1.65	1.77	1.06
τ	1.07	1.34	1.63	1.42	1.05	1.31	1.61	1.40

Table 4.11. Difference between the experimental and computational results (NASA Q1D)

	AI	AO	EI	EO
$\dot{m}$	9 %	3 %	14 %	15 %
$\boldsymbol{\pi}$	2 %	7.14 %	10 %	4 %
τ	1 %	2 %	1 %	1 %

with a maximum difference of 10% and an average difference of 7%. The temperature ratios are predicted with a maximum difference of 2% and an average difference of 1%. Figures 4.10 and 4.11 show the pressure and temperature distribution and velocity profile during the cycle at 12,000 RPM.

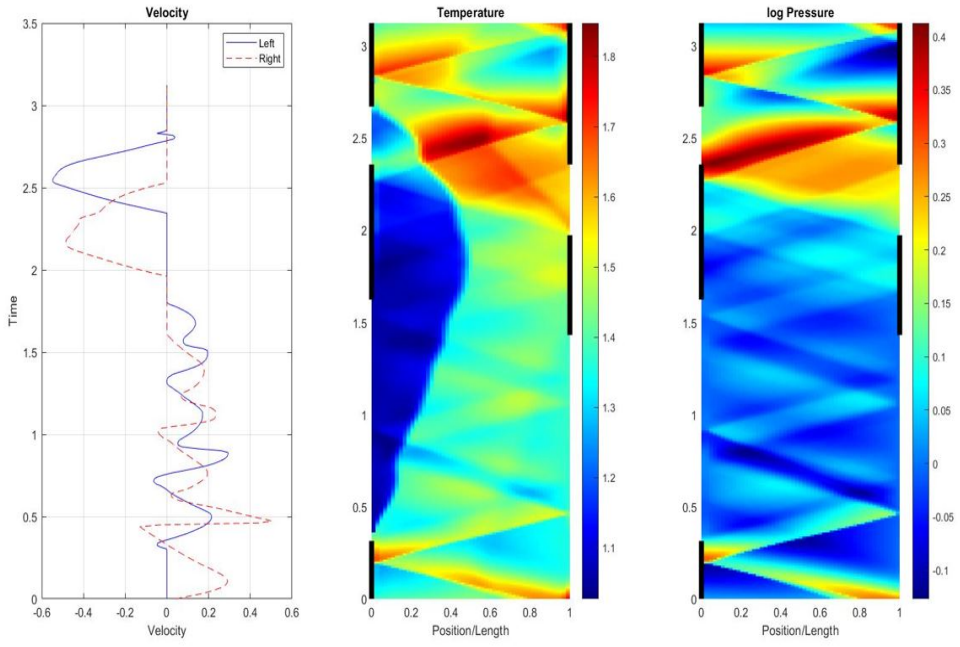

Figure 4.10. Comprex simulation at 12,000 RPM (NASA Q1D)

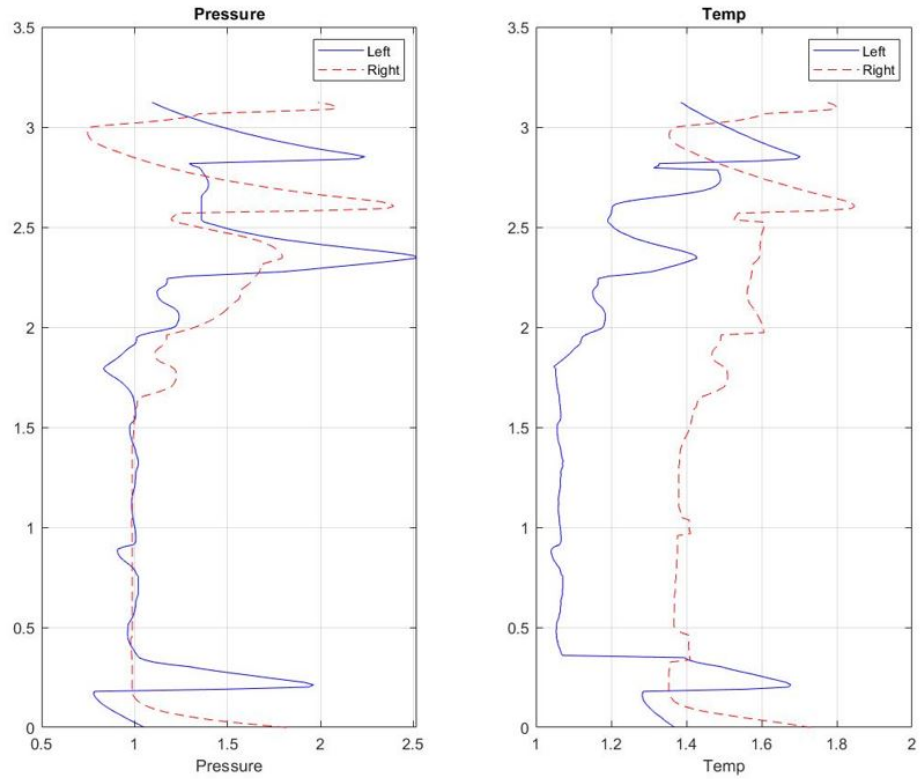

Figure 4.11. Temperature and Pressure variation during the Comprex cycle at 12,000 RPM rotor speed (NASA Q1D)

4.5.2 Comprex Simulation at 12,000 RPM with SCW1D (A and B)

Table 4.12 shows the experimentally measured and computationally predicted mass flow rates, pressure and temperature ratios. Table 4.13 points out the difference between experimental and computational values.

Table 4.12. Comparison of experimental and computational results for Comprex test at 12,000 RPM rotor speed (SCW1D)

	Experimental				Computational			
	AI	AO	EI	EO	AI	AO	EI	EO
$\dot{m}$	10.03	12.59	15.87	13.31	10.38	14.23	15.35	11.24
$\boldsymbol{\pi}$	1.00	1.54	1.98	1.02	1.02	1.70	1.87	1.04
τ	1.07	1.34	1.63	1.42	1.06	1.37	1.62	1.42

Table 4.13. Difference between the experimental and computational results (SCW1D)

	AI	AO	EI	EO
$\dot{m}$	3 %	13 %	3 %	15 %
$\boldsymbol{\pi}$	2 %	10 %	5 %	2 %
τ	0.93 %	2 %	0.61 %	0 %

As shown in Table 4.13, the SCW1D code can predict the mass flow rates with an average difference of 9% and a maximum difference of 16%. The pressure ratios are predicted with a maximum difference of 10% and an average difference of 5%. The temperature ratios are predicted with a maximum difference of 2% and an average difference of 1%. Figures 4.12 and 4.13 show the variation of properties during the cycle.

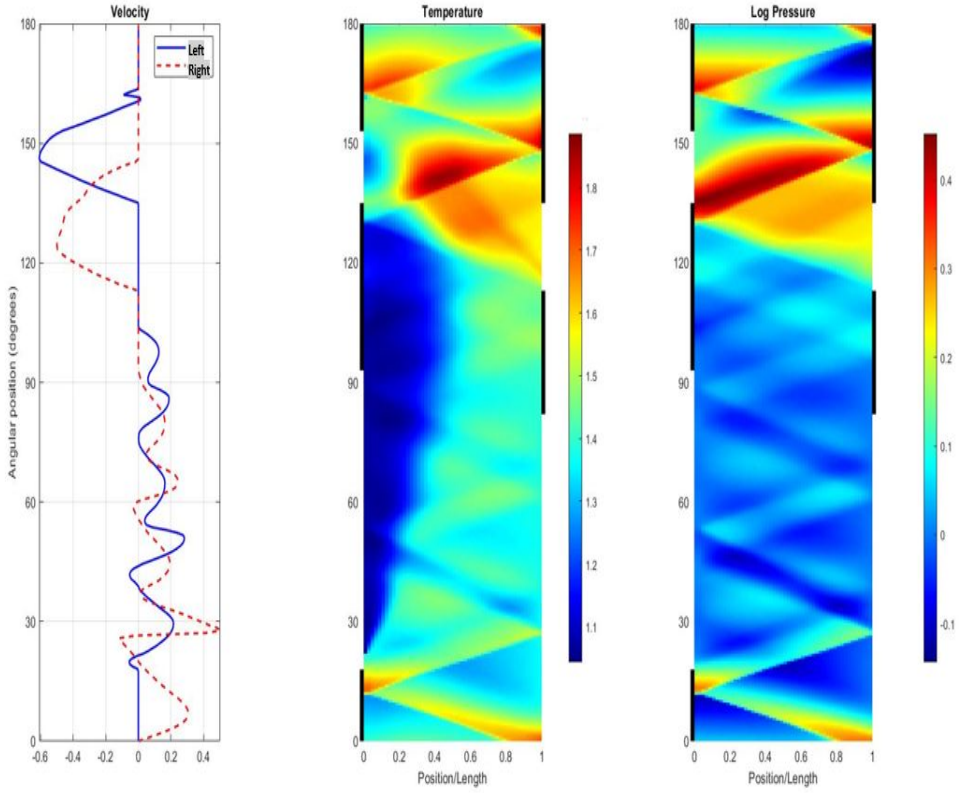

Figure 4.12. Comprex simulation at 12,000 RPM (SCW1D)

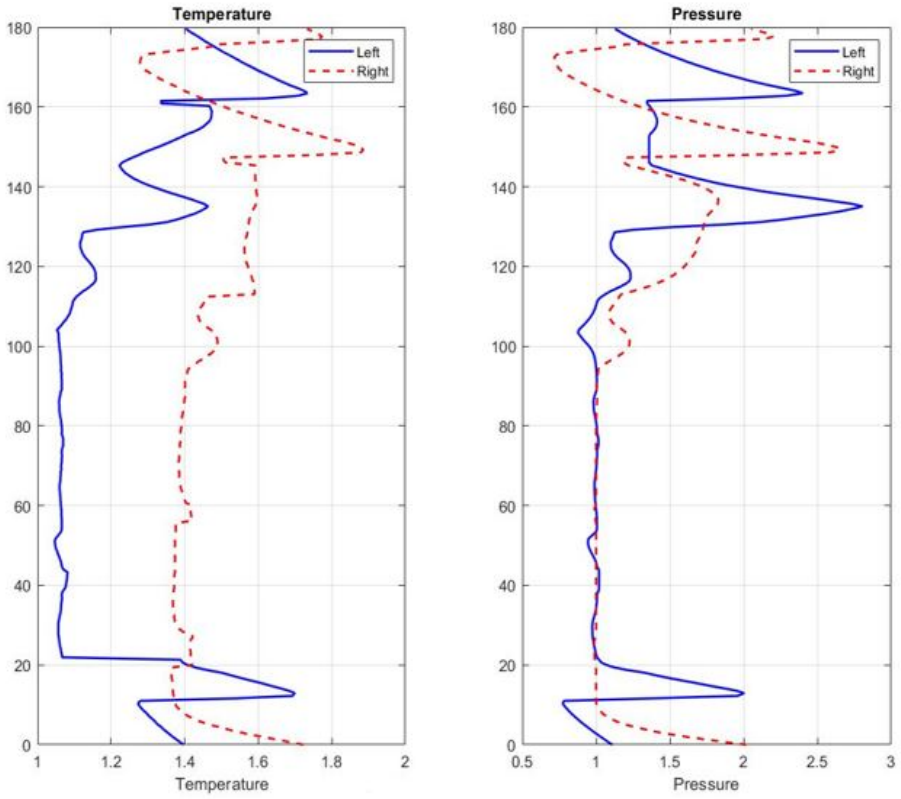

Figure 4.13. Temperature and Pressure variation during the Comprex cycle at 12,000 RPM rotor speed (SCW1D)

5. VARIABLE SPEED TEST ON COMPREX

5.1 Effect of Variable Speed and Load Conditions

The importance of correct wave timings and the influence of rotor speed on the performance of a PWS have been discussed in Chapter 4. Comprex is a belt-driven PWS, and the rotor speed is proportional to the engine speed, which may not be optimal for PWS operation. At the design point, a PWS is theoretically a very efficient device. A PWS needs to be specifically designed to meet some specific requirements (such as compression ratio and efficiency) of the unit to be supercharged. Under the variable speed and load conditions of the engine, it is difficult to meet these requirements.

The PWS has been successfully tested on passenger car engines as well as heavy-duty vehicles. The main advantage of the PWS is its rapid response to engine demand [1]. The design features of the Comprex have enabled the device to keep operating under variable load and speed conditions without failure. But a simple four-port wave rotor has limitations to work under off-design conditions. If the rotor speed of a PWS goes below the design point, the air will be compressed before the AO port opening, and for a pocketless PWS the reflected wave traveling back into the channel will restrict the EI flow. Further reflections of the wave on open ports give rise to the low-pressure zone between the high-pressure and low-pressure parts of the PWS. Under such a scenario, the PWS operation will collapse due to the low efficiency and excessive exhaust gas recirculation. To overcome the shortcomings arising due to the reduced speed, an engine-dependent means can be used to maintain the rotor speed constant. But it does not solve the whole problem.

Engine load is a crucial factor affecting the performance of superchargers. Under on-road operating conditions, the engine load fluctuates frequently. If the engine load exceeds the drive torque, the engine speed decreases. Also, on numerous occasions, the engine load tends to exceed the rated load. In such a situation, the engine speed falls below the rated speed, decreasing the ability to produce power. The engine needs heightened air and fuel flow to overcome the power deficit under increased load conditions. This is a challenging situation that a PWS should be able to address. The mass flow rate through the AO port is required to be adjusted according to the engine demand. Also, it should be noted that wave speeds

will change with average temperature due to speed of sound. At high engine loads, more fuel is added in a diesel engine, and exhaust temperature coming via EI is higher. This slightly increases wave speeds, and the effect is stronger there is more hot gas occupying the length of the channel. But often engine speed may not increase but rather decrease as load increases. Too much EGR will reduce oxygen in the cylinder and prevents engine load being met.

Figure 5.1 shows the comparison between Comprex operations at low-speed and high-speed. With the inclusion of pockets, it is needed to ensure that the cycle simulation starts and ends at an instant in the cycle when the channel is fully closed. For this reason, the cycle simulation starts shortly after the AI port closes, unlike in the previous chapters. This type of simulation approach will be discussed in Chapter 6. The AO port (on the left side) opens at around 30 degrees and closes at about 48 degrees in the depicted results.

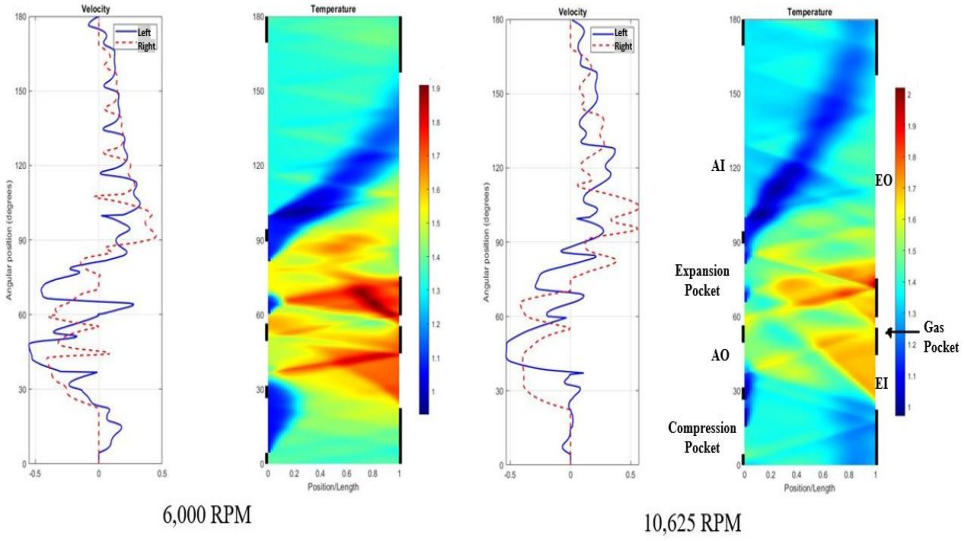

Figure 5.1. Velocity profiles and Temperature during a Comprex cycle

It should be noted here that the performance of PWS is highly dependent on the AO and EI pressures and the EI temperature. These represent boundary conditions provided to the wave rotor code to simulate realistic operational situations. Unfortunately, limited experimental test data is available on the empirical testing of Comprex under realistic condi-

tions. The results depicted by the computational simulations need some insightful qualitative assessment to picture the working of Comprex under varying rotor speed.

5.2 Variable Speed Test on Comprex

5.2.1 Variable Speed Test 1

It has been previously seen that the wave rotor analysis codes are able to predict the performance of Comprex like wave rotors with an acceptable margin of errors. This section aims to investigate the performance of Comprex under varying rotor speed. The pressure and temperature boundary conditions are held constant in this section to only focus on the parameters influenced by the variable speed. The Comprex geometrical boundary conditions are same as described in Chapter 4. The reference pressure and temperature used in this study are 14.7 psi and 518 R, respectively. At the EI port, non-dimensional stagnation pressure was assumed to be 1.89, and the non-dimensional stagnation temperature of 1.73 was imposed. The dimensionless static pressure used at the AO port was 1.44. The properties at the EO port were considered to be standard atmospheric. The Comprex was regarded as a four-port wave rotor, and the wall-pockets were excluded from the simulations.

The specifications of Mazda 2.0 D engine have been given in section 4.2. Using the Comprex pulley ratio, noted by Smith in ref. [32], as 4.25:1, the following data was obtained.

Table 5.1. Flow rates to the EI port for different rotor speeds

Engine Speed (RPM)	Comprex Rotor Speed (RPM)	Mass Flow Rate (lb/min)
1,000	4,250	5.30
1,500	6,375	7.95
2,000	8,500	10.59
2,500	10,625	13.11
3,000	12,750	15.89
3,500	14,875	18.54
4,000	17,000	21.19
4,500	19,125	23.84

The engine speed range from 2,000 RPM to 4,000 RPM was chosen to simulate the performance of Comprex. The rotor speeds were changed accordingly to see the effect of variable speed on the mass flow rate through each port. In reality, the pressure and tem-

perature values at the EI port will differ with the change in engine speed. As the pressure of supercharged air is dependent on the pressure of exhaust gas, the static pressure values at the AO port will also vary accordingly. The temperature of exhaust gas coming in plays a crucial role in gas dynamics of the shock waves. It is challenging to find the relations between the change of properties following the change in speed. Table 5.2 indicates the mass flow rates through each port under variable rotor speed, predicted by the SCW1D program. It is emphasized that the boundary conditions correspond to the referenced experiment and not actual diesel engine operating conditions, and thus mass flow for EI can exceed that for AO sometimes substantially.

Table 5.2. Mass flow rate for variable rotor speeds (four-port)

Rotor Speed (RPM)	Rotor Speed (RPM)			
	AI	AO	EI	EO
8,500	9.8	13.02	7.58	11.01
10,625	12.32	11.47	11.75	11.14
12,750	13.39	5.82	17.00	9.77
14,875	15.22	5.5	22.41	12.99
17,000	12.43	2.86	22.54	13.21

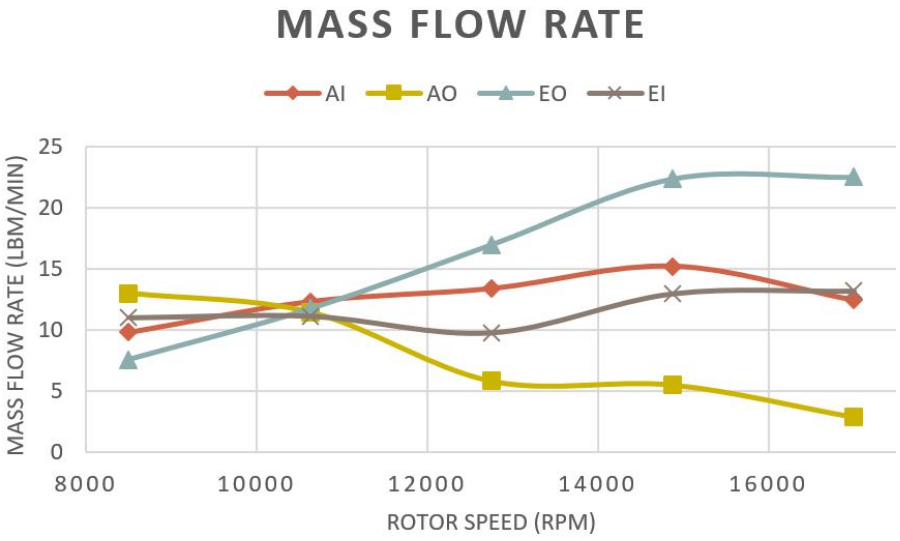

Figure 5.2. Mass flow rate variation for variable speed (four-port)

Figure 5.2 indicates the effect of speed fluctuations on the low-pressure scavenging in the case of four-port Comprex design. As the speed increases, the mass flow rate through the EO port tends to go up. In contrast, the mass flow rate through AO port seems to decrease drastically following the increased rotor speed. In reality, the increased engine speed indicates a reduced engine load. During the low load events, the airflow to the engine is also cut down.

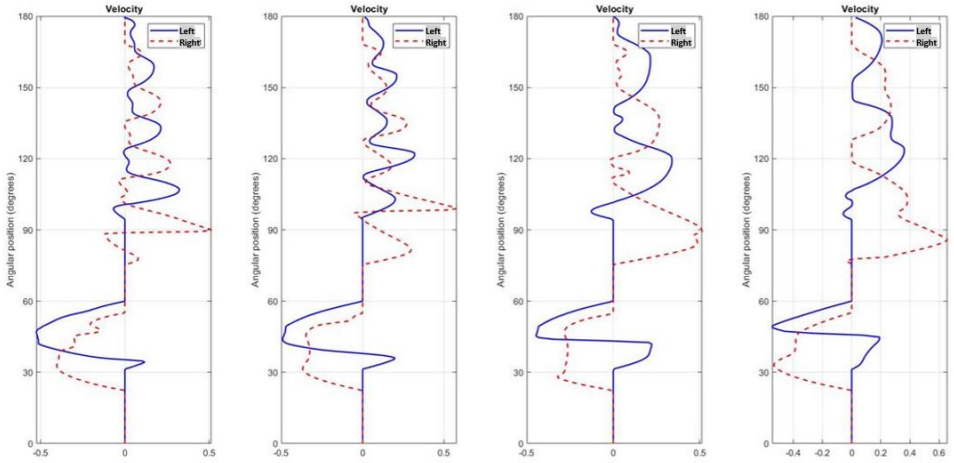

Figure 5.3. Velocity profiles for variable speed (four-port); (Left to right- 8,500 RPM, 10,625 RPM, 12,750 RPM, 14,875 RPM)

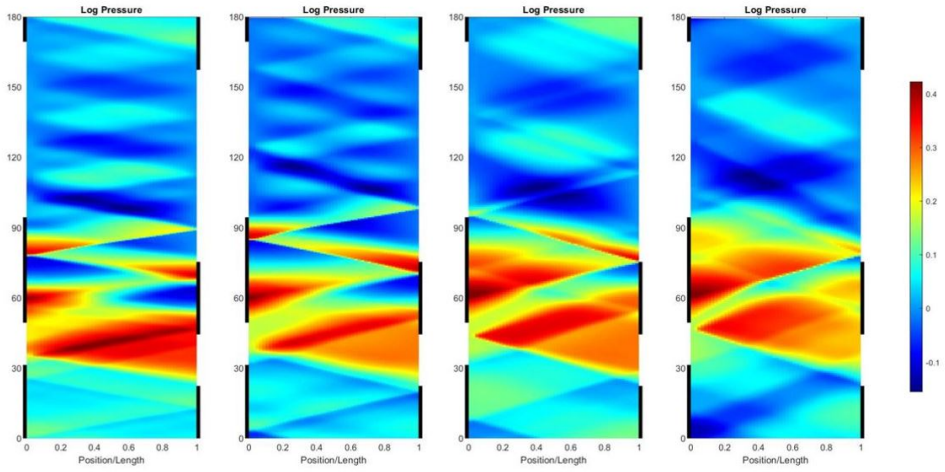

Figure 5.4. Pressure distribution for variable speed (four-port); (Left to right- 8,500 RPM, 10,625 RPM, 12,750 RPM, 14,875 RPM)

The velocity profiles given in figure 5.3 explain the mass flow rate variation under the change in speed. The following simulations have been conducted using the same 'high-pressure to low-pressure' approach. The port opening and closing locations can be seen in figure 5.4, which indicates the shift of shock incidence per change in rotor speed. The left and right sides designate the cold (air) and hot (exhaust) sides, respectively. The high-pressure part is at the bottom, whereas the top portion is the low-pressure part. The boundary conditions are chosen from the 2,500 RPM test point from Smith's experiment. Therefore, the results at 2,500 RPM engine speed (10625 RPM rotor speed) seem more promising. Since the pressure and temperature boundary conditions are constant, the velocity of shock waves inside the Comprex channels is unchanged. Hence the point of shock incidence shifts upwards following the increased angular velocity of the rotor. In real practice, the increasing engine speed points to the higher velocity in the exhaust manifold. So, the stagnation properties at the EI port are expected to be higher. Higher stagnation temperature results in higher shock speed, causing the compression wave to arrive earlier at the AO port. Hence the mass flow rate through the AO port remains largely unaffected. Yet the problem of poor low-pressure scavenging needs to be addressed in four-port wave rotors.

5.2.2 Variable Speed Test 2

The results of another variable speed test conducted on the Comprex geometry are presented in this section. The reference pressure and temperature are same as the previous case, 14.7 psi and 518 K, respectively. The non-dimensional static pressure of 1.47 was used at the AO port. The dimensionless exhaust gas pressure and temperature were assumed to be 1.78 and 1.66, respectively. Standard atmospheric conditions were applied at the EO port. The rotor speed was changed from 9,420 RPM to 15,000 RPM.

The mass flow rates through each port are listed in Table 4.3. Figure 5.5 shows the variation in mass flow rates through each port as the rotor speed changes. Comparing figure 5.5 with figure 5.2, it can be inferred that the variable speed can influence the performance of Comprex-like PWS differently for different boundary conditions. The essential boundary conditions applied at the ports are major key-holders in deciding the mass flux through each port. They can either reinforce or compensate for the effects of variable rotor speed of the

Table 5.3. Computed mass flow rate for variable rotor speeds (four-port)

Rotor Speed (RPM)	Mass Flow Rate (lbm/min)			
	AI	AO	EI	EO
9,420	9.4	9.44	9.54	9.27
10,000	10.08	9.78	10.21	10.77
11,000	11.26	8.06	10.02	12.88
12,000	9.11	9.94	11.76	11.22
12,960	9.5	9.13	11.18	11.8
14,000	10.14	8.71	9.59	11.2
15,000	10.44	7.74	8.88	11.78

PWS. The overall Comprex cycle comprises several individual phenomena. It is possible to tune in the individual phenomena to attain the optimum operation.

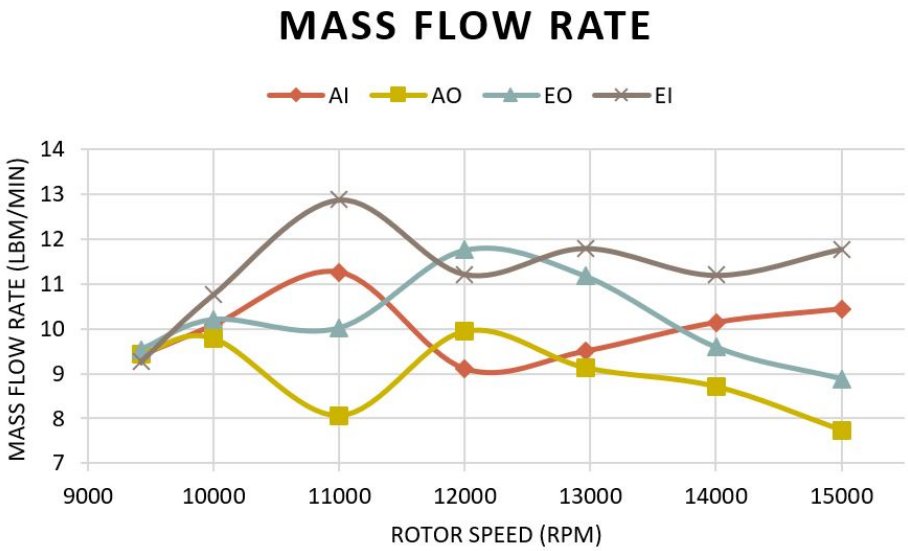

Figure 5.5. Mass flow rate variation for variable speed (four-port)

6. NUMERICAL SIMULATION OF PWS WITH POCKETS

6.1 High-Pressure to Low-Pressure Simulation Approach

In order to accommodate all three pockets in a four-port PWS simulation using the codes, some modifications had to be made to the conventional port arrangement approach. In conventional PWS simulation approach, a cycle starts from the low-pressure part, by first discharging the channel by opening it to the EO port. Since the AI port opens after the EO port, corresponding port closing locations are also delayed. The last port closing will be at the trailing edge of the AO port. Since the channel goes from low-pressure to high-pressure part, the actual function of the expansion pocket can not be simulated. Also, the location of expansion pocket is delayed in the direction of rotation, placing it much above the gas pocket. Further, an essential computational requirement is to close both ends of the channels at the cycle end. With this in consideration, it is not possible to simulate the compression pocket. Still the simulation of expansion and gas pockets is possible. It is also possible to simulate each pocket separately and together to investigate other possibilities while scaling customized PWS. This approach has been successfully tested by S. Basu at the Combustion and Propulsion Research Laboratory at IUPUI and has been documented in internal references [24] and [25]. Different pocket combinations were simulated with Comprex geometry and results were compared with each other.

In this work, a different approach called as 'high-pressure to low-pressure approach' was developed to accommodate all three pockets provided in the Comprex PWS. The important feature here is to just shift the cycle starting location from the low-pressure part to the high-pressure part. A well-converged four-port Comprex simulation case was taken for reference to compare the end results. Figure 6.1 shows a well-converged four-port Comprex cycle with simulation results.

In the figure 6.1, the change of position of the pockets can be imagined. But if the phase of the cycle is shifted from current start time to somewhere just above the trailing edge of the AI port, all three pockets can be incorporated. To save the computational time while testing the phase-shifting approach, the conditions in each computational cell at the end of low-pressure part were obtained and used as initial conditions to simulate the phase-changed

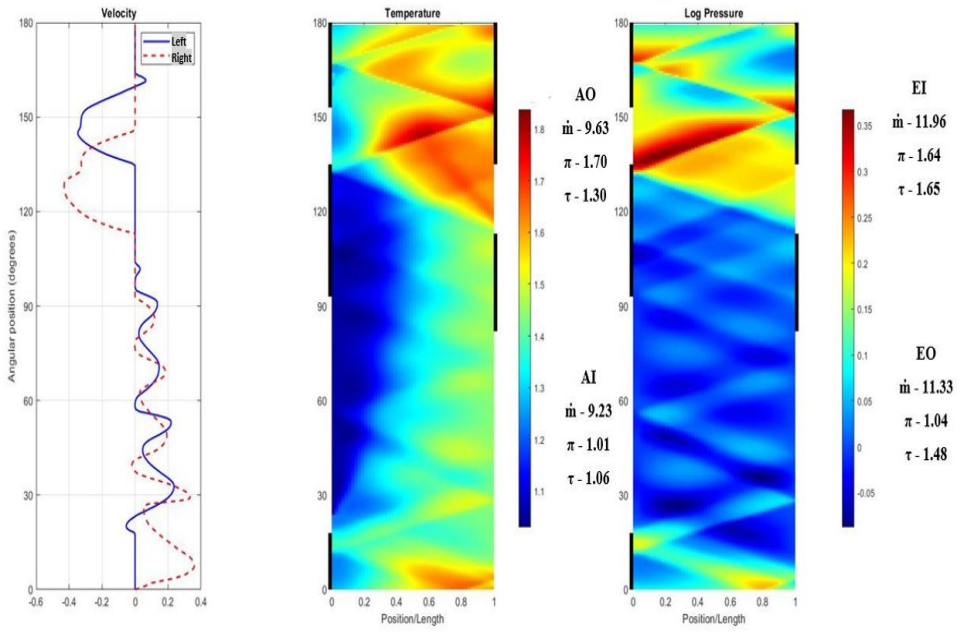

Figure 6.1. Low-pressure to high-pressure simulation approach

cycle. To obtain the properties in each computational cell at the end of low-pressure part, only the low-pressure part was simulated using the SCW1D-A code. The cycle end time was selected to be the AI port closing time plus the passage width. Doing so, just enough space can be obtained at the end of phase-changed cycle to close both ends of a channel, saving sufficient angular length to accommodate the pockets. Figure 6.2 shows the low-pressure part simulation.

The high-pressure to low-pressure cycle starts from the location where the low-pressure part simulation ends. This is a new reference start time. Remaining positions from the reference start time were calculated without changing the port angles. The properties in each computational cell, calculate by code at the end of low-pressure part simulation, are used as initial conditions to simulate the remaining cycle which starts from the new reference. This is a new approach developed during this work to incorporate the Comprex wall-pocket combination.

Figure 6.3 shows the high-pressure to low-pressure simulation approach. This approach gives a convenient way to relate the reversed cycle analysis of the Comprex without disturbing the conventional nomenclature familiarity. Further, the simulation results are precisely same

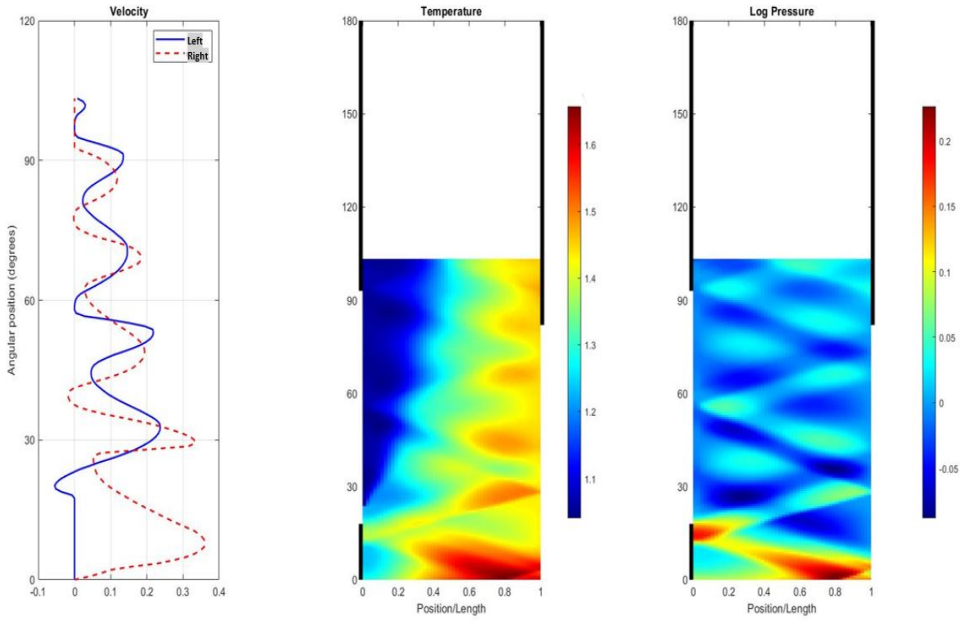

Figure 6.2. Comprex low-pressure part simulation

as the four-port Comprex simulation results. The simulation can be carried out for multiple cycles and eventually runs to convergence. Further, if the initial conditions are set according to the reference pressure and temperature, as those were set in the four-port simulation, it gives promising results exactly similar to the four-port simulation. For same number of iterations, the same results are computed by the two approaches. Hence this approach can be conveniently used for other four-port PWS simulations.

In figure 6.3, the direction of rotation is in the direction of positive Y-axis. On the left side, in the direction of rotation the first port (lower) is AO port and the second port (upper) is AI port. On the right side, in the direction of rotation, the first port (lower) is EI port and the second port (upper) is EO port.

In above geometry, it is possible to incorporate all three pockets at their relevant positions. The expansion pocket can be specified between the trailing edge of AO port and the leading edge of AI port. The gas pocket will be between the trailing edge of EI port and the leading edge of the EO port. The location of compression pocket is between the trailing edge of AI port and the leading edge of AO port. As there is sufficient space available at the beginning of the cycle and the leading edge of AO port, a compression pocket can be simulated.

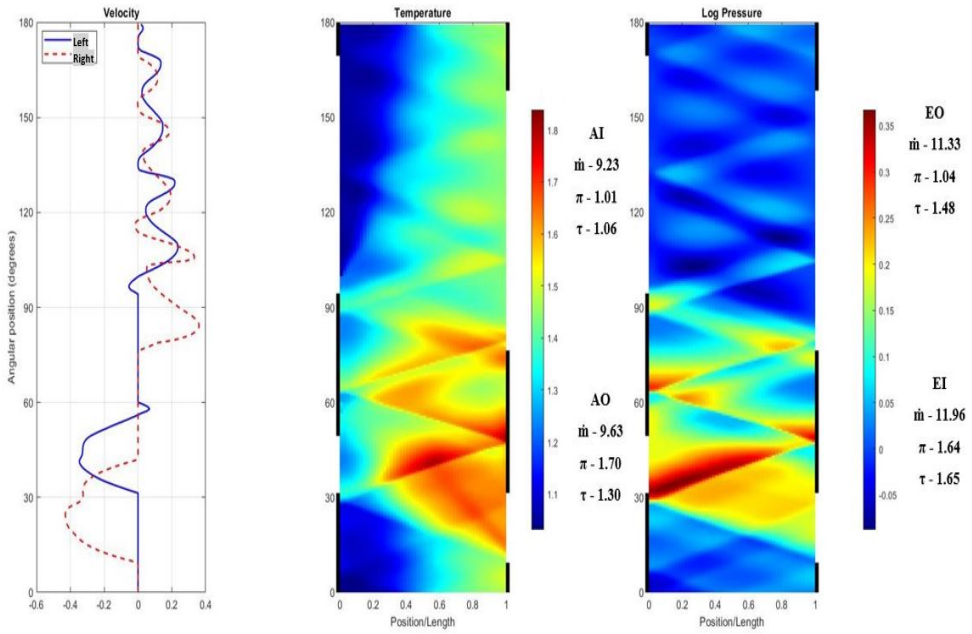

Figure 6.3. High-pressure to low-pressure simulation approach

6.2 Pocket Combination for Four-Port PWS

The effects of variable speed on the performance of a four-port PWS have been discussed in the previous chapter. To briefly summarize, the off-design rotor speed causes improper shock arrivals, giving rise to undesirable backflows. Under engine high-load and low-speed conditions, the rotor speed is substantially reduced below the design point, leading to improper low-pressure scavenging and excessive exhaust gas recirculation. The rotor speed must be held nearly constant or in fact may need to be slightly higher to achieve optimal wave arrival timing, especially the arrival of the strong compression shock from EI to AO. However, it is not always possible to maintain the rotor speed at the design point, especially when the PWS is directly driven by the unit to be supercharged.

The Brown Boveri solution to provide the extension for variable speed and load range to a four-port PWS involves constructing the wall-pockets between the high and low pressure parts. The provision of wall-pockets provides the Comprex an significant extension of the operating range in the direction of low speeds [10]. Figure 6.4 shows the Comprex air and exhaust manifolds with pocket arrangements.

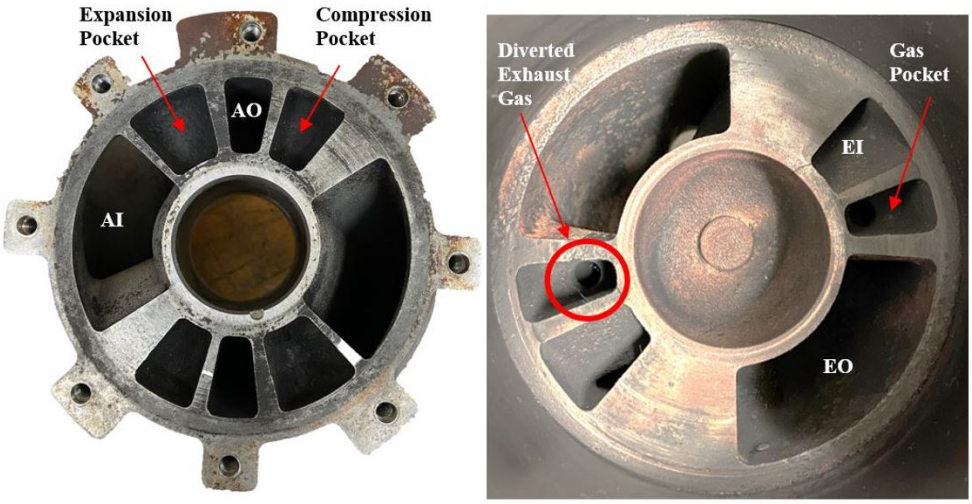

Figure 6.4. Comprex air (left) and exhaust (right) stator endplates

The commercial Comprex unit has three wall-pockets machined in the endplates. In figure 6.5, the direction of rotation is along the positive Y-axis. A gas pocket is provided in the region between the trailing edge of EI port and the leading edge of the EO port, in the direction of rotation. Similarly, an expansion pocket is provided between the trailing edge of AO port and the leading edge of the AI port. Gas pocket and expansion pocket work in conjunction to create the necessary high-pressure zone between the low-pressure part and high-pressure part of a four-port wave rotor. A compression pocket is provided in the cold stator plate between the trailing edge of AI port and the leading edge of AO port. Its purpose is to assist the pre-compression of the fresh air, before it is compressed by the primary compression wave originating from the high-pressure inlet port. A new 'high-pressure to low-pressure' simulation approach was developed during this study to accommodate the pocket combinations. Figure 6.5 explains the ideal wave diagram for a four-port PWS operating at the design speed.

For optimum results, in order to avoid the discharge of contaminated gases into the AO port, the high pressure interface (HPI) initiating from the leading edge R1 of the EI port, must terminate at the trailing edge L2 of the AO port. The primary compression wave, C-R1L1, originates from the leading edge of EI port and reflects on the leading edge of AO port. If the reflected wave RC-R1L1 is a compression acceleration wave, the flow speed in

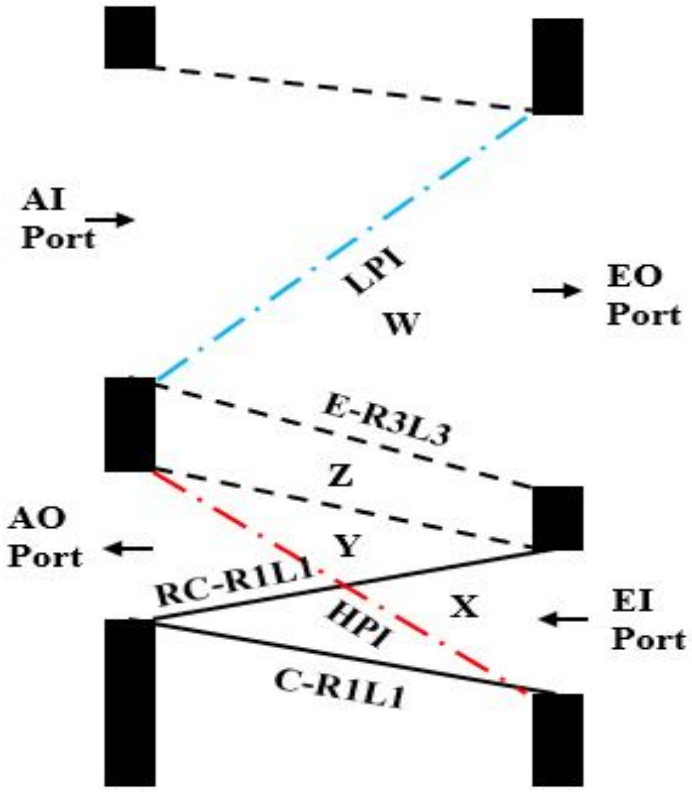

Figure 6.5. Ideal wave diagram for a four-port PWS operating at design speed (high-pressure to low-pressure approach)

the rotor will be decreased and leads to rise of pressure in the region Y. Hence the pressure in region Y will be somewhat greater than the pressure in region X. This scenario results into decreased mass flow rate through the AO port. On the contrast, if the reflected wave R1L2 is an expansion acceleration wave, it will increase the flow speed in the rotor, thereby boost the mass flow rate through the AO port.

For proper operation, it is also essential to facilitate the complete low-pressure scavenging. It can be achieved only if the low pressure interface (LPI) terminates at or before the trailing edge R4 of the EO port. Failing to attain the termination of LPI at least at the EO port closure will lead to trapping the exhaust gas present in the region W, which will subsequently be recirculated to to the engine. To avoid the incomplete low-pressure scavenging, certain sufficient flow speed is necessary in the region W. The flow speed in the region W depends on the pressure in region Z. However, the pressure in region Z depends on the pressure in

region Y. SO, in order to maintain sufficient flow rate in the region W, the pressure in region Y should be higher. The pressure in region Y is determined by the mass flow rate through the AO port, in a sense that the increased mass flow rate through the AO port will decrease the region Y pressure and vice versa. The AO port mass flow rate is a function of the engine demand. Higher the engine demand, higher would be the mass flow rate through the AO port and lower would be the pressure in region Y. In other words, if the engine load is increased, the engine demand would be higher. The elevated mass flow rate through the AO port will reduce the pressure in region Y, jeopardizing the low-pressure scavenging.

Figure 6.3 shows the wave diagram for a four-port PWS operating at a speed far below the design speed. As the cycle starts, the channels will be opened to the leading edge R1 of the EI port. The primary compression wave C-R1L1 will penetrate the channels. It will arrive the left end of the channel too early before the opening of AO port and reflect on the closed end of the channel. The pressure behind this reflected wave RC-R1L1, that is the pressure in region X' will be much higher than the pressure in region X. In fact the pressure in region X' exceeds the pressure at the EI port, forming the backflow, indicated by arrow 51, through the EI port. As the cycle continues, the channels will be exposed to the AO port and an expansion wave E-L1R2 will travel into the channel reducing the pressure in region Y. The pressure in region Y may be higher or lower than the pressure in region X, the difference being relatively small. However, the pressure in region X' is substantially high as compared to the pressure in region X. The expansion wave E-L1R2 reflects on the open port EI and reestablish the inflow conditions through the port EI as indicated by arrow 52. The compression wave RC-R1L1 reflects on the open port as a compression wave and reduces the pressure in region Y', thereby causing the undesirable flow reversal through the AO port indicated by arrow 11. Consequently, the expansion wave E-L1R2 reflects on the open port EI as a compression wave and reestablishes the outflow conditions at AO port after reaching the left end of the channel, as indicated by arrow 12.

Upon the closing of EI port, an expansion acceleration wave will be generated from its trailing edge R2. The expansion wave traveling from the trialing edge of EI port to the trailing edge of AO port, will arrive at the left end of the channel before the closing of AO. The pressure behind this expansion wave, that is in the region Z will be significantly lower as

compared to the pressure existing in the high-pressure part of the cycle. Hence an additional undesirable flow reversal will emerge at the AO port, indicated by arrow 13.

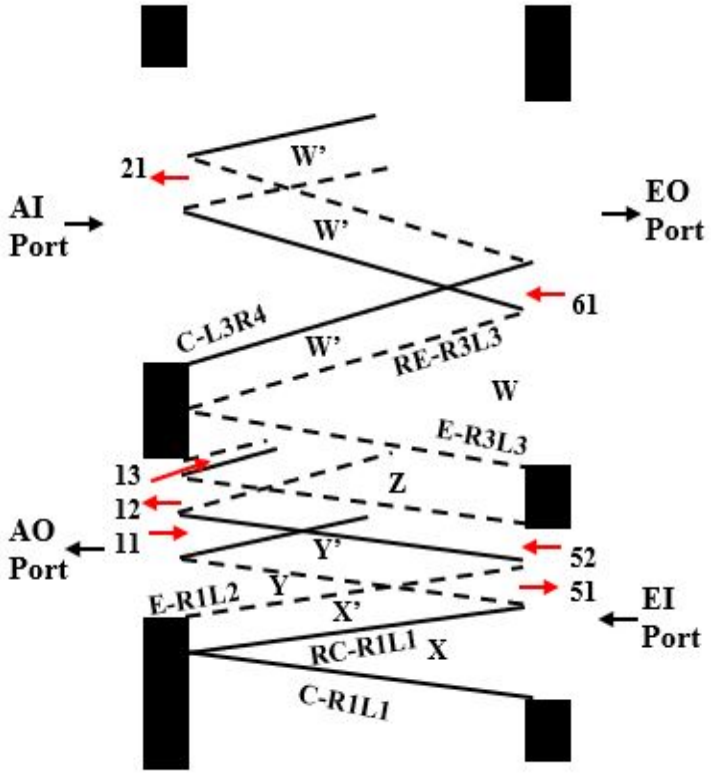

Figure 6.6. Wave diagram for reduced rotor speed operation (high-pressure to low-pressure approach)

In the low-pressure part, an expansion wave E-R3L3 will originate as the channels are opened to the EO port. The pressure behind this wave will be lowered to almost atmospheric value and it will arrive the left end of the channel before the opening of AI port. Despite the low pressure in region W, the direction of flow will still be towards the EO port. However, the reflected expansion wave RE-R3L3 will create further reduction in the pressure in region W'. Upon arrival at the EO port, the backflow will occur in the region W' as shown by arrow 61. As the rotor continues, the compression wave C-L3R4 will travel into the channels and restore the outflow conditions upon reaching the EO port. The region W' bounded by the reflected waves continues to reciprocate into the channel and results into the flow reversal at the AI port, as the arrow 21 indicates. The inflow conditions will be shortly

restored by the reflected waves following the region W'. At the lower speed of the rotor, mass flow rate through the AO port will be larger and it will reduce the pressure in region Y. Also, the undesirable backflows will be emerged as a result of incorrect wave timings. These phenomena are counterproductive for the low-pressure scavenging process.

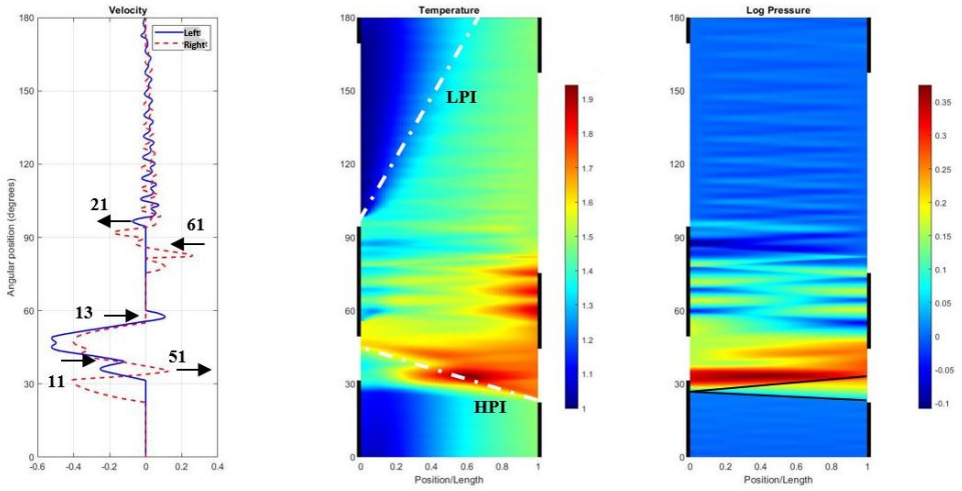

Figure 6.7. Four-port PWS operating below speed

Figure 6.4 shows the operation of a four-port PWS below design point. In temperature diagram, it is clearly visible that the low-pressure interface does not terminate before the closure of EO port. As a result, excessive exhaust gas recirculation takes place at the AO port. Similarly, the flow reversals can be identified by corresponding arrow numbers used in figure 6.3. The regions Y' and Z have fairly low pressures as compared to the region X'. The pressure below the region Z is approximately equal to the reference states used at the AI port. Low-pressure zone at the region Z qualifies the flow speed in the region W. As stated earlier, this scenario signifies the incomplete low-pressure scavenging.

This simulation was conducted using the SCW1D-A program and the rotor speed of 3000 RPM was used. The mass flow rates through the EI and AO port were observed to be around 9.40 lbm/min. On the other hand, the mass flow rates through the EO and AI port were significantly depleted to reach the value of about 1.64 lbm/min. Jose et al. in ref. [23] have presented a combination of arrangements to provide four-port PWS a variable speed and load range extension in the low-speed direction.

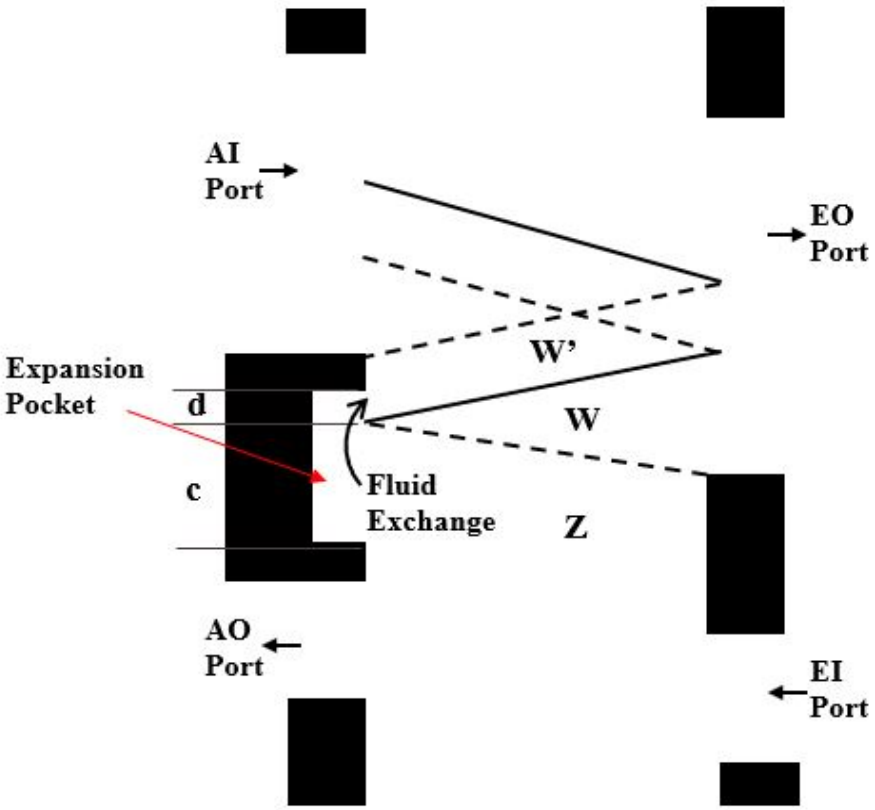

Figure 6.8. Working principle of expansion pocket

The first construction is provided between the trailing edge of the AO port and the leading edge of the AI port. This recess in the airside manifold is referred to as an expansion pocket. The purpose of expansion pocket is to mitigate the harmful effects of expansion wave originating from the leading edge of the EO port. It has been discussed earlier how this expansion wave causes backflows at the EO port, thereby hindering the low-pressure scavenging process. The location of expansion pocket is determined such that the early arriving expansion wave will be incident on the pocket. The expansion pocket allows the exchange of fluid between the region Z and region W', as shown in figure 6.5. In four-port wave rotors operating at lower speeds, the pressure existing in the region W' is almost below atmospheric pressure, which causes undesirable backflows at certain locations. The expansion pocket allows the high-pressure fluid from region Z to pass through the pocket into the region W' and eliminates the flow reversals. Depending on the pressure existing

in region Z, the pressure available in region W' can be greater than the pressure present in region W. However, to attain proper working of the expansion pocket, it necessary to maintain the sufficient pressure in it. The expansion pocket pressure solely depends on the pressure available in region Z. It has been explained previously that the pressure in region Z might be fairly low when the rotor is rotating at lower speed. Another factor that directly affects the expansion pocket pressure, is the location of incidence at the pocket. The arrival of expansion wave originating from the leading edge of the EO port divides the pocket in two sections. The lower section 'c' is exposed to higher pressure region Z and upper section 'd' is exposed to the lower pressure region W'. If the rotor is rotating at very low speed, the lower section 'c' will be shorter and upper section 'd' will be longer. This means the flow going into the pocket through 'c' will be less than the flow leaving the pocket through 'd'. In such condition, the pocket pressure will be substantially reduced. Also, during the low speed operation, the pressure in the region Z will be lower. Hence, the expansion pocket standing on its own might be less efficient at lower rotor speeds.

The expansion pocket pressure needs to be maintained to overcome the pressure drop in it. A gas pocket is provided to branch off some high-pressure gas from the exhaust manifold of the engine (or from some other high-pressure zones such as X') to improve the pressure in region Z. The location of gas pocket is between the trailing edge of the EI port and the leading edge of the EO port, as shown in figure 6.6. A simple and practical means to facilitate the high-pressure fluid into the region Z is to provide a smaller cross-section duct from the exhaust manifold to the gas pocket. This type of construction can be seen in figure 6.1, denoted by a circle. Yet another way is to extend the portion of gas pocket up to the EI port, by forming a gap between the hot stator plate and the rotor exit plane on the hot side, as denoted by the shaded region in figure 6.6. The high-pressure fluid entering the rotor from the gas pocket will form a high-pressure band Z' between the regions Z and W. The pressure of Z' will be equal to higher than the pressure at Z. The gas and expansion pocket working in conjunction give outstanding low speed and load operability to a four-port PWS [23].

Additionally, a compression pocket is provided between the leading edge of AO port and the trailing edge of AI port. The purpose of compression pocket is to enable the pre-

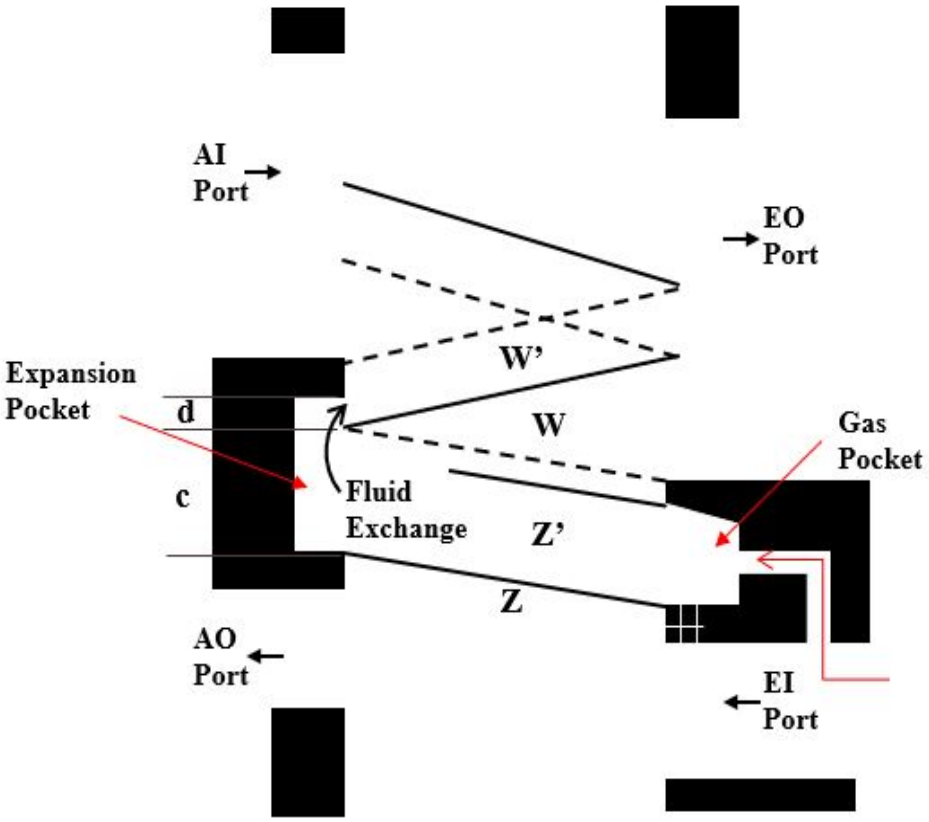

Figure 6.9. Working principle of gas pocket

compression stage before the primary compression. The compression of fluid starts when AI port closes and the gas inside the channel comes to halt. The waves incident on the compression pocket further boost the pressure of fluid at the beginning of the cycle. A four-port PWS equipped with all three pockets becomes very elastic and exhibits variable speed and load operations.

6.3 Numerical Modeling of Pocket Combination

The numerical modeling of the wall-pockets discussed in the previous subchapter has been performed using a simple lumped volume technique, patterned after the modeling of the combustor in a gas-turbine topping cycle wave rotor simulation at NASA using the Q1D code [28]. The first computational cell of a passage is exposed to the left-side of the cycle, that is to the cold stator plate. The computational cell designated by the subscript 0 is the

cell where port boundary conditions are applied. Here, a pocket has been treated as port. Hence, the mass and energy fluxes through the computational cell denoted by the subscript 0 can be used to update the conditions in the cold-side pockets, that are expansion and compression pockets. On the left side, the pocket density and pressure can be integrated using the continuity (eq. 6.1) and energy (eq. 6.2) equations as follows.

$$\rho_{poc}^{n+1} = \rho_{poc}^{n} - (\frac{b.h.L}{V_{poc}})(\sum_{k=1}^{N_{poc}} [F_1]_{\mathrm{i}=0,k}^{n})\Delta t \tag{6.1}$$

$$P_{poc}^{n+1} = P_{poc}^{n} - (\frac{b.h.L}{V_{poc}})\gamma(\sum_{k=1}^{N_{poc}} [F_3]_{\mathrm{i}=0,k}^{n} + \sum_{k=1}^{N_{poc}} [F_1]_{\mathrm{i}=0,k}^{n}.\frac{\gamma-1}{2}(\frac{\omega.R}{a^*})^2)\Delta t \tag{6.2}$$

Similarly, the last computational cell of a passage is exposed to the right-side of the cycle. The subscript M designates the last computational cell of a passage. The subscript M+1 denotes the computational cell where the right-side port boundary conditions are applied. Hence, the mass flux through the computational cell denoted by M+1 can be used to update the properties in the gas pocket, which in in the hot side stator plate.

Here, a port between the EO and EI ports can be used as a gas pocket. There are two approaches to simulate the gas pocket. First, it can be treated just like an expansion pocket with higher pressure and temperature boundary conditions. With this approach, the gas state in the pocket can be integrated using the continuity (eq. 6.3) and energy (eq. 6.4) equations as follows.

$$\rho_{poc}^{n+1} = \rho_{poc}^{n} + (\frac{b.h.L}{V_{poc}})(\sum_{k=1}^{N_{poc}} [F_1]_{\mathrm{i}=M+1,k}^{n})\Delta t \tag{6.3}$$

$$P_{poc}^{n+1} = P_{poc}^{n} + (\frac{b.h.L}{V_{poc}})\gamma(\sum_{k=1}^{N_{poc}} [F_3]_{\mathrm{i}=M+1,k}^{n} + \sum_{k=1}^{N_{poc}} [F_1]_{\mathrm{i}=M+1,k}^{n}.\frac{\gamma-1}{2}(\frac{\omega.R}{a^*})^2)\Delta t \tag{6.4}$$

The superscript n indicates the discrete temporal index $n\Delta t$ and the subscript i indicates the spatial index iΔx, with ratio of $\frac{\Delta t}{\Delta x} = 0.2$, with $\Delta x = 0.02$ Here, ρ_{poc}, and P_{poc} are the pocket density and pressure, respectively. L, h and b are the passage length, height and width, respectively. V_{poc} is the pocket volume. N indicates the number of passages, whereas k indicates the individual passage numbers. M represents the last computational cell in the computational domain.

Another approach to model the gas pocket is to simply consider it as port since it does not have any significance in fluid exchange. The main purpose of gas pocket is to maintain the high pressure in expansion pocket. The flow coming in through the gas pocket is diverged from the engine exhaust manifold and supplied to the pocket through a duct. The duct opening into the pocket can be considered as a small cross-section port. Both approaches have been discussed in the next subchapter. The first approach can not signify the actual working principles of the pocket-combination as the pocket pressure is updated after each cycle and it is adjusted according to the adjacent computational cells. However, this approach is important to identify the computational efficiency of the introduced model. The second approach is more plausible and gives promising results.

6.4 Numerical Simulation of Pocket Combination

6.4.1 Pocket Simulation Method-I

As explained earlier, the gas pocket can be modeled by treating it either like an expansion pocket or like an auxiliary high-pressure fluid introducing duct. In method- I, the gas pocket has been simulated in same fashion as the expansion and compression pockets. The purpose here was to allow the fluid passage from the high-pressure area to the low-pressure area first through the gas pocket and then through the expansion pocket.

The following simulation was performed using the SCW1D code to simulate the Comprex cycle. The reference pressure and temperature are 14.7 psi and 518 R. At the EI port, non-dimensional stagnation pressure was assumed to be 1.89, and the non-dimensional stagnation temperature of 1.73 was imposed. The dimensionless static pressure used at the AO port was 1.44. The properties at the EO port were considered to be standard atmospheric. Also, other boundary conditions and input parameters are same as used in the pocketless Comprex simulation in the previous chapter. The rotor speed used was 8,500 RPM.

Figure 6.10 shows the locations of wall-pockets. The direction of rotation is along positive Y-axis. The inflow and outflow port locations are same as shown in figure 6.9. Once the pockets are specified at desired locations, the port numbering will be changed. In figure 6.10, in the direction of rotation, on the left side (cold stator plate) there are compression

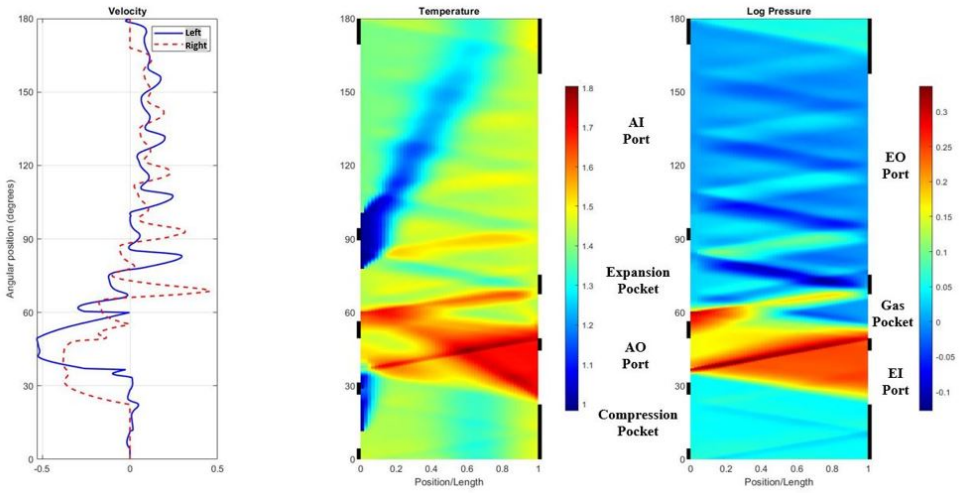

Figure 6.10. Comprex simulation with pockets (Method-I)

pocket, AO port, expansion pocket and AI port, respectively. Similarly, on the right side (hot stator plate), there are EI port, gas pocket and EO port, respectively. From this point on, the same port numbering will be used for each simulation included in this chapter.

In the method I, there is no inflow through the gas pocket. It is assumed to perform in the same way as the expansion pocket. Though this approach does not describe the actual functioning of the gas pocket, the simulations performed using this method can be used to verify if the pocket modeling affects the mass flow rate through other inflow and outflow ports. Table 6.1 show the variable speed test performed on the PWS with pockets.

The pressure and temperature boundary conditions used here are same as those in the variable speed test 1, in section 5.2.1. The wall-pockets have been included in the same the same PWS geometry. The rotor speed was varied from 8,500 RPM to 17,000 RPM.

Table 6.1. Variable speed test on PWS with pockets (Method-I)

Rotor Speed (RPM)	Rotor Speed (RPM)			
	AI	AO	EI	EO
8,500	7.61	11.7	7.52	11.68
10,625	10.22	11.15	11.09	12.14
12,750	12.6	7.65	16.11	11.26
14,875	12.71	4.34	19.68	11.46
17,000	12.92	3.77	21.59	12.57

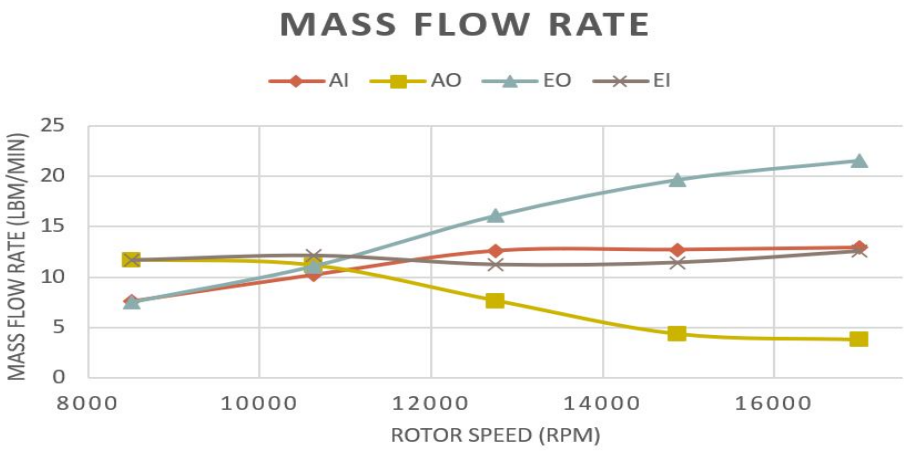

Figure 6.11. Mass flow rate variation for variable speed (PWS with pockets, Method-I)

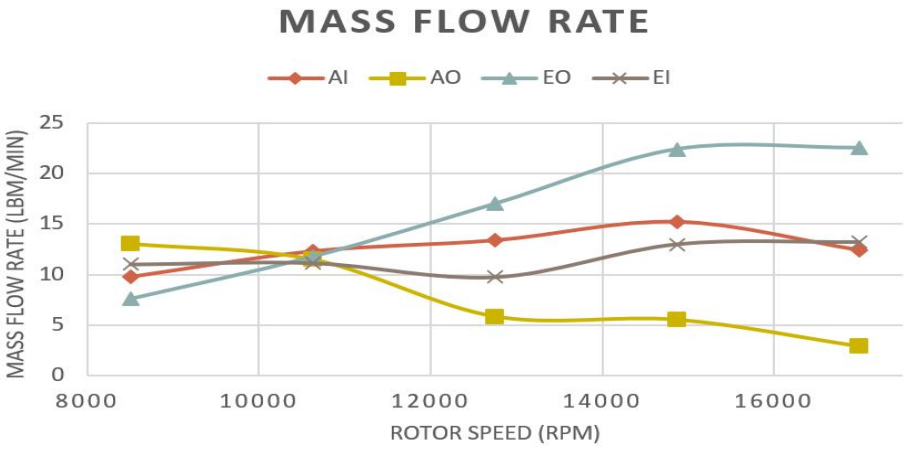

Figure 6.12. Mass flow rate variation for variable speed (four-port)

Figure 6.11 shows the results of variable speed test simulation of a PWS with pockets. Figure 6.12 shows the results of same test performed on a four-port pocketless PWS geometry. It can be observed that the mass flow rate through each port remains largely unchanged. As the pocket pressure and temperatures are updated after each cycle, it is impossible to maintain the necessary pocket pressure in the expansion pocket without any sort of fluid exchange from the high-pressure zones. Eventually, this might lead the cycle to behave like a four-port cycle. A gas pocket is provided to constantly supply the high-pressure fluid to maintain sufficient pressure in the expansion pocket.

6.4.2 Pocket Simulation Method-II

The objective of gas pocket is to establish a high-pressure zone in the region Z', as shown in figure 6.13. In Comprex-like PWS, it is achieved by diverting some exhaust gas into the rotor through the gas pocket. Hence, the gas pocket can be treated as an inflow port. In Comprex CX-93, the portion of gas pocket is extended up to the EI port by forming a narrow gap between the rotor-end and the hot-side stator plate. The flow coming through EI port is allowed to pass through the gap into the gas pocket. The trailing edge of gas pocket is slanted by some angle to extend the width of high-pressure band denoted by Z'. Some other versions of Comprex are provided with a narrow duct originating from the exhaust manifold and opening into the gas pocket. The flow coming into the EI port is allowed to pass though the duct and taken into the rotor through gas pocket. For computational simplicity, the duct opening into the exhaust port has been considered as an inflow port.

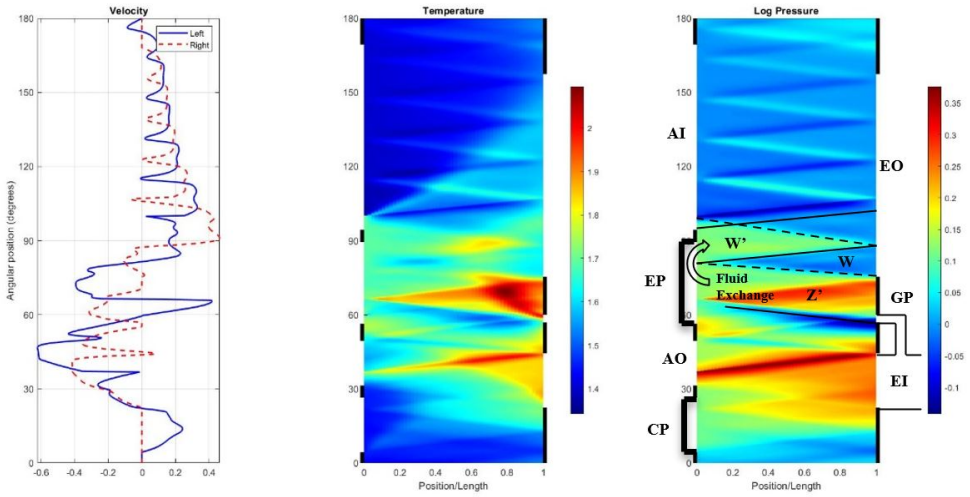

Figure 6.13. Comprex 6,000 RPM simulation with pockets

The simulation results shown in Figure 6.13, illustrate the working of Comprex with pocket combination. The rotor speed of 6,000 RPM was used for this simulation. The port pressure and temperature boundary conditions are same as discussed in the previous section. In the temperature diagram, the low pressure interface can be seen terminating much before the trailing edge of the EO port and assures the low exhaust gas recirculation. Introduction of the exhaust gas from the gas pocket can be visualized by the interface created at gas

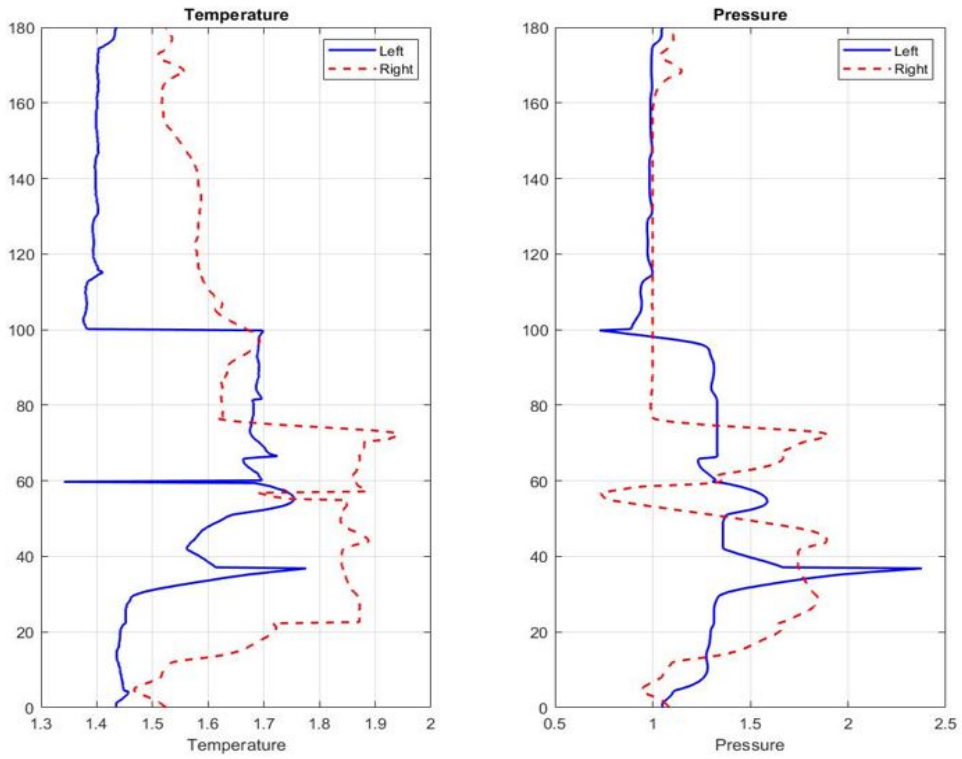

Figure 6.14. Temperature and Pressure variation over the cycle (Comprex with pockets)

pocket opening. The high-pressure region Z' established by the gas pocket can be seen in the pressure diagram. As the rotor is rotating at lower speed, the primary expansion wave originating from the leading edge of the EO port arrives at the expansion pocket. In a four-port PWS, the pressure existing in region W' will be the lowest in the cycle. It generally gives rise to the flow reversals from the EO and AI ports. The exchange of fluid from region Z' to W', allowed by the expansion pocket, increases the pressure in region W'. The arrow shown in the pressure diagram gives the direction of fluid exchange through the expansion pocket. Higher pressure in the region W' ensures proper low-pressure scavenging. The compression pocket facilitates the pre-compression stage at the beginning of cycle, in the high-pressure part. Figure 6.14 shows the pressure and temperature variation over the cycle. The pressure plot shows the rise in air pressure at the compression pocket.

6.4.3 Variable Speed Performance of Comprex with Pockets

As discussed earlier, the pocket combination gives variable speed operability to a four-port PWS, in the direction of lower speed. Simulations of Comprex with pocket combination has been performed for varying rotor speed, to identify the effect of wall-pockets on the performance of a PWS with pockets.

The pressure and temperature boundary conditions are same as those used in the variable speed test 1 conducted on the four-port PWS geometry, in section 5.2.1. The reference pressure and temperature are 14.7 psi and 518 R, respectively. The non-dimensional static pressure of 1.47 was used at the AO port. The dimensionless exhaust gas pressure and temperature were assumed to be 1.78 and 1.66, respectively. Standard atmospheric conditions were assumed at the EO port. The rotor speed was changed from 6,000 RPM to 12,750 RPM. The pressure and temperature boundary conditions were kept constant and only the rotor speed was varied for each simulation. Table 6-2 shows the mass flow rate through each port and gas pocket (GP), for different rotor speeds. It can be observed that the mass flow rate through EO port, which generally tends to decrease with reduction in rotor speed, is maintained at sufficient values, even at much lower speeds.

Table 6.2. Mass flow rate through each port for varying rotor speed (Comprex simulation with pockets)

Rotor Speed (RPM)	Mass Flow Rate(lbm/min)				
	AI	AO	EI	EO	GP
6,000	10.69	10.41	10.11	14.06	3.8
7,000	11.18	11.32	10.73	14.43	3.97
8,500	10.97	10.92	11.67	15.22	4.33
10,625	12.46	11.07	12.34	17.97	4.39
12,750	14.72	7.63	11.29	21.06	2.83

Table 6.3 shows the total pressure in each port and pocket, computed by the wave rotor codes at each rotor speed. Faster the rotor rotates, later the primary expansion wave arrives at the expansion pocket. This means, the low pressure band W' will become narrower as the rotor speed increases and lesser amount of fluid will leave the expansion pocket. Hence, the pressure existing in the expansion pocket will be higher at higher speeds. Figure 6.16 shows

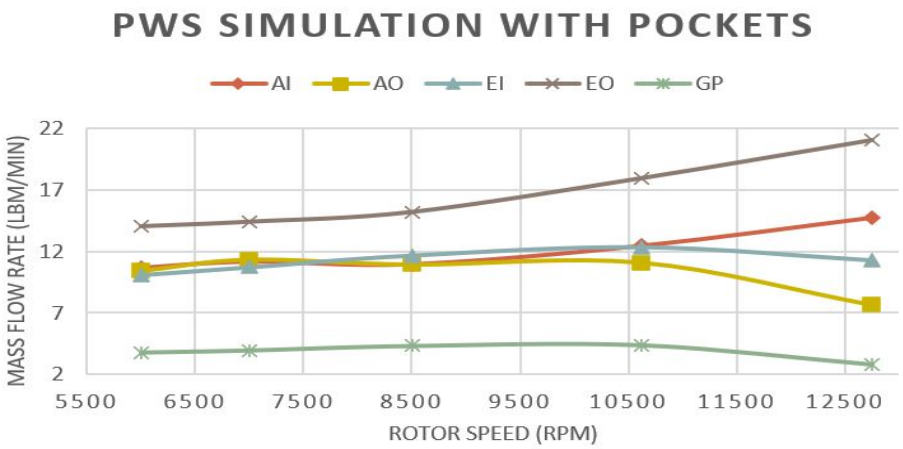

Figure 6.15. Mass flow rate variation for varying rotor speed

Table 6.3. Total pressure in each port and pocket

Rotor Speed (RPM)	Total Pressure (non-dim)						
	CP	AO	EP	AI	EI	GP	EO
6,000	1.31	1.52	1.43	0.98	1.86	1.91	1.04
7,000	1.15	1.54	1.46	0.98	1.85	1.92	1.04
8,500	1.13	1.56	1.52	0.98	1.84	1.91	1.04
10,625	1.09	1.57	1.62	0.98	1.82	1.91	1.06
12,750	1.18	1.61	1.7	0.98	1.84	1.97	1.08

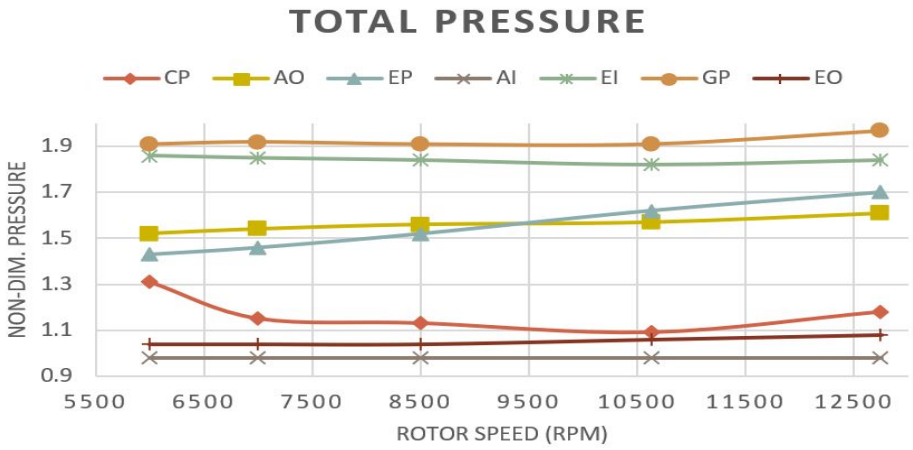

Figure 6.16. Total pressure variation with varying rotor speed

the total pressure variation following the varying speed of the rotor. The terms CP, EP and GP are the acronyms for compression pocket, expansion pocket and gas pocket, respectively.

6.5 Validation of Comprex Simulation Models

Modeling of wall-pockets and Comprex simulation with wall-pockets has been discussed in previous sections. This section aims to validate the computational results by comparing against the experimental data available. Simulation of Comprex with wall-pockets has been performed in this section by choosing the laboratory test conditions from AFIT experimental study described in B. Smith [32]. Three test points were selected in the AFIT experiment to investigate the performance of Comprex. The mass flow rates, pressures and temperatures at each port were measured for three different rotor speeds. The recorded pressures and temperatures from the AFIT experiment have been used as the essential boundary conditions. It should be noted that the AFIT experimental testing did not emulate the real-world operation of Comprex but it was a bench-top laboratory testing. Further, the wave rotor analysis codes compute the values of pressures and temperatures at the rotor exit face and taking measurements at the rotor exit face was rather impossible to implement in the experimental set-up. Three tests conducted were at the rotor speeds 9,420 RPM, 12,000 RPM and 12,960 RPM. Mass flow rate provided to the EI port at 9,420 RPM and 12,960 RPM was 13.1 lbm/min whereas at 12,000 RPM it was 15.9 lbm/min. The comparison between experimental and computational results has been shown in table 6.4.

Table 6.4. Mass flow rate comparison between AFIT experimental results and Comprex simulation results with pockets

Rotor Speed (RPM)	Mass Flow Rate (lbm/min)							
	Experimental				Computational (With Pockets)			
	AI	AO	EI	EO	AI	AO	EI	EO
9,420	6.45	10.18	13.04	9.31	6.82	11.36	14.64	9.04
12,000	10.03	12.59	15.87	13.31	12.58	12.13	13.64	15.92
12,960	10.05	11.07	13.04	12.2	11.14	9.08	11.45	13.42

Table 6.5 shows the percentage difference between the experimentally measured values and computationally predicted values. Figure 6.17 shows the comparison of velocity profile over the cycle for three test points. Figures 6.18 and 6.19 show the experimental and computational mass flow rates.

Table 6.5. Difference between the experimentally measured and computationally predicted values of mass flow rate

	AI	AO	EI	EO
9,420	6 %	11 %	12 %	3 %
12,000	25 %	4 %	14 %	19 %
12,960	11 %	17 %	12 %	10 %

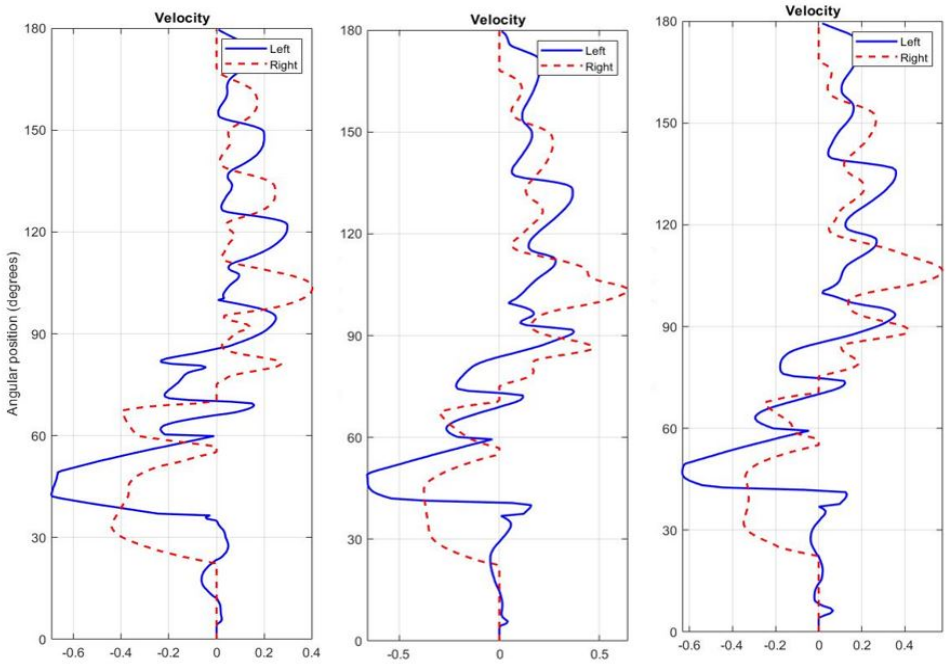

Figure 6.17. Velocity profiles (Left to Right- 9,420 RPM, 12,000 RPM, 12,000 RPM)

The maximum difference between the experimental and computational values of mass flow rates occurs at the AI port in 12,000 RPM rotor speed simulation. The results predicted by the computational codes are highly dependent on the EI port pressure and temperature as well as static pressure at the AO port. So, it is important to use the accurate value of static pressure at the AO port which was not recorded in the experiment. Also, the locations where the measurements were taken during the experiment are not in the vicinity of the rotor whereas the code predicts the values at the rotor exit face. A valve used at the AO port was adjusted in the experiment to balance the mass flow rates through AO and EO ports. The wave rotor analysis codes have the ability to incorporate the exit vales at corresponding ports. In above simulation, the exit valve simulation modules were not used. Despite the differences

between the experimental setup and computational boundary conditions, it can be seen that the wave rotor analysis codes can reliably predict the performance of Comprex-like PWS.

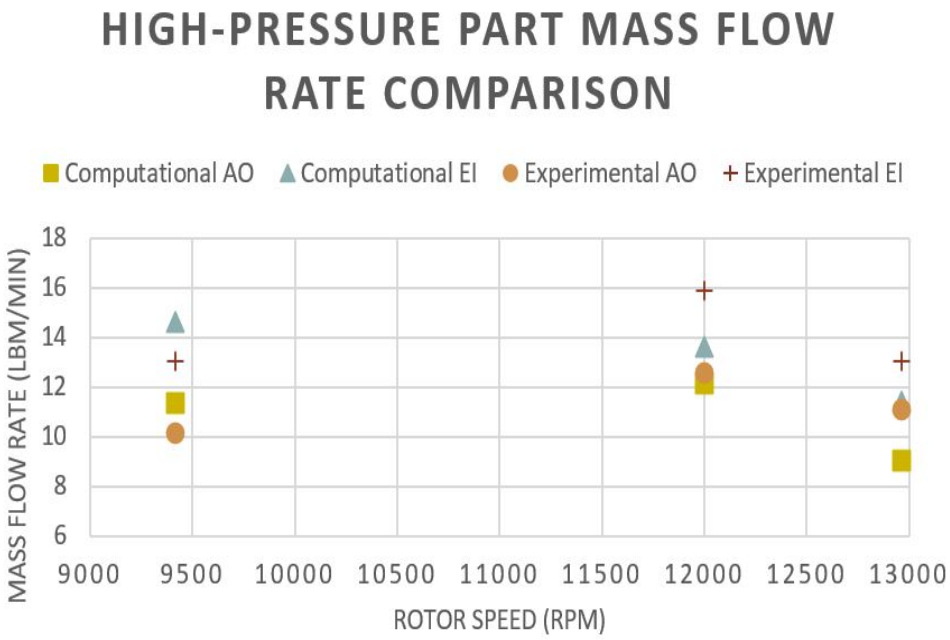

Figure 6.18. High-pressure part mass flow rate comparison

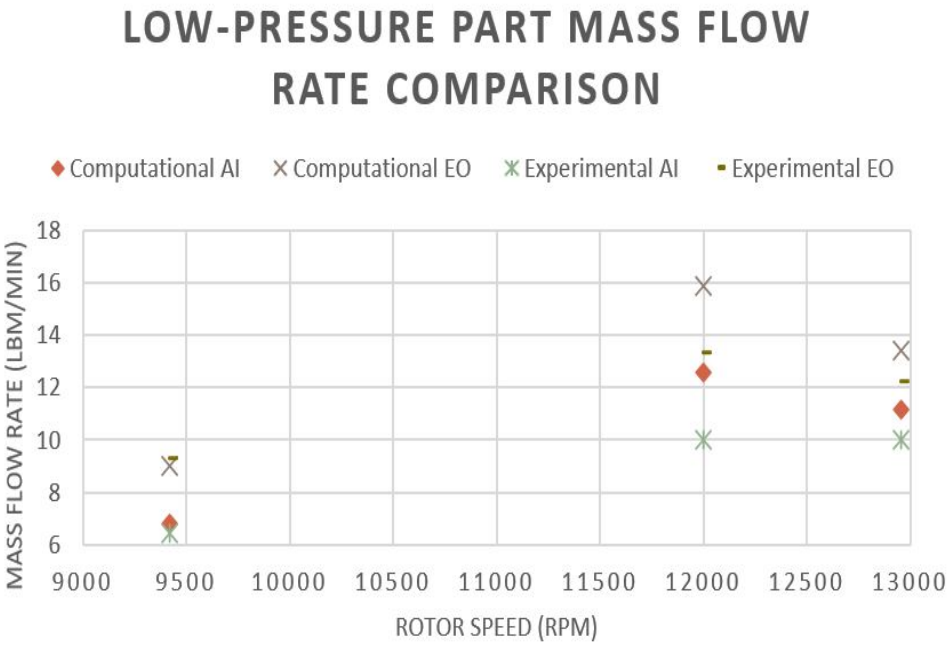

Figure 6.19. Low-pressure part mass flow rate comparison

6.6 Simulation of Comprex under Realistic Operating Conditions

There is limited experimental data available on the Comprex performance under realistic operating conditions. The only experimental data available is from a laboratory experimental testing conducted at the Air Force Institute of Technology, described in ref. [32]. In this section, an attempt has been made to investigate the performance of Comprex fitted on Mazda 626 diesel engine. The engine specifications have been listed in Table 4.1. Mazda 626 2.0 l diesel engine, for which the Comprex was used, had 4 inline cylinders with total displacement volume of 1998 cc. The engine thermal and volumetric efficiencies were assumed to be 46% and 90%, respectively. The engine produces 179 Nm torque at 2,000 RPM. From Comprex pulley ratio of 4.25:1, the rotor speed at this operating point was calculated to be 8,500 RPM. Lower heating value (LHV) of diesel fuel used here is 46,500 kJ/kg.

The power output at 2,000 RPM can be calculated as,

$$W = \frac{2\pi NT}{60\times 1000} = 37.489kW$$

Estimated fuel consumption at this operating condition,

$$m_f = \frac{W}{\frac{LHV}{3600}\times\frac{\eta_{th}}{100}} = 6.309kg/h$$

Assuming the engine operation at air to fuel ratio (AFR) of 23, air flow can be calculated as

$$m_a = m_f \times AFR = 145.121kg/h = 5.3322lbm/min$$

From air and fuel mass flow rate to the engine, the exhaust mass flow rate can be calculated as

$$m_{eg} = m_f + m_a = 151.43kg/h = 5.5622lbm/min$$

For the mass flow rate of air to the engine cylinder during the intake stroke, pressure of the engine intake air can be calculated as

$$P = \frac{m_a R_{Specific} T}{V_{displacement}\eta_{vol}} = 164.1378kPa$$

Here, temperature T was assumed to be equal to 385 R. These pressure and temperature values can be used at the AO port as boundary conditions. The stagnation conditions at the AI port can be used to nondimensionalize the AO port pressure and temperature values. The EI port boundary conditions were estimated by using the isentropic relations for a diesel cycle. The nondimensional static pressure and temperature at the AO port are 1.59 and 1.34, respectively. Similarly, the nondimensional stagnation pressure and temperature at EI port are 1.59 and 2.62, respectively. The boundary conditions were applied as described above to simulate the Comprex working under realistic conditions.

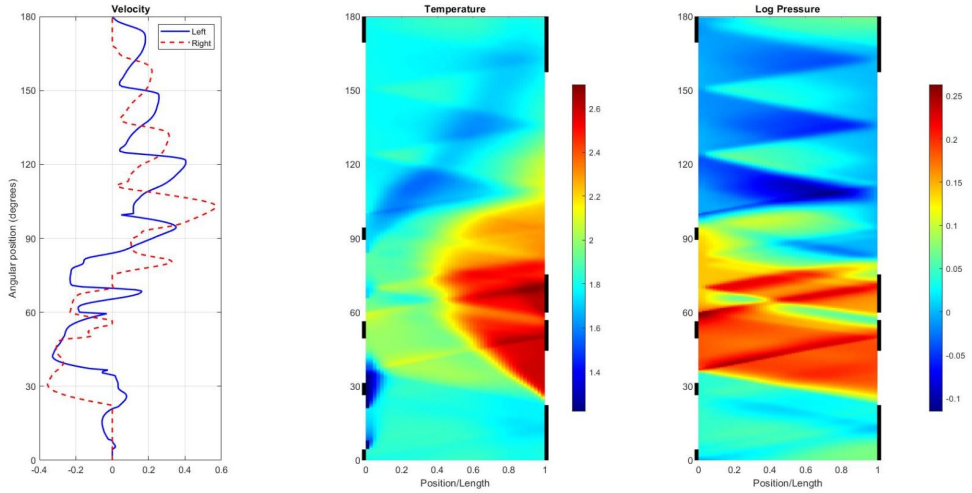

Figure 6.20. Velocity, Temperature and Pressure taces (Comprex simulation under realistic conditions)

Figure 6.20 shows the velocity, temperature and pressure traces over the cycle. The mass flow rate through the AO port predicted by the code when applied the pressure and temperature boundary conditions as described above is 5.81 lbm/min which is closer to the mass flow rate required by the engine at 2,000 RPM. Similarly, the mass flow rate through the EI port is 5.86 lbm/min, which is in good agreement with the estimated exhaust gas flow.

7. SUMMARY

7.1 Summary of Results

The intent of this work is to develop a methodology of using the wave rotor analysis codes to simulate the performance characteristics of the pressure wave superchargers with wall-pockets. The wall-pockets are design features for the extension for speed and load range of PWS, first found in the Comprex PWS, developed by Brown Boveri and Company. Three versions of wave rotor analysis codes, used at the Combustion and Propulsion Research Laboratory at IUPUI, were used for simulating the Comprex geometry operating at different speeds. The NASA Q1D code has been previously validated for the Comprex geometry and size. In this work, the axial-passage (SCW1D-A) and non-axial passage (SCW1D-B) versions of the SCW1D code, derived from Q1D with substantial modifications, have been validated for geometry, size, and design elements unique for Comprex. The results predicted by the codes are in fair agreement with the limited experimental data available.

When used for complex geometries like PWS, It is important to verify that novel features such as pockets can be consistently implemented in the more basic Q1D and more advanced SCW1D versions. As all codes have been modified several times for including additional features, it was important for version control to keep track of the changes made to the codes. The codes were first validated for the basic unsteady flow processes with and without friction and rotation. The results produced by the three codes were compared against the analytical solutions for the basic unsteady processes. All three codes were in good agreement with the analytical solution as well as with each other. The conservation equations in SCW1D-B version include additional terms to account for the passage curvature. The conservation equations to account for the passage curvature in SCW1D-B have been manipulated algebraically such that the additional terms from the passage curvature are transferred to the source vector. The SCW1D-A and SCW1D-B versions produce identical results when the passage curvature is set to zero. Also, the observations made about the performance of codes at non-optimum duct angles, have raised the need to review the incidence model and port mixing calculations used in NASA Q1D and SCW1D (A and B). Some minor discrepancies were identified and resolved in the friction modeling. Based on this verification study and

the fact that flow incidence in pockets can be substantially non-optimal, it was decided to implement the pockets model in the Q1D and SCW1D-A codes, but not the SCW1D-B code.

The main objective of this work was to extend the capability of the SCW1D-A program to incorporate the wall-pockets used in the PWS configurations. Numerical modeling of wall-pockets has been performed using a simple lumped volume technique. The pocket density and pressure are updated using the continuity and energy equations in such a way that the net mass and energy fluxes of the pockets are each driven to zero as the solution converges, neglecting heat losses. The SCW1D programs can embody any number of ports due to their modularity. The pockets have been modeled by considering them as ports. To more easily incorporate the three wall-pockets provided in Comprex, the four-port cycle was arranged for the simulation to begin with the cycle's high-pressure part. This simulation approach provided the necessary dead-time (angular position equivalent to wall boundary) between the ports to incorporate the pockets at desired locations. The simulation results show that the pocket combination works to serve the qualitatively explained purpose of facilitating the low-pressure scavenging. It was observed that the mass flow rates through each port remain almost unchanged during the low-speed operation of the Comprex. With the capability to simulate the wall-pockets, the wave rotor analysis codes can be reliably used to design and scale the PWS geometries with pocket combination.

7.2 Conclusions

An unsteady, one-dimensional numerical module has been developed to simulate the effects of wall-pockets used in four-port wave rotors. The simulation results show that the pocket combination can establish sufficient high-pressure zones at desired locations by capturing the energy of certain waves at a phase of the cycle and redistributing the energy to adjacent phases of the wave cycle. The pocket simulation module, when used in the wave rotor analysis code, can predict the performance of pressure wave superchargers with pockets. The main advantage achieved in this work is to extend the capability of computational code SCW1D-A to incorporate the wall-pockets, which will allow the design of pockets in future applications of wave rotors, including wave rotor combustors.

The simulation results have also shown that the SCW1D programs can satisfactorily predict the performance of pressure wave superchargers of size, geometry, and unique design elements similar to Comprex. Although the limited experimental data is available to compare the results, it has been observed that the simulation results are in good agreement with the qualitative expectations of the pocket combination used in Comprex. The lumped volume models of individual pockets have been observed to be able create the high-pressure bands as per necessity and hence can be used to design novel pocket locations as per custom requirements.

This work also presented the opportunity to review and compare the modeling approaches used in NASA Q1D and SCW1D programs, for modeling different phenomena such as friction and non-uniform port flow mixings. Some minor discrepancies were identified and resolved.

7.3 Recommendations for Future Work

A limited set of experimental test data is available to understand the operation of Comprex-like PWS under variable speed and different boundary conditions. Although the experiment was not intended to duplicate the practical diesel engine operating conditions, the simulations have predicted the results close to the experimental data available by acceptable margin of errors, considering the challenges in measuring the accurate values during the experiment. The wave rotor analysis codes can be used to scale a small PWS with pockets for diesel engines. Students at IUPUI have previously attempted to scale a PWS for Kubota diesel engine used in Snowmobile race vehicle. Similar study can be conducted to design and manufacture a PWS with pockets. The device can also be used to generate the experimental data for future research.

This work presented an opportunity to review the modeling of different physical phenomena, mixing calculations and fundamental numerical scheme used in three wave rotor analysis codes. Efforts should be continued to review different modules of the codes to check if there are any differences present in the modeling approaches used in NASA Q1D and SCW1D codes, and to improve the incidence loss model of SCW1D-B such that pockets can be designed for wave rotors with bent or non-axial channels. Also, the errors in incident loss modeling in SCW1D-B code should be investigated.

In this work, the pocket locations are specified as per the measurements taken on the Comprex PWS. The pocket locations and widths can be varied to examine whether they are optimal or can be improved. The pocket effects can be applied for realistic diesel engine conditions of PWS operation, by matching EI mass flow rate to a specific percentage of AO mass flow up to 100%. The flow restriction (valve) between gas pocket and EI port can be added in the model, to more faithfully represent the geometric design.

REFERENCES

[1] P. Akbari, R. Nalim, and N. Mueller, "A review of wave rotor technology and its applications," *Journal of Engineering for Gas Turbines and Power-transactions of The Asme*, vol. 128, pp. 717–735, 2006.

[2] P. Rose and R. PH, "Potential applications of wave machinery to energy and chemical processes," *I"lll*, 1980.

[3] S. Claude, *Pressure exchanger*, US Patent 2,399,394, Apr. 1946.

[4] S. Claude, *Gas turbine installation*, US Patent 2,461,186, Feb. 1949.

[5] M. Berchtold and F. Gardiner, "The comprex: A new concept of diesel supercharging," in *Turbo Expo: Power for Land, Sea, and Air*, American Society of Mechanical Engineers, vol. 79979, 1958, V001T01A016.

[6] M. Berchtold, "The comprex diesel supercharger," *SAE Transactions*, pp. 5–14, 1959.

[7] M. Berchtold and H. Gull, "Road performance of a comprex supercharged diesel truck," *SAE Transactions*, pp. 367–379, 1960.

[8] P. K. Doerfler, "Comprex supercharging of vehicle diesel engines," SAE Technical Paper, Report 0148-7191, 1975.

[9] G. Schruf and T. Kollbrunner, "Application and matching of the comprex pressure-wave supercharger to automotive diesel engines," *SAE transactions*, pp. 772–785, 1984, ISSN: 0096-736X.

[10] G. Zehnder and A. Mayer, "Comprex® pressure-wave supercharging for automotive diesels—state-of-the-art," *SAE transactions*, pp. 756–771, 1984, ISSN: 0096-736X.

[11] P. t. Azoury, "An introduction to the dynamic pressure exchanger," *Proceedings of the Institution of Mechanical Engineers*, vol. 180, no. 1, pp. 451–480, 1965, ISSN: 0020-3483.

[12] L. Guzzella, U. Wenger, and R. Martin, "Ic-engine downsizing and pressure-wave supercharging for fuel economy," SAE Technical Paper, Report 0148-7191, 2000.

[13] A. Mayer, J. Oda, K. Kato, W. Haase, and R. Fried, "Extruded ceramic-a new technology for the comprex®-rotor," SAE Technical Paper, Report 0148-7191, 1989.

[14] P. H. Snyder, "Wave rotor demonstrator engine assessment," 1996.

[15] D. PAXSON and J. Wilson, "An improved numerical model for wave rotor design and analysis," in *31st Aerospace Sciences Meeting*, p. 482.

[16] D. PAXSON, "A comparison between numerically modelled and experimentally measured loss mechanisms in wave rotors," in *29th Joint Propulsion Conference and Exhibit*, 1993, p. 2522.

[17] D. E. Paxson, "Comparison between numerically modeled and experimentally measured wave-rotor loss mechanisms," *Journal of Propulsion and Power*, vol. 11, no. 5, pp. 908–914, 1995.

[18] G. Welch and D. Paxson, "Wave turbine analysis tool development," in 34*th AIAA \ASME \SAE \ASEE Joint Propulsion Conference and Exhibit*, p. 3402.

[19] M. R. Nalim, "Preliminary assessment of combustion modes for internal combustion wave rotors," in *31st Joint Propulsion Conference and Exhibit*, p. 2801.

[20] M. Nalim and M. Nalim, "Numerical study of stratified charge combustion in wave rotors," in *33rd Joint Propulsion Conference and Exhibit*, 1997, p. 3141.

[21] T. M. Elharis, "A multi-step reaction model for stratified-charge combustion in wave rotors," Thesis, Purdue University, Indianapolis, 2011.

[22] R. R. Jagannath, "Development of plasma assisted ignition for wave rotor combustion turbine," Thesis, Purdue University Graduate School, 2019.

[23] W. Jose, J. Ernst, and M. Kurt, *Pocket combination for extension for speed and load range of awm supercharger*, US Patent 3,120,920, Feb. 1964.

[24] S. Basu, "One-dimensional simulation of non-steady channel flow in a pressure-wave supercharger with a pocket," Unpublished MS Project Report, 2018.

[25] S. Basu, "Comparison of versions of one-dimensional program to simulate non-steady flow in a pressure-wave supercharger with pockets," Unpublished MS Project Report, 2018.

[26] H. Aoki, *Control system and method for comprex supercharger*, US Patent 4,563,997, Jan. 1986.

[27] C. Leahu, H. Abăităncei, and S. Radu, "Drive with rotative speed independent from the engine, of the pressure wave compressors," *Recent Journal*, vol. 37, pp. 29–35, 2013.

[28] D. Paxson, "A numerical model for dynamic wave rotor analysis," in *31st Joint Propulsion Conference and Exhibit*, p. 2800.

[29] D. W. Paxson, "A general numerical model for wave rotor analysis," 1992.

[30] D. E. Paxson, "Numerical simulation of dynamic wave rotor performance," *Journal of Propulsion and Power*, vol. 12, no. 5, pp. 949–957, 1996, ISSN: 0748-4658.

[31] M. R. Nalim and D. E. Paxson, "A numerical investigation of premixed combustion in wave rotors," in *Turbo Expo: Power for Land, Sea, and Air*, vol. 78729, American Society of Mechanical Engineers, V001T01A039, ISBN: 0791878724.

[32] B. D. Smith, "Scaling study of wave rotor turbo-normalization of a small internal combustion engine," 2012.

[33] K. C. Smith, "Coupled dynamic analysis of flow in the inlet section of a wave rotor constant volume combustor," 2011.

[34] J. D. Anderson, *Modern compressible flow*. Tata McGraw-Hill Education, 2003, ISBN: 1259027422.

[35] M. R. Mataczynski, "Design and simulation of a pressure wave supercharger for a small two-stroke engine," 2014.

A. CONVERGENCE CHECK

The simulations presented in this thesis have used non-dimensional spacial grid size (numerical spacial step) of 0.02. The grid or computational cell size has been obtained by dividing the wave rotor passage into 50 cells. This size of spacial steps was determined by conducting a grid convergence check. The convergence check conducted on NASA Q1D and SCW1D (A and B) has been presented in this appendix. As stated earlier, both A and B versions of SCW1D code compute the same results when passage curvature angle is set to zero in version B. Hence the results presented under SCW1D title represent both version A and B.

The number of computational cells was varied from 25 cells to 150 cells by changing the grid sizing. The analysis results were compared with each other to determine the appropriate number of cells required in the model to ensure that the simulation results are not affected by additional grid refinement. Mass flux is a good measure to compare the results computed by each code. The mass flux values computed by the code when using 25 cells (non-dimensional spacial step of 0.04) are in close proximity with those values calculated by using 150 cells (non-dimensional spacial step of 0.00667). The point of 50 computational cells was determined by considering the time taken by the codes to compute the results and quality of plots generated after post-processing. Coarser grid of 25 cells produces low-quality x-t diagrams whereas the graphs generated by using 50 cells are of sufficiently higher quality. The difference between the results can be seen in presented x-t diagrams and velocity plots.

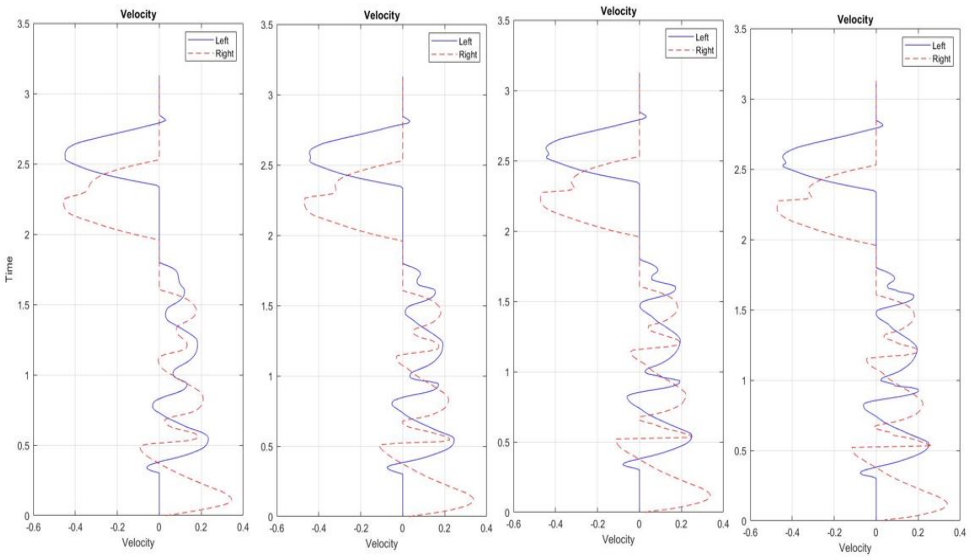

Figure A.1. Velocity profiles using different numbers of computational cells; (Left to right- 25 cells, 50 cells, 100 cells, 150 cells)

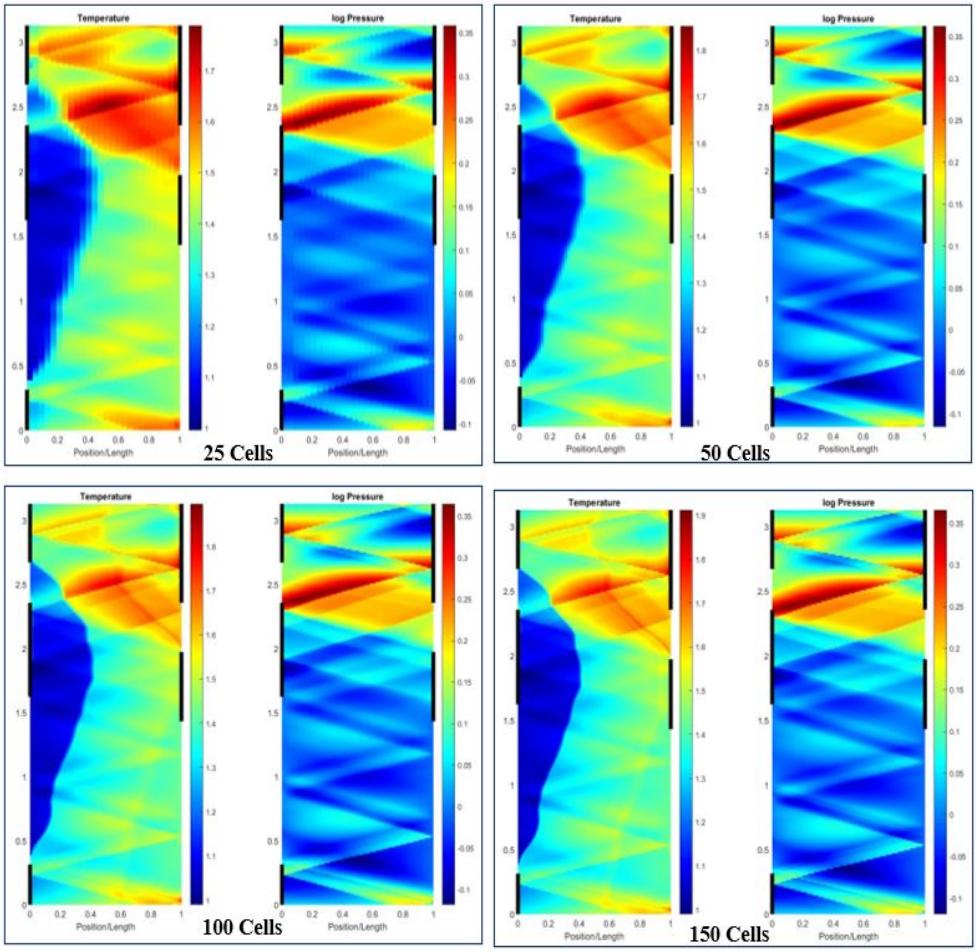

Figure A.2. x-t diagrams using different numbers of computational cells

A.1 NASA Q1D

Table A.1 shows the simulation results computed by NASA Q1D program for different grid sizing. It can be observed that the simulation results are almost unchanged for finer mesh refinement.

Table A.1. Grid convergence for NASA Q1D

Number of Cells	Cell Size	MF_{AI}	MF_{AO}	MF_{EI}	MF_{EO}
25	0.04	0.356	-0.410	-0.416	0.355
50	0.02	0.358	-0.410	-0.415	0.356
100	0.01	0.358	-0.410	-0.415	0.357
150	0.00667	0.358	-0.410	-0.415	0.357

A.2 SCW1D (A and B)

Table A.2 shows the mass flux computed by the SCW1D programs by using different numbers of computational cells. It can be observed that the simulation results are largely unaffected by additional mesh refinement.

Table A.2. Grid convergence for SCW1D (A and B)

Number of Cells	Cell Size	MF_{AI}	MF_{AO}	MF_{EI}	MF_{EO}
25	0.04	0.365	-0.449	-0.461	0.375
50	0.02	0.368	-0.449	-0.461	0.373
100	0.01	0.369	-0.450	-0.461	0.373
150	0.00667	0.369	-0.450	-0.461	0.373